وزارة التعليم العالي والبحث العلمي
جامعة بابل
كلية العلوم
قسم الفيزياء

تحضير أغشية نانوية من أوكسيد النحاس المشوب بثنائي أوكسيد النحاس لتطبيقات الخلايا الشمسية : الخصائص, وتأثير درجة التلدين و التشويب

أطروحة مقدمة الى
مجلس كلية العلوم في جامعة بابل وهي جزء من متطلبات
نيل درجة دكتوراه فلسفة في العلوم/ الفيزياء

من قبل

زينب قاسم محمد صوفي

بكالوريوس علوم فيزياء 2011
ماجستير علوم فيزياء 2015

بأشراف

الأستاذ الدكتور
عبد العزيز عبيد موسى العكيلي

الأستاذ الدكتور
خالد حنين عباس حسن

١٤٤٤ ه
٢٠٢٢ م

Supervisors Certification

We certify that this thesis is titled (**Preparation of CuO Doped Cu_2O Nanofilms for Solar Cell Applications: Characterizations, Annealing Temperature and Doping Effect**) will be prepared by (**Zainab Qassim Mohamed Sofi**) under our Supervision at Plan of Doctor, of Philosophy Submitted to the Department of Physics, College of Science, University of Babylon in (Material Physics).

Signature:

Supervisor:Dr.AbdulazeezO.Mousa Al-Ogaili
Title: Professor
Address: Department of Physics –
College of Sciences
University of Babylon
Date: / / 2022

Signature:

Supervisor:Dr.Khalid Haneen Abass Hassan
Title: Professor
Address: Department of Physics College
of Education for pure Sciences University of
Babylon
Date: / / 2022

Certification of the head of the Department

In view of the available recommendation, I forward this thesis for debate by the Examination Committee.

Signature:

Name: Dr. Faez Ali Rashid AL-Maamori
Title: Professor
Address: Head of Department of Physics- College of Science-University of Babylon.

Date: / / 2022

Ministry of Higher Education and Scientific Research
University of Babylon
College of Science
Department of Physics

Preparation of CuO Doped Cu_2O Nanofilms for Solar Cell Applications: Characterizations, Annealing Temperature and Doping Effect

A Thesis

Submitted to the Council of the College of Science University of Babylon in Partial Fulfillment of the requirements for the Degree of Doctorate of Philosophy in Physics

By

Zainab Qassim Mohamed Sofi

B.Sc. in Physics 2011
M.Sc. in Physics 2015

Supervised by

Prof.Dr.

Abdulazeez O. Mousa Al-Ogaili

Prof.Dr.

Khalid Haneen Abass Hassan

2022 A.D. **1444 A.H.**

بسم الله الرحمن الرحيم

﴿ يَٰٓأَيُّهَا ٱلَّذِينَ ءَامَنُوٓاْ إِذَا قِيلَ لَكُمۡ تَفَسَّحُواْ فِي ٱلۡمَجَٰلِسِ
فَٱفۡسَحُواْ يَفۡسَحِ ٱللَّهُ لَكُمۡۖ وَإِذَا قِيلَ ٱنشُزُواْ فَٱنشُزُواْ يَرۡفَعِ ٱللَّهُ
ٱلَّذِينَ ءَامَنُواْ مِنكُمۡ وَٱلَّذِينَ أُوتُواْ ٱلۡعِلۡمَ دَرَجَٰتٖۚ وَٱللَّهُ بِمَا
تَعۡمَلُونَ خَبِيرٞ ﴾

صَدَقَ اللهُ العَظِيْم

سورة المجادلة ، الآية ﴿ ١١ ﴾

الخلاصة

في الدراسة الحالية ، حضرت أغشية رقيقة من أوكسيد النحاس (CuO) النقي والمشوب بأوكسيد النحاس الثنائي (Cu_2O) بنسب وزنية مختلفة(0.006,0.004,0.002) ٪ بتقنية التبخير الحراري تحت ضغط مقداره(1×10^{-7}) ملي بار وبمعدل ترسيب (0.5) نانومتر بالثانية مُرسبة على قواعد من الزجاج والسيلكون بدرجة حرارة الغرفة وبسمك (75) نانومتر عند درجة حرارة تلدين (200) سيليزي لمدة ساعة ولمدة ساعتين. درست طبوغرافية السطح للغشاء المحضر بوساطة جهاز مجهر القوى الذرية، حيث تم ملاحظه أن بزيادة درجة حرارة التلدين يقل كل من الحجم الحبيبي ومعدل الخشونه من(0.467-0.337) نانومتر ومعدل مربع الجذر من (0.581-0.426) نانومتر ومعدل القطر الذي تم حسابه من خريطة عرض الصور يقل من (2.143-1.149) وكذلك تقل كافة المعاملات بزيادة نسب التشويب لأوكسيد النحاس الثنائي.

أظهرت نتائج حيود الاشعة السينية (XRD) بأن جميع الأغشية المحضرة كانت متعددة التبلور وذات تركيب متعامد المحاور عند المستوى (110) عند الزاوية (32.162°) القمة الرئيسية كانت عند الزاوية (32.162°) والتي تعود الى مستوى الانعكاس (110) .اوكسيد النحاس النقي حيث كانت اعظم شدة (100) وبحجم حبيبي(18) نانومتر .اضهرت النتائج نقصان في الحجم الحبيبي مع زيادة نسبة التشويب بأوكسيد النحاس الثنائي . تأثير درجة حرارة التلدين على المركب تم حسابه بوساطة المجهر الالكتروني الماسح بمدى للحجم الحبيبي يتراوح بين (15.42 الى 35.05) نانومتر.

تم دراسة الخصائص البصرية بتسجيل أطياف الامتصاص بأستخدام مطياف الاشعة فوق البنفسجية المرئية بمدى طول موجي (300-1100) نانو متر، تزداد الامتصاصية بزيادة نسبة التشويب بأوكسيد النحاس الثنائي بينما تقل النفاذية. تقل فجوة الطاقة البصرية من (3.3-3.05) الكترون فولت بعد التلدين لمدة ساعتين وبدرجة حرارة (200) سيليزي. تشير القيم العالية لفجوة الطاقة الى تأثير التكميم. تزداد الثوابت البصرية كمعامل الانعكاس ومعامل الخمود ومعامل الامتصاص بزيادة درجة حرارة التلدين ،تأثير التكميم تولد من خلال فجوة الطاقة المكتسبة الحجم الحبيبي يزداد بزيادة نسبة التشويب باوكسيد النحاس الثنائي.

حضر المفرق ($CuO:Cu_2O/Si$) بنسب وزنية مختلفة تبين. النتائج ان الغشاء المحضر بهذه الطريقة يمتلك سطح متجانس. تضمنت الخصائص البصرية قياسات هول. خصائص أضاءه-ظلام ظهرت عند التشويب بأوكسيد النحاس فأن الطاقة لكفاءة التباعد تزداد. وبإعادة ترتيب الزوج الكترون- فجوة وبحساب أن أفضل كفاءة للمفرق المتباين الناتج من القيمة العالية لتيار الدائرة المفتوح وفولتية الدائرة

المفتوحة وقد وجد إن أعلى كفاءة تم الحصول عليها عند نسبة تشويب (0.006) % هي بقيمة (3.642857 % أن أعلى قيمة لجهد الدائرة المفتوحة V(1.95 للعينة Si (p) المرسب عليها غشاء من النوع (n) و أن أعلى قيمة لتيار الدائرة المفتوحة تكون (0.0180) $mA\ cm^{-2}$ وأعلى قيمة لعامل الملىء تكون (0.7264) عند طاقة تعادل تقريبا ($100\ mW/cm^{2}$) .

Acknowledgments

I like to express my deep thanks and gratitude to my respected supervisors, **Prof.Dr. Abdulazez O.Mousa Al-Ogaili** and **Prof.Dr. Khalid Haneen Abass Hassan** for their suggesting this project, and their remarkable notes, advice, support, during the whole work of mine, special thanks go to **Prod.Dr.Saleem azara hussain** ,who provided me with any kind of help during this work.

Finally, many thanks to Department of Physics, College of Science and Department of Physics, College of Education for Pure Science, for offering me the opportunity to complete my thesis.

Zainab

Dedications.

First and foremost this humble work is dedicated to almighty God to fill me with strength and power…….. to my father, Cindy to my loving mom for her patience and constant Support , And care .

To the one who sacrificed for my happiness always and forever my husband.

Zainab

Scientific Activities

1. papers

a. Paper(CuO Quantum Dot Annealed Layer Prepared via Thermal Evaporation Technique) has been accepted for publication in scopus container (1st international Conference for Pure Science ICPS-2021).

b. Paper **(**Morphology of Copper Oxide Nano-Layer Prepared via Thermal Evaporation Technique) has been published in scopus container (NeuroQuantology), Volume 20, March 2022.

c. Paper **(**Enhancement of CuO/Si Solar Cell Efficiency by Cu_2O doping Prepared via Thermal Evaporation Technique) under review.

2. Conferences

Certificate of participation in the international scientific conference for pure sciences at the university of diyala in partnership with western Michigan university, and a certificate of participation in the fifth international conference on chemical safety and security.

3. Symposiums

Participation in two scientific symposium for postgraduate student in the faculty of science, department of physics, in addition to obtaining a certificate of attendance in eleven scientific symposiums.

4. training courses

Certificate of participation in five national training courses

5. electronic seminars

Participation in three electronic seminars in the department of physics, the most important of which was how to raise the level of scientific research among graduate students, as well as about the importance of publishing in international journals.

6. Workshops

Certificate of attendance in three international and twenty-five national workshops.

Summary

In the present study, copper oxide (CuO) and Cu_2O-doped CuO with different weight ratio of (0.002, 0.004, and 0.006) wt.% thin films were prepared by thermal evaporation technique, with a rate of deposition 0.5 $nm.s^{-1}$, deposited on glass substrates under a pressure of 1×10^{-7} mbar. At a thickness of 75 nm, CuO thin films were annealed at 200 ℃ for one and two hours. The surface topography of the prepared films using atomic force microscopy (AFM) has been studied. It has been observed that by increasing the annealing temperature for two hours, the roughness decreased from (0.467 to 0.337) nm, the root mean square (RMS) decreased from (0.581 to 0.426) nm, and the average grain diameter was evaluated from the plane view image that decreased from (149.1 to 143.2) nm. Also, they decreased by increasing Cu_2O doping ratio.

The X-Ray diffraction (XRD) results showed that the prepared films were polycrystalline with orthorhombic structure and preferential orientation in (110) direction along the c-axis at $2\theta = 32.162^{\circ}$. The main peak was observed at $2\theta = 32.321^{\circ}$, which corresponds to the reflection plane (110) for pure CuO with a crystallite size of 18 nm. The results showed that decreasing in crystallite size with the increasing of Cu_2O doping. The effect of annealing temperature on the structure was measured using scanning electron microscopy (SEM), and the particle size ranged from (15.42-35.05) nm.

The optical properties were studied by recording the absorbance spectra using a UV-Visible spectrophotometer. In the wavelength range (300-1100) nm, the absorbance increased with increasing the Cu_2O with different weight ratio, while the transmittance decreased. The optical band gap decreased from (3.3 to 3.05) eV after annealing the temperature to 200 ℃ for two hours. The high values of the energy gap refer to the quantization effect.

The optical constants such as absorption coefficient and extinction coefficient increased with increasing the annealing temperature. Obviously, the quantization effect emerging was caused by the acquisition of high values of the energy gap. The crystallite size increased with increasing of Cu_2O doping. $CuO:Cu_2O/Si$ heterojunctions have been prepared at different weight ratio. The measurements confirmed that the thin films, grown by this technique, have homogeneous surfaces.

The electrical properties including the Hall effect were studied. I-V characteristics showed that the Cu_2O doping increased the energy conversion efficiency by retarding the electron-hole recombination and the improved device performance is caused by the high short-circuit current (I_{sc}) , open circuit voltage (V_{oc}) found that the highest efficiency (η) at doping 0.006 wt.% is 3.642857% with (V_{oc}) of 1.95V, (I_{sc}) of 0.0180 mA cm^{-2}, fill factor (F.F) of 0.7264 at intensity P =100 mW/cm^2.

Contents

Chapter One: Introduction

Chapter Two : Theoretical Part

Chapter Three : Experimental Part

Chapter Four : Results and Discussion

List of Figures

List of Tables

List of Symbols and Abbreviations

Symbols	**Meaning**
A	Absorbance
A*	Cross Section Area
a	Lattice Constant
α	Absorption Coefficient
AFM	Atomic Force Microscopy
A'	Cross Section Area
ALD	Atomic Layer Deposition
AMI	Air Mass Illumination
B	Magnetic Field
Bz	Boltzman Factor
c	Light Velocity
C.B	Conduction Band
CVD	Chemical Vapor Deposition
D	Average Grain Size
D	Interplanner Distance
DSSCs	Dye-Sensitized Solar Cells
E_g	Energy Gap
E_{it}	Hall Electric Field
ε_i	Imaginary Dielectric Constant
E_p	Energy of Absorbed
ε_r	Real Dielectric Constant
E	Electric Field
EMF	Electromotive Force
F.F	Fill Factor
FWHM	Full Width at Half Maximum
h	Plank Constant
HJ	Heterojunction
hν	Photon Energy
I_s	Saturation Current
I_d	Dark Current
I_o	Inverse Saturation Current
I_{ph}	Photocurrent
I_t	Illuminated Current
I-V	Current-Voltage
I_{sc}	Short Circuit Current
IH	Hall Current
J_{sc}	Short Current Density
J	Current Density

Symbols	**Meaning**
k_B	Boltzmann Constant
K	Kelvin
K_{max}	Maximum Wave Vector
K_{min}	Minimum Wave Vector
k	Extinction Coefficient
L	Distance between the Electrodes
M	Weight Material
μ_n	Electron Mobility
μ_p	Hole Mobility
m	Mass of Material
MEMS	Micro Electro-Mechanical Systems
MBE	Molecular Beam Epitaxy
μ	Mobility
μ_H	Hall Mobility
μ_n	Electron Mobility
n	Refractive Index
n	Carrier Concentration
n^*	Complex Refractive Index
n-type	Negative Electric Conductivity
η	Efficiency
NPs	Nano-Particle Size
P_{in}	Incident Power
ρ	Resistivity
P_m	Maximum Power
p-type	Positive Electric Conductivity
PV	Photovoltaic
ρ_o	Material Density
q	Charge of Electron
R	Distance Between Substrate and Source
R_H	Hall Coefficient
RT	Room Temperature
R_{sh}	Shunt Resistant
Si	Silicon
Si_3N_4	Silicon Nitride
Si	Silicon Nano
SEM	Scanning Electron Microscopy
T	Transmittance
t	Thickness
T_S	Substrate Temperature

Symbols	**Meaning**
τ_c	Mean Free Time
TEVD	Thermal Evaporation in Vacuum Deposition
TFSC	Thin Film Solar Cell
TPD	Thermal Pyrolysis Deposition
T	Temperature
UV	Ultra Violet Spectrum
V.B	Valence Band
V_H	Hall Voltage
V_{oc}	Open Circuit Voltage
υ_n	Electron Drift Velocity
υ_p	Hole Drift Velocity
ν	Frequency (Hz).
V_{oc}	Open Circuit Voltage
v	Velocity of Propagation
W	Distance between Two Electrons
XRD	X-Ray Diffraction
θ	Bragg’s Angle
λ	Wavelength
R_e	resistance of electron

1.1 General Introduction

Several solar technologies including wafer, thin film and organic, have been researched to achieve reliability, cost-effectiveness and high efficiency with huge success. For instance, crystalline silicon has been very effective from laboratory to commercial integration, and makes up to 90% of the global photovoltaic (PV) [1].

Thin-film solar cells are basically thin layers of semiconductor materials applied to a solid backing material. Thin films greatly reduce the amount of semiconductor material required for each cell when compared to silicon wafers and hence lowers the cost of production of photovoltaic cells [2].

Furthermore, compared to more conventional photovoltaic such as silicon solar cells, the device operation principles of many of these thin film photovoltaic technologies are dependent on complex physical mechanisms, such as excitonic processes, photo induced charge separation and functional material interfaces[3].

In 1857, the scientist (Faraday) was able to obtain a thin metal film by using of Thermal Evaporation [4], thin-film technologies are also being developed as a means of substantially reducing the cost of solar cells. The rationale for this thin-film solar cells are cheaper to manufacture owing to their reduced material and energy costs [5].

Other thin-film technologies are often classified as emerging or third generation photovoltaic cells and include; organic, dye-sensitized, and polymer solar cells, as well as quantum dot, copper zinc tin sulfide, nano crystal, micro morph and perovskite solar cells, thin-film technologies reduce the amount of active material in a cell [6].

In this work will study the structure and examine the high efficiency of solar cell by using copper oxide (CuO) doped by cuprous oxide (Cu_2O) prepared by thermal evaporation technique.

1.2 Photovoltaic Solar Cell

Photovoltaics conversion is the direct conversion of sunlight into electricity without any heat engine to interfere. Photovoltaic devices are rugged and simple in design requiring very little maintenance and their biggest advantage being their construction as stand-alone systems to give outputs from microwatts to megawatts, hence they are used for power source, water pumping, remote buildings, solar home systems, communications, satellites and space vehicles, reverse osmosis plants, and for even megawatt scale power plants. With such a vast array of applications, the demand for photovoltaics is increasing every year [1].

The origin of the term "photovoltaic" is derived from Greek , meaning light, from the name Volta, an Italian physicist, volt - a unit of the electric impulse - and the term photovoltaic in English since 1849, the optical effect was first identified in 1839 by French physicist Becquerel, however, the first photovoltaic cell was built in 1883 by Charles Fritz, who encapsulated the semiconductor selenium with a very thin layer of gold to form intersections, the efficiency of the device was about 1% only, in 1888, Russian physicist Alexander Kostolitov built the first photovoltaic cell based on the external photoelectric effect discovered by Heinrich Hertz earlier in 1887 [7].

In the developing country , solar photovoltaic (PV) technology is key driver for electrifying rural areas. Available solar energy can be converted directly into direct current, is major advantage of using photovoltaic cells, moreover, as compared to conventional energy production, operating solar energy is much easier and requires less manpower. Photovoltaic (p-n) junction solar cell as shown in Figure (1.1), has important application of solar photovoltaic system that power supply to remote house or villages, irrigation and water supply, as compared to other power pumping devices which produces unbearable noise during operation, these solar cells produces no noise[8].

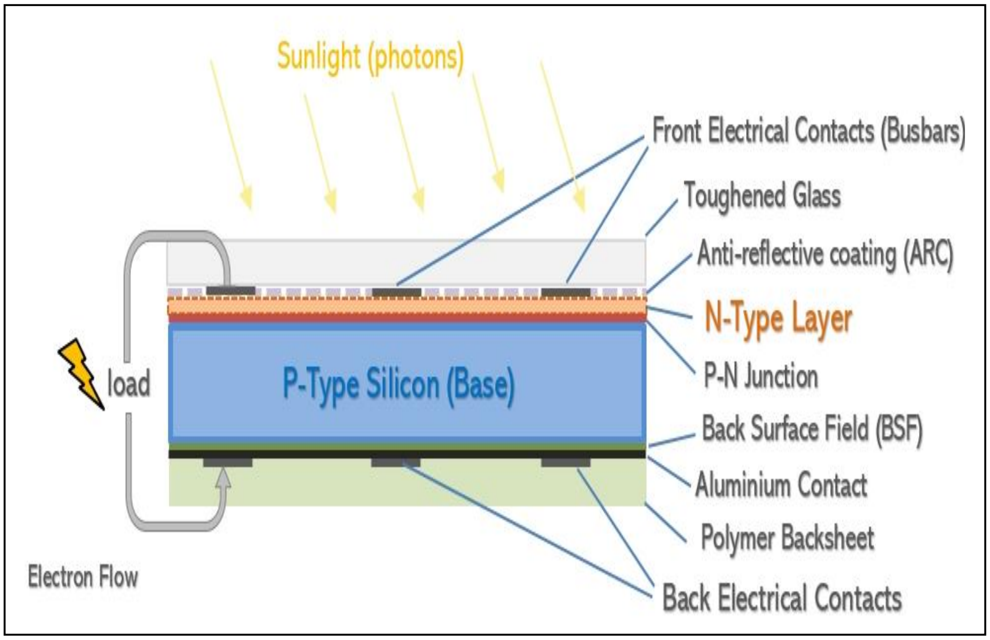

Figure(1.1): Photovoltaic(p-n) Junction Solar Cell [9].

1.3 Nanomaterial

Nanomaterials are materials with dimensions less than (100) nm and they have at least one unique property that is different from the bulk material, or the science is concerned with studying the treatment of the material on the atomic and molecular scale, nanotechnology is concerned with the invention of new methods and instruments whose dimensions are measured in nanometers, which is a fraction of a thousandth of a micrometer, a fraction of a millionth of a millimeter. nanotechnology usually deals with measurements from (0.1 to 100) nm, which deals with atomic clusters ranging from five to one thousand atoms [9]. Nanostructures of nanomaterials can be classified according to their dimensions (X, Y and Z) in space [10].

1. Zero-dimension (0-D) (represent for quantum dots or nanoparticles) .
2. One-dimension (1-D) (indicate to nanowires, nanorods, nanofibres, nanobelts, and nanotubes) .
3. Two-dimension (2-D) (refer to nanosheets, nanowalls and nanoplates).
4. Three-dimension (3-D) (represent to nanoflowers and other complex structures such as nano tetra pods).

The density of states which describes the electronic states with energy in the band diagram of the 0-D, 1-D, 2-D and cluster materials are shown in Figure(1.2) [11].

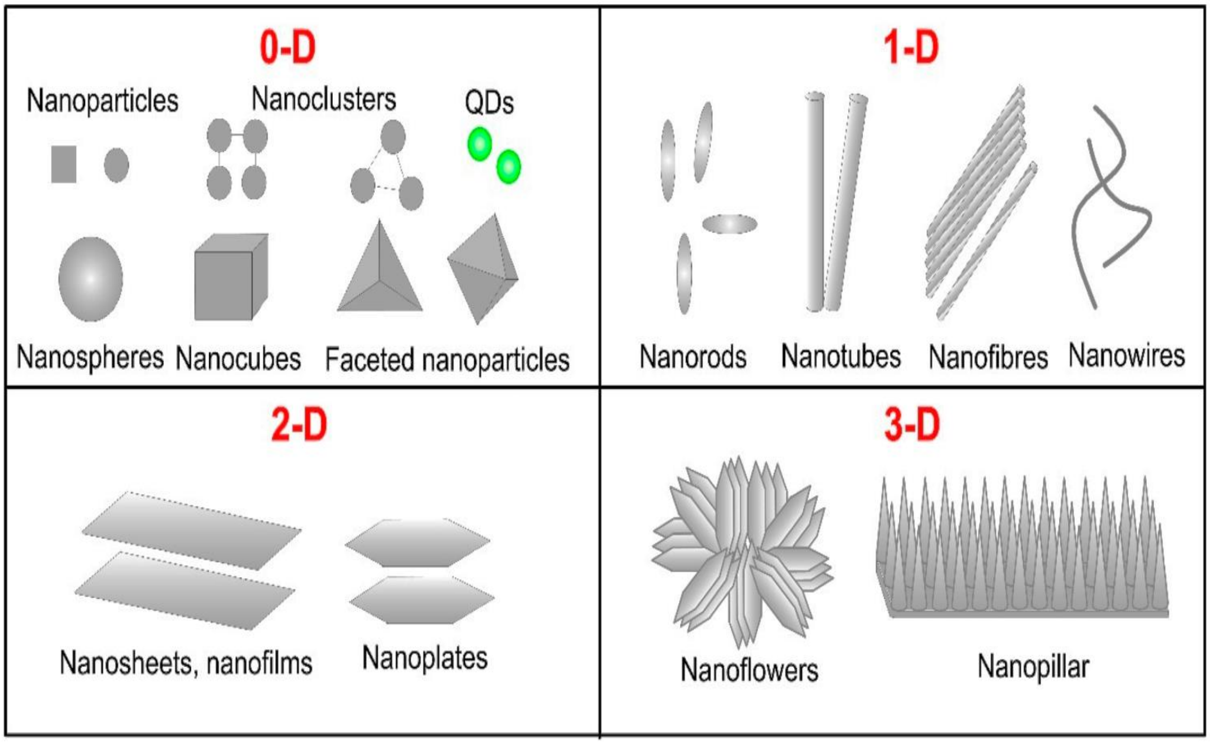

Figure (1.2): The Band Diagram of the(0-D, 1-D, 2-D) and Cluster Materials [12].

1.4 Synthesis of Nanomaterials Methods

In general, top-down and bottom-up are the two main approaches for nanomaterials synthesis[13].

a. Top-down: size reduction from bulk materials.

b. Bottom-up: material synthesis from atomic level.

Top-down routes are included in the typical solid.

State processing of the materials. This route is based with the bulk material and makes it smaller, thus breaking up larger particles by the use of physical processes like crushing, milling or grinding. Usually this route is not suitable for preparing shaped materials, and it is very difficult to realize very small particles even with high energy consumption [13].

The biggest problem with top-down approach is the imperfection of the surface structure. Such imperfection would have a significant impact on physical properties and surface chemistry of nanostructures and nanomaterials. It is well known that the conventional top-down technique can cause significant crystallographic damage to the processed patterns [14].

Bottom –up approach refers to the build-up of a material from the bottom: atom-by-atom, molecule-by-molecule or cluster-by-cluster. It effectively covers chemical synthesis and precisely controlled the reaction to inhibit further particle growth. Although the bottom-up approach is nothing new, it plays an important role in the fabrication and processing of nanostructures and nanomaterials, synthesis of nanoparticles to have a better control over particles size distribution, morphology, purity, quantity, by employing environment friendly economical processes have always been a challenge for the researchers [15].

1.5 Thin Film Deposition Methods

Based on the nature of deposition process the methods employed for thin film deposition can be broadly classified into two groups i.e. Physical and chemical methods [16]. In physical methods the film material is moved as of form of energy to the substrate, this technique is widely used in one-component films, like metal films. We have vacuum evaporation and sputtering, where the deposition takes place after the material to be deposited has been transferred to a gaseous state either chemical film fabrication methods involve chemical reactions and the precursors are mostly components undergoing reaction at the substrate surface or in the vicinity of the substrate. We have the gas phase chemical processes and solution techniques [17]. This method is shown in figure(1.3).

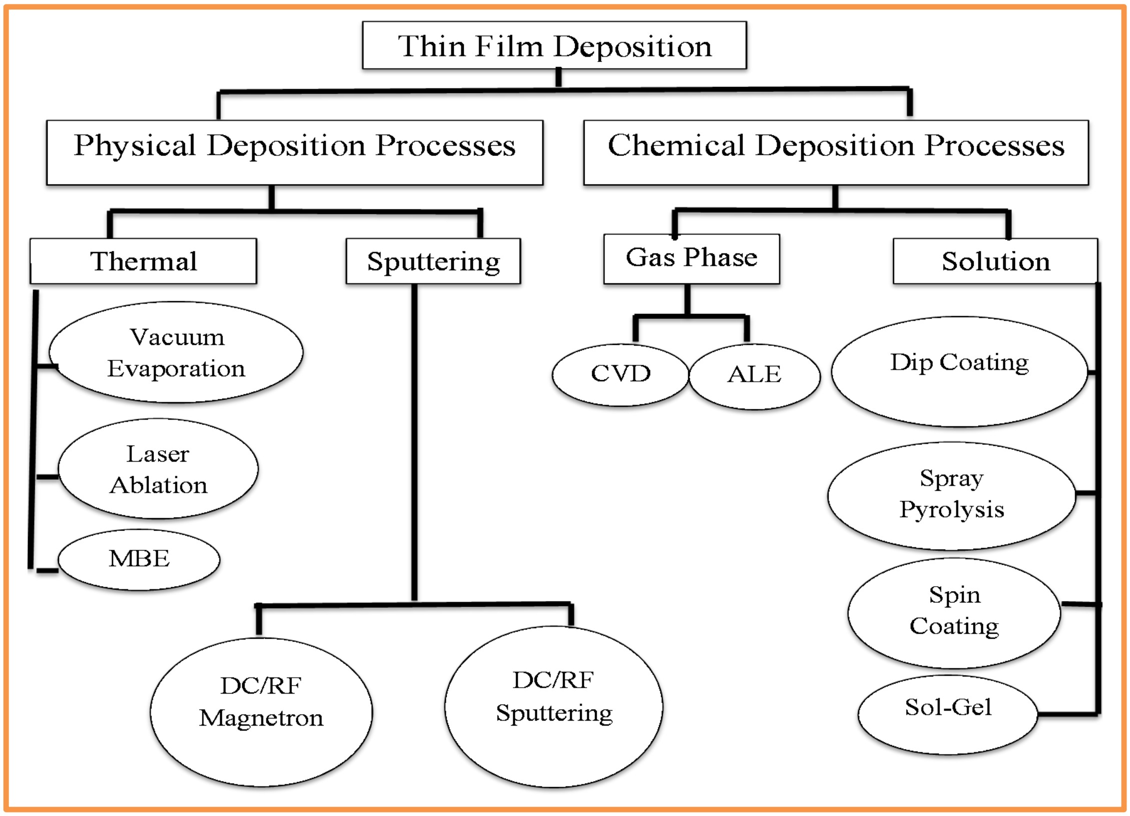

Figure (1.3): Classification of Thin Film Deposition Processes Physical and Chemical Methods[20].

1.6 Literature Survey

This section includes previous studies done by many researchers and the results of their work:

In (2007) H. Peng ***et al*.** [18] they obtained so far in the range of many reasons having been advanced for low performance, barrier height measurements in various schottky barrier solar cells have shown that values are always in the range (0.7-0.9) eV regardless of the metal except for the case of gold and silver which form ohmic contacts **.**

H. Lu ***et al*.** (2009) [19] cuprous oxide (Cu_2O) and cupric oxide (CuO) thin films were deposited on glass substrates at different oxygen partial pressures by direct-current reactive magnetron sputtering of pure copper target in a mixture of argon and oxygen gases. Oxygen partial pressure was found to be a crucial parameter in controlling the phases thus, the physical properties of the deposited copper oxide thin films. Single-phase Cu_2O thin films with cubic structure were obtained at low oxygen partial pressure between (0.147) Pa and (0.200) Pa while higher oxygen partial pressure promoted the formation of CuO thin films with base-centered monoclinic structure. Polycrystalline Cu_2O thin films deposited with oxygen partial pressure at (0.147) Pa possessed the lowest p-type resistivity of (1.76) Ω cm as well as an optical band gap of (2.01) eV.

Y.S. Lee ***et al*.** (2011) [20] studied the cuprous oxide Cu_2O as a promising earth-abundant semiconductor for photovoltaic applications. We report Hall mobility's of polycrystalline Cu_2O thin films deposited by reactive dc magnetron sputtering. High substrate growth temperature enhances film grain structure and Hall mobility, temperature-dependent Hall mobilities measured on these films are comparable to monocrystalline Cu_2O at temperatures above (250) K, reaching (62) cm^2 /Vs at room temperature, at lower temperatures, the Hall mobility appears limited by carrier scattering from ionized centers. These observations indicate that sputtered Cu_2O films at high substrate growth temperature may be suitable for thin-film photovoltaic applications, cuprous oxide Cu_2O a compound semiconductor with a direct band gap of (1.9-2.1) eV, is a promising material for thin-film photovoltaic applications due to its elemental abundance in the earth's crust and nontoxicity.

R.Sahay ***et al.*** November (2012) [21] reported the electrospun copper based composite nanofibers were synthesized using the copper acetate/polyvinyl alcohol/water solution as starting material. Synthesized composite nanofibers were sintered at (500) C to obtain CuO nanofibers. XRD, FTIR and XPS techniques were used to confirm the presence of pure CuO nanostructures. The effect of annealing cycle on the crystalline structure of the CuO nanofibers was analyzed and observed that the decrease in crystallite size with an increase in the dwelling time improved the orientation of the CuO crystallite. The blue-shift in the band-gap energies of CuO nanofibers is observed as a result of quantum confinement from bulk CuO (1.2) eV to one dimensional (1D) nanostructures (1.746) eV. The catalytic activity of the CuO fibers for the degradation of methyl orange was carried out and as a blocking layer in ZnO based DSSC was fabricated and observed a (25)% increase in the current density.

V.V. Tyagi ***et al.*** (2013) [22] solar photovoltaic PV technology is one of the renewable technologies which have a potential to shape a clean, reliable, scalable and affordable electricity system for the future, considering this fact, all over the world governments are encouraging the development and deployment of solar (PV) technology, a wide range of photovoltaic(PV) materials are available world-wide, globally, there are hundreds of companies involved in the manufacturing of (PV) modules with varying efficiencies and limitations.

T. Dimopoulos ***et al.*** (2014) [23] studied hetero-junction solar cells were fabricated by electrochemical deposition of p-type, cuprous oxide (Cu_2O) absorber on sputtered, n-type ZnO layer. They found open circuit voltage (V_{OC}), short circuit current density (j_{SC}), fill factor (FF) and power conversion efficiency (η) of the as deposited cells are (0.37)V, (3.71) mA/cm^2, (35.7)% and (0.49)%, respectively. A general improvement of the hetero-junction and bulk materials quality is observed, reflected upon the smallest influence of the shunt and series resistance on the transport properties of the cells in dark and under illumination.

M.Gul ***et al*.** (2016) [24] electricity systems worldwide are changing. Global demand for, and dependence on electricity is increasing and, as environmental concerns become more pressing, so does the focus on the reduction of greenhouse gas emissions, this is resulting in a move towards a decarbonized electricity system based on a large volume of variable renewables generation, predominantly delivered by wind and solar photovoltaic (PV).

V. Kanna ***et al*.** (2018) [25] state that the solar energy is the best source to make a revolution in energy field. The above review shows comfortable proof to make that revolution in energy, when the economics is driving the energy and electricity industries to develop more renewable-energy technologies, which will also create ancillary wealth, security, and environmental benefits around the world, these social benefits are potentially vast and should be encouraged through progressive government policies as well as coordinated industry efforts, thoughtful investments in attention and money made today by industry and government are highly likely to accelerate this change and bring dramatic financial and social returns**.**

D.Naveena ***et al*.** (2019) [26] show that the CuO thin films have been prepared using various source materials such as $Cu(NO_3)_2{\cdot}3H_2O$, $CuCl_2{\cdot}2H_2O$ and $Cu(CH_3COO)_2{\cdot}H_2O$ by chemical spray pyrolysis technique. The (XRD) result shows an increased crystallite size for Cu-N compared with Cu-Cl and Cu-A films. Good optical absorption in the visible region is observed for all CuO films and Cu-

N film illustrates high absorption coefficient in the order of (5.7 × 105) cm^{-1}. From (SEM) analysis, flake like morphology is observed for Cu-N and Cu-A films. The good electrical property i.e. High conductivity (0.0611) Scm^{-1} and carrier concentration (2.287×1017) cm^{-3} is observed for Cu-N films. From I-V measurement, it is observed that the high current for Cu-N (16.6) μA than Cu-Cl (2.3) μA and Cu-A (10.7) μA. All CuO films are photo-responsive under solar light exposure, which is due to high absorption coefficient that leads to higher photocurrent (20.5) μA for Cu-N film. The best solar cell performance is obtained for Cu-N film which shows an efficiency of (0.31)%.

A.N.Tuama ***et al*.** (2020) [27] prepared pure cuprous oxide and silver nanoparticles doped cuprous oxide (0.02, 0.04, 0.06) wt.% films via thermal evaporation technique with a thickness of 60 nm. The grain size was found to be in between (9.2-18.4) nm and the optical band gap of the samples was found to be in between (2.79 and 3.42) eV which was the main factor in manipulating and improving the Cu_2O optical properties by doping. They studied the effect of the Ag doping on the Cu_2O properties, it was obvious and positively influenced by solar cell efficiency improvement. Optimization of the deposition conditions and doping process led to enhanced solar cell performance.

S. Kawanishi ***et al*.** (2021) [28] fabricated a p-n homojunction SnS solar cell by the deposition of p-type SnS polycrystalline thin films on large n-type SnS single crystals. They found that p-type thin films consist of columnar grains that grow along the <100> direction, which is the same orientation as the n-type single crystal and the interface of the p-n homojunctions is void-free and compositionally sharp. They obtained SnS homojunction solar cell achieves an open-circuit voltage (V_{OC}) of (360) mV. Once the device structure of the homojunction cell is optimized to efficiently collect the photo generated carriers and achieve a comparable J_{SC} as the conventional heterojunction cells (≈25) mA cm^{-2}, high η exceeding (4 -5) % will be realized with improving the V_{OC}.

M.E.H. Attia ***et al.*** (2022) [29] they achieve the highest freshwater productivity from the hemispherical solar distillers by combining two of the most effective modifications, namely, use of CuO nanoparticles to increase the evaporation rate, and use of glass cover cooling technology to increase the condensation rate. To obtain the influences of combining two effective modifications on the productivity of hemispherical distillers, three hemispherical distillers were constructed and tested at same climate conditions. The results presented that the combination between two effective modifications (CuO nanoparticles with weight ratio (0.3)% and glass cover cooling technology) represents the good option which improving the freshwater productivity.

1.7 Aims of the Study

The aims of this study can be listed as follows:

1. Preparation CuO and Cu_2O-doped CuO thin films via thermal evaporation technique with nano thickness, high homogeneity, and covering all the substrate.
2. Studying the homogeneity via scanning electron microscopy and Atomic force microscopy.
3. Fabricating solar cell from the prepared thin films and study the effect of Cu_2O content on its efficiency.

2.1 Introduction

This chapter focuses on the theoretical parts measurements; structural, optical, electrical for CuO:Cu_2O thin films. This chapter gives a theoretical review including all the relations, scientific explanations, optical properties of crystalline semiconductors (the optical constants**,** fundamental absorption edge, electronic transitions), electrical properties (hall effect, resistivity and current-voltage (I-V) characteristic.

2.2 Basic Theory of Applied Techniques of Thin Film

In the last years , the advancement in science has taken place with the discovery of new materials. Characterization is an important to development of exotic materials. The complete characterization of any material consists of phase analysis, structural, and surface characterization. In this section different analytical techniques are used to characterize thin films are described.

2.3 Structural and Morphological Characterization

A wide variety of characterization techniques were used to evaluate the material quality of the thin films before using the films in applications, the morphology of surface thin films was studied by atomic force microscopy (AFM) and (XRD). The structural properties of the films were studied by scanning electron microscopy (SEM).

2.3.1 Atomic Force Microscopy (AFM)

The atomic force microscopy (AFM) was invented in 1986 by Binnig, Quate and Gerber. (AFM) mode to use is based on the surface characteristics of interest and on the hardness/stickiness of the sample [30].

Atomic force microscopy is a high-resolution imaging technique where a small probe with a sharp tip is scanned back and forth in a controlled manner across a sample to measure the surface topography at up to atomic resolution. Atomic force microscopy techniques encompass a variety of scanning modes that enable nan scale characterization of different material properties such as electrical, magnetic properties. With AFM, one can measure the force between atoms at the tip and the sample, which are located as close as (0.1–100) nm [31].

Atomic Force Microscopy principles include:

1. Surface Sensing :An AFM uses a cantilever with a very sharp tip to scan over a sample surface.
2. Detection Method :A laser beam is used to detect cantilever deflections towards or away from the surface.
3. Imaging :An AFM images the topography of a sample surface by scanning the cantilever over a region of interest [30].

Figure (2.1) explains the block diagram of AFM. The AFM consists of a micro scale cantilever with a sharp tip (probe) at its end that is used to scan the specimen surface. The cantilever is typically silicon (Si) or silicon nitride (Si_3N_4) with a tip radius of curvature on the order of nanometers. The (AFM) works by scanning a fine ceramic or semiconductor tip over a surface much the same way as a phonograph needle scans a record.

When the tip is brought into proximity of a sample surface, Van der Waals forces between the tip and the sample lead to a deflection of the cantilever. The magnitude of the deflection is captured by a laser that reflects an oblique angle from the very end of the cantilever [32].

A plot of the laser deflection versus tip position on the sample surface provides the resolution of the hills that constitute the topography of the surface. The AFM can work with the tip touching the sample (contact mode), or the tip can tap across the surface (tapping mode) much like the cane of a blind**[32].**

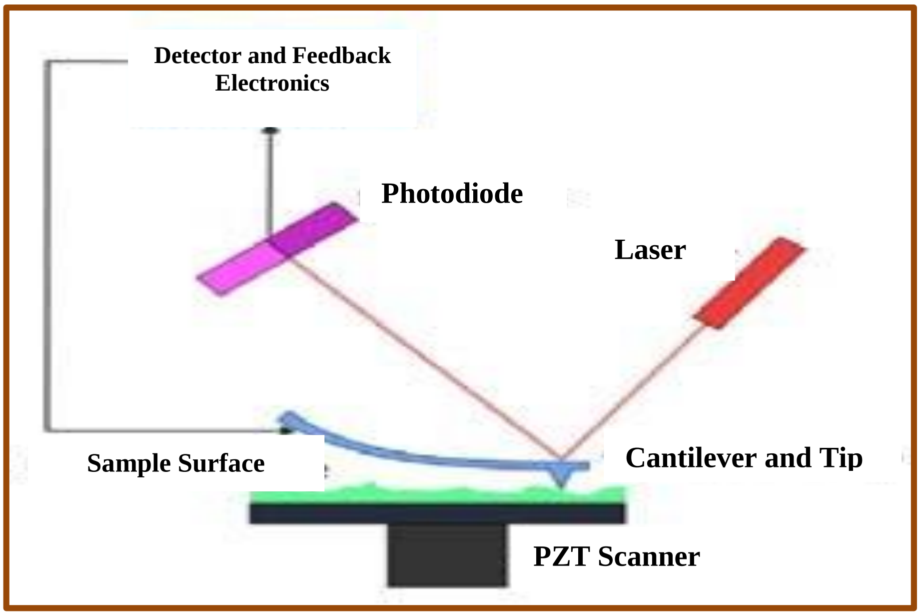

Figure (2.1): Block Diagram of Atomic Force Microscopy(AFM) [32].

2.3.2 X-ray Diffraction (XRD)

X-ray is a rapid analytical technique primarily used for determining the atomic structure of a crystalline material and can provide information on unit cell dimensions. The analyzed material is finely ground, homogenized, and average bulk composition, which is used in X-rays are electromagnetic ray. In diffraction applications, only x-rays with short wavelengths are used [33,34].

X-rays interacts with electrons in the atom, when photons collide in x-rays with electrons, some photons of the falling beam deviate from their direction uses x-ray diffraction for purpose recognition of crystalline systems [35].

X-ray diffraction is based on constructive interference of monochromatic x-rays and a crystalline sample, these X-rays are generated by a cathode ray tube, filtered to produce monochromatic radiation, collimated to concentrate, and directed toward the sample. The interaction of the incident rays with the sample produces constructive interference and a diffracted ray when the conditions satisfy Bragg's law [36]:

$$2d_{hkl}\sin\theta=n\lambda \qquad (2.1)$$

$$d_{hkl}=\frac{a_\circ}{\sqrt{h^2+k^2+l^2}} \qquad (2.2)$$

Where (n) is integer that shows the order of the reflection, (θ) is Bragg's angle, (λ) is the wavelength of the x-ray beam, (d) is inter-planar distant, (hkl) are millar index, $(a_\circ)$The lattice constants. The bragg's diffraction is represented in Figure (2.2).

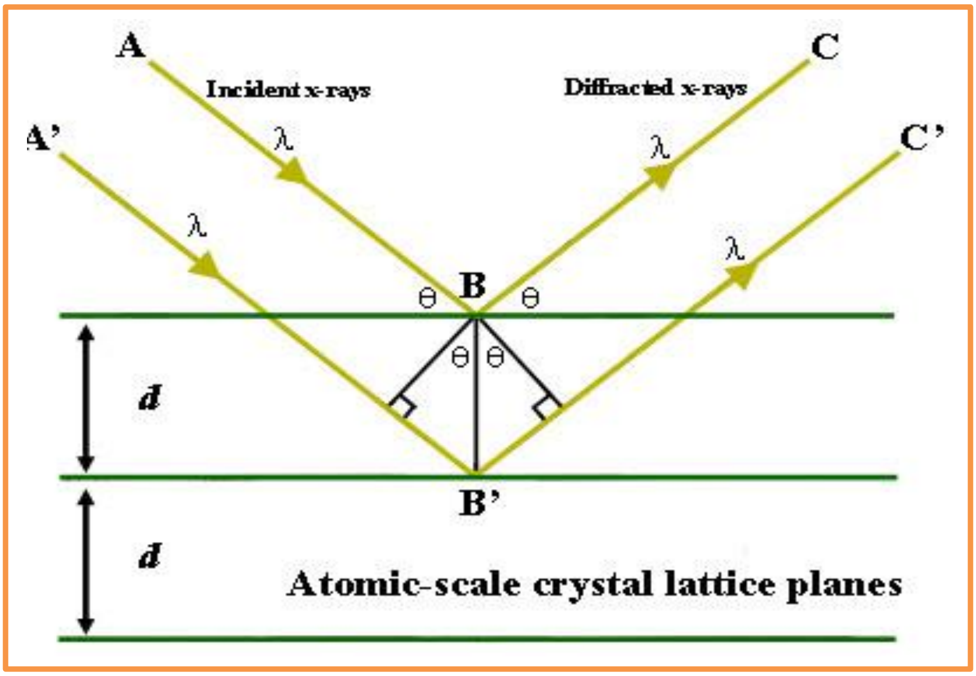

Figure (2.2): Bragg's Diffraction Diagram[36].

2.3.2.1 Parameters' Calculation

Normally, XRD is used to calculate different parameters, which could be used to clarify the studies of the deposited films, including:

a- Full Width at Half Maximum (FWHM) (β).

Full width at the half of the maximum intensity (FWHM) of the preferred orientation (peak), which equal to the width of the line profile (radian) at the half of the maximum intensity [37].

b- Average Crystallite Size (Dav).

The crystallite size (D) can be estimated by Debye Scherer formula [38]:

$$D = 0.9\lambda /\beta \cos\theta \tag{2.3}$$

Where λ is the x-ray wavelength (Å) , β is the full width at the half of the maximum intensity (FWHM) (radian), θ is Bragg diffraction angle of the XRD peak (degree).

2.3.3 Scanning Electron Microscopy (SEM)

The scanning electron microscopy (SEM) is one of the most versatile instruments available for the examination and analysis of the microstructure morphology and chemical composition characterizations. It is necessary to know the basic principles of light optics in order to understand the fundamentals of electron microscopy, the unaided eye can discriminate objects subtending about (1/60°) visual angle, corresponding to a resolution of ~0.1 mm (at the optimum viewing distance of 25 cm). Optical microscopy has the limit of resolution of (~2,000) Å by enlarging the visual angle through optical lens [39].

The electrons are produced by a thermal emission source by using it, we can estimate the diameter, length, thickness, density, shape and orientation of the nanostructures[40].

The SEM machine consists of the following components: A source to generate electrons of high energy, it is called electron gun, column down for travelling the electrons through two or more electromagnetic lenses, deflection system consists of scan coils, electron detector for backscattered and secondary electron, a chamber for the sample. Computer system consists of viewing screen to display the scanned images and keyboard to control the electron beam. Magnifications ranging from (10) to in excess of (50000) times are possible, also very great depths of fields, as shown in Figure (2.3), accessory equipment permits qualitative and semi quantitative analyses of the elemental composition of very localized surface area [41].

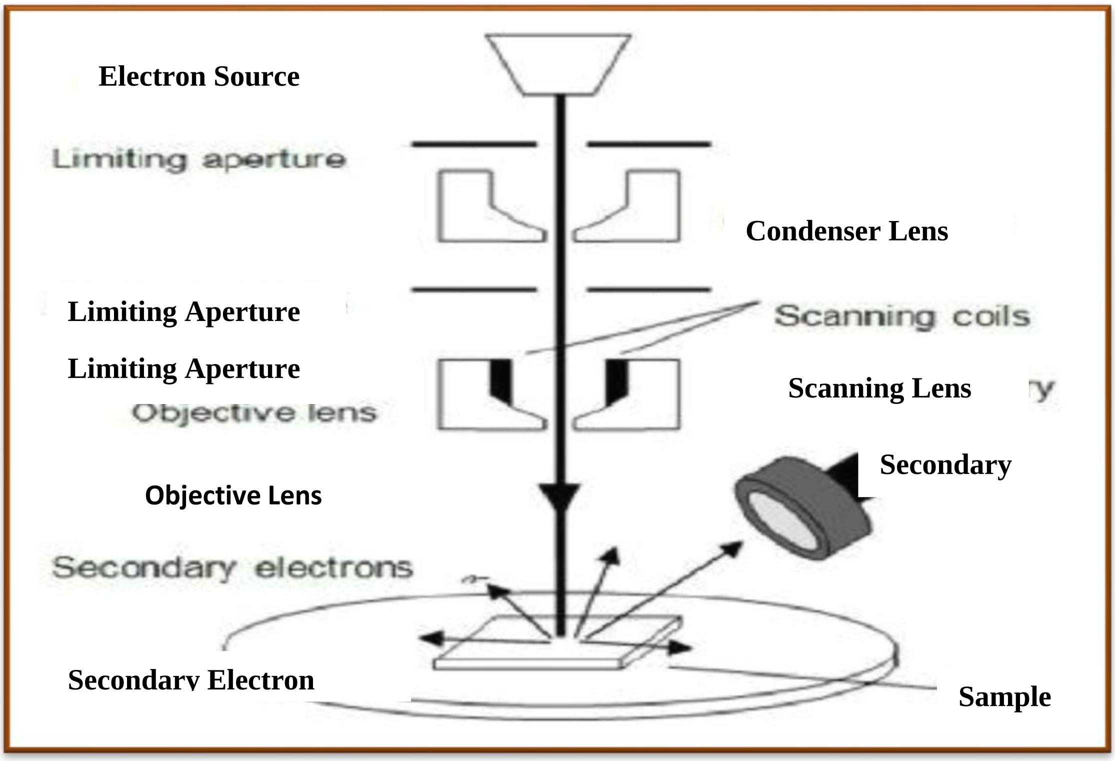

Figure(2.3): Schematic of Scanning Electron Microscopy (SEM) [42].

2.3.4 Thermal Evaporation

Thermal evaporation is a common method of physical vapor deposition (PVD). It is one of the simplest forms of PVD and typically uses a resistive heat source to evaporate a solid material in a vacuum environment to form a thin film. Usually low pressures are used, about(10^{-6} or 10^{-5})Torr. to avoid reaction between the vapor and atmosphere. At these low pressures. Figure (2.4) explains the configuration of a basic coating system [39,43].

The materials to be applied with thermal evaporation techniques can be atomic elements including both metals and nonmetals or can be molecules such as oxides and nitrides. The object to be coated is referred to as the substrate, and can be any of a wide variety of things such as semiconductor wafers, solar cells, optical components, or many other possibilities [40].

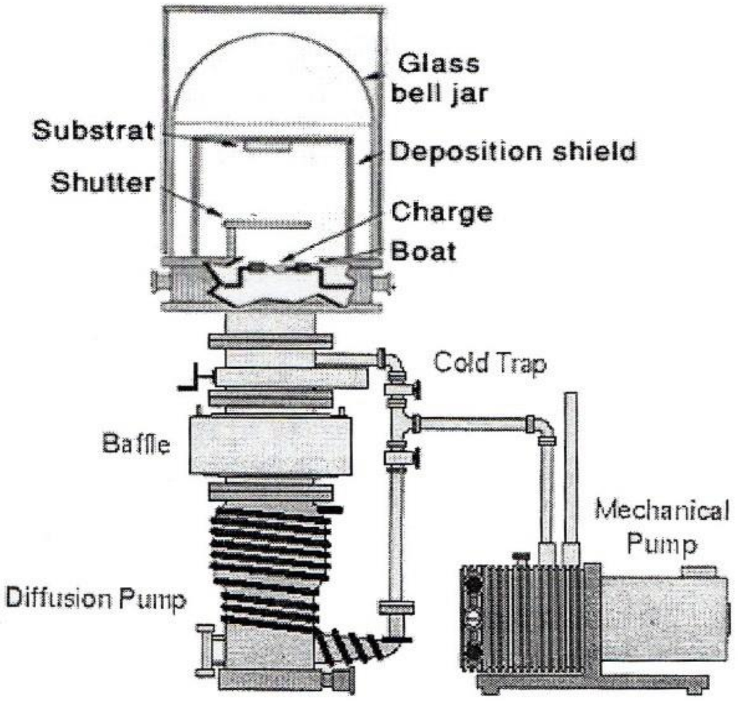

Figure(2.4): Configuration of A Basic Coating System[39,43].

2.4 Optical Properties of Semiconductors

The optical properties of a semiconductor are related to the intrinsic effect. Based on the intrinsic location of the top of the valence band (V.B) and the bottom of the conduction band (C.B) in the band structure, the electron–hole pair generation occurs directly or indirectly [44,45].

The semiconductor absorbs photon from the incident beam, the absorption depends on the photon energy. The absorption is associated with the electronic transition between the V.B and the C.B in the material starting at the absorption edge which corresponds to minimum energy difference (E_g) between the lowest minimum of the C.B. And the highest maximum of the V.B. If the photon energy (hν) is equal to energy gap (E_g) then, it can interact with a valence electron, elevates the electron into the C.B and creates an electron–hole pair. The maximum wavelength (λc) of the incident photon which creates an electron–hole pair is defined as [46].

$$\lambda_c(\mu m) = \frac{hc}{E_g} = \frac{1.24}{E_g(eV)} \tag{2.4}$$

Where: h is Plank's constant (6.625×10^{-34} J.s), c is velocity of light, and E_g is the optical energy band gap.

The intensity of the photon flux decreases exponentially with distance through the semiconductor according to the Ber lamberts equation [47].

$$I_T = I_o \exp(-\alpha t) \tag{2.5}$$

Where: I_o and I_T : are the incident and the transmitted photon intensity in (W/cm^2) respectively, t: is the thickness of the sample in (cm) and α: is the absorption coefficient, which is defined as the relative number of photons absorbed per unit distance of semiconductor.

2.4.1 The Fundamental Absorption Edges

The fundamental absorption refers to band-to-band or to excitation transitions (i.e. the excitation of an electron from the valence band to the conduction band), it manifests itself by a rapid rise in absorption. Which can be used to determine the energy gap of the semiconductor. Absorption regions can be classified into three regions [48].

a) High Absorption Region

This region is shown in Figure (2.5). In part (A), the magnitude of absorption coefficient (α) is larger or equal to (10^4 cm^{-1}). From this region the magnitude of forbidden optical energy gap (E_g^{opt}) can be introduced.

b) Exponential Region

This region is shown in figure (2.5). The value of absorption coefficient (α) is equal to ($1\ cm^{-1} < \alpha < 10^4\ cm^{-1}$). It refers to the transition between the extended levels from the (V.B) to the local levels in the (C.B) and from local levels in (V.B) to extend the levels in (C.B).

c) Low Absorption Region

The absorption coefficient (α) in this region is very small, it is about ($1\ cm^{-1}$). The transition happens in this region because of density of state in mobility gap resulted from structural faults, as in Figure (2.5).

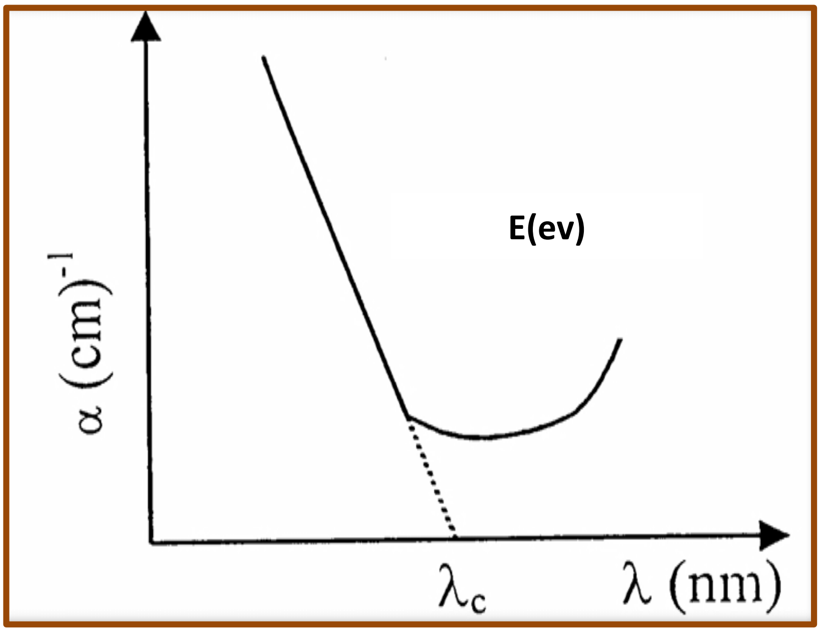

Figure (2.5): The Variation of Absorption Edges With Absorption Regions [47].

2.4.2 Electronics Transition

The absorption of radiation, which leads to electronic transition between the valence and conduction bands, is split into direct and indirect transition as shown in Figure (2.6) [49].

The direct transition happens in semiconductors when the bottom of (C.B) is exactly over the top of (V.B). This means that they have the same value of wave vector, i.e. ($\Delta K=0$) in this state the absorption appears when ($h\upsilon=E_g^{opt}$). This transition type is required for the law's of conservation of energy and momentum. These direct transitions have two types [45]:

a) Allowed Direct Transitions

The transition happens from the top points in the (V.B) and the bottom point in the (C.B) at the same wave vector $\Delta K=0$ for conservation of momentum, as shown in Figure (2.6.a). This transition is described by the following relation [46]:

$$\alpha h\nu = B' \, (h\nu - E_g)^{1/2} \qquad (2.6)$$

Where υ: is the frequency in (Hz), B' : constant depended on type of material (is inversely proportional to amorphousity), r =1/2 for Allowed direct transitions.

b) Forbidden Direct Transitions

If the transition occurs between states of the same wave vector, that is not equal to zero, this transition happens from near top points of (V.B) and the bottom points of (C.B), as shown in Figure (2.6.b). The transition is called forbidden direct transition, the absorption coefficient for this transition type is given by [46]:

$$\alpha h\nu = B' \, (h\nu - E_g)^{3/2} \qquad (2.7)$$

Also indirect transition have two type of transition **:**

c) Allowed Indirect Transitions

For the indirect transition in this case the bottom of (C.B) is not over the top of (V.B) in curve (E-K). The electron transits from (V.B) to (C.B) is not perpendicularly where the value of the wave vector of electron before and after the transition is not equal to zero ($\Delta K \neq 0$). This transition type happens with helpful of particle called "Phonon", for conservation of the energy and momentum law then, a phonon is necessary to conserve the momentum, therefore [50]:

$$h\nu = E_g \pm E_p \qquad (2.8)$$

Where: E_p is the energy of an absorbed or emitted phonon, is (-) when phonon absorption, and (+) when phonon emission. For an allowed indirect transition, the transition occurs from the top of the valence band to the bottom of the conduction band as shows in Figure (2.6.c), so that [51]:

$$\alpha h\nu = B' \left(h\nu - E_g\right)^2 \qquad (2.9)$$

(d) Forbidden Indirect Transitions

The forbidden indirect transitions occur from any point near the top of (V.B) to any point other than the bottom of the (C.B), as shown in Figure (2.6.d). The absorption coefficient for transition with a phonon absorption is given by [52]:

$$\alpha h\nu = B' \qquad (2.10)$$

Experimentally, it is possible to differentiate between direct and indirect processes by the level of the absorption coefficient; α takes values from (10^4 to 10^5) cm^{-1} for direct transitions and (10 to 10^3) cm^{-1} for indirect transitions at the absorption edge.

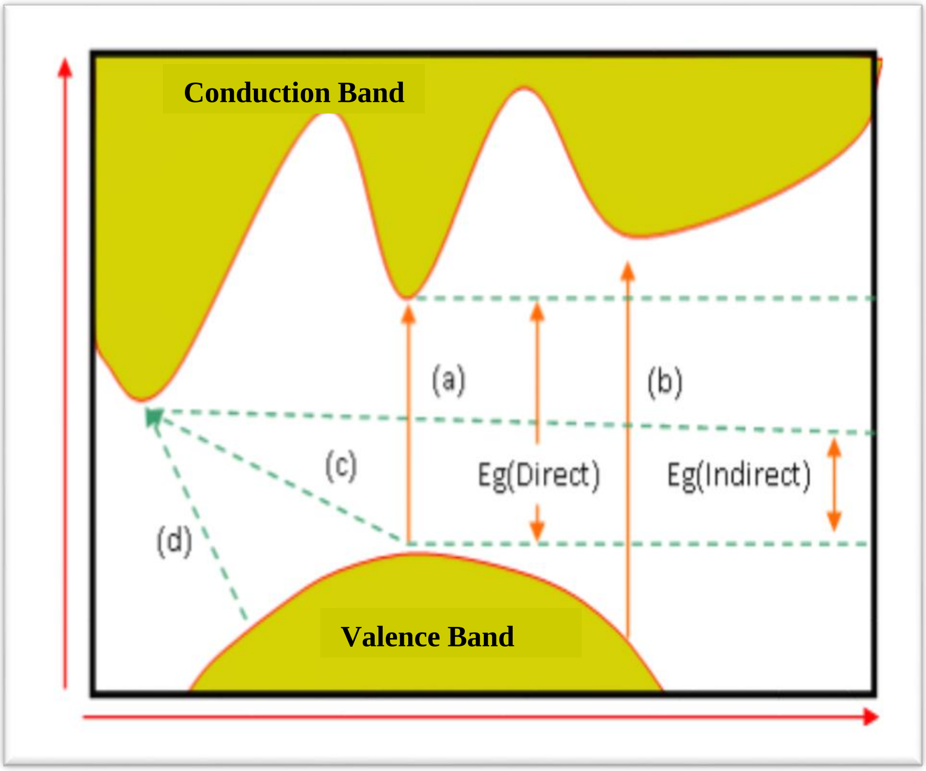

Figure(2.6): The Transition Types [53].

(a) Allowed Direct Transition. **(c) Allowed Indirect Transition.**

(b) Forbidden Direct Transition. **(d) Forbidden Indirect Transition.**

2.4.3 Optical Transmittance (T)

It is the ratio between the intensity of the beam from the film I_T to the intensity of the beam falling on the film I_o and expressed as [53].

$$\mathbf{T} = \frac{\mathbf{I_T}}{\mathbf{I_\circ}} \tag{2.11}$$

When a beam of light rays falls on the semiconductor, a portion of the rays will be carried out from the film. The amount of x-rays depends on the energy gap, the thickness of the film and the ratio of impurities.

2.4.4 Optical Absorbance (A)

It is defined as the ratio between absorbed light intensity (I_A) by material and incident intensity of light (I_o) [54].

$$A = \frac{I_A}{I_\circ} \tag{2.12}$$

We can also find a transmittance as a function of wavelength through the exponential relationship for both absorbance and transmittance which

$$A = \mathrm{Log}\frac{1}{T} \tag{2.13}$$

2.4.5 Optical Reflectance

It is known as the ratio between the intensity of the reflected radiation and the intensity of the radiation falling at the boundary between the two centers, and can be defined by the amount of energy conservation law [55]:

$$R + A + T = 1 \tag{2.14}$$

2.4.6 Optical Constants

There are many ways to find the optical constants including absorption coefficient, refractive index, extinction coefficient, the complex of dielectric constant (real and imaginary) and optical energy.

1. Absorption Coefficient (α)

It is defined as the percentage of decrease in the amount of radiation energy falling for the unit of that distance towards the propagation of the wave within the center, and depends on the amount on the energy gap, the types of transitions and the radiation energy falling by relationship [56]:

$$\alpha = \frac{2.303\ \mathrm{A}}{\mathrm{t}} \qquad (2.15)$$

Where A is the absorbance and t is the sample thickness.

2. Refractive Index (n)

The refractive index is defined as the ratio between the speed of light in vacuum (c) and the speed of light in the matter, calculated from the amount of the following relationship[57].

$$\mathrm{n}=[\frac{4\mathrm{R}}{(\mathrm{R}-1)^2} - \mathrm{k}^2\ ]^{1/2} - \frac{(R+1)}{(\mathrm{R}-1)} \qquad (2.16)$$

Where (R) is the reflectance.

3. Extinction Coefficient (k)

The coefficient of inertia represents the amount of photons absorbed by the film, that is, the energy absorbed by the electrons of the material, and expresses the following relationship [58]:

$$\mathrm{k} = \frac{\alpha\lambda}{4\pi} \qquad (2.17)$$

Where (λ) is the wavelength of the incident radiation and (α) absorption coefficient.

4. Complex Dielectric Constant

The insulation constant is defined as the absorption of energy in the material due to the interaction of light with the charges of the medium, and that leads to the polarization of the center charges, and this polarization is called insulation constant known as the following relationship [59].

$$\boldsymbol{\varepsilon} = \boldsymbol{\varepsilon}_{\mathbf{r}} + \boldsymbol{i}\boldsymbol{\varepsilon}_{\mathbf{i}} \qquad (2.18)$$

For the calculation of the dielectric constant in its two parts, one can use the following expressions[59].

$$\boldsymbol{\varepsilon}_{\boldsymbol{r}} = \mathbf{n}^{2} + \mathbf{k}^{2} \qquad (2.19)$$

$$\boldsymbol{\varepsilon}_{\mathbf{i}} = \mathbf{2nk} \qquad (2.20)$$

ε_r: the real part of the dielectric constant, ε_{i}: the imaginary part of the dielectric constant

2.5 Hall Effect

The advantage of a Hall impact measurement measures and determines the concentration of charge carriers in the volume unit and its type as in Figure(2.7), as well as the charge-bearing charge calculation [60].

If a magnetic field (B) has a vertical effect on the semiconductor with a constant current (I), a transverse voltage difference will be created via the semiconductor called Hall voltage and the resulting electric field is called Hall field. This field arises because of the deviations of the moving electrons towards one side of the semiconductor by the magnetic field, and this deviation continues and the charge carriers accumulate until they reach the state of equilibrium, where both the force of the sphere and the force arising from the magnetic field are equal.

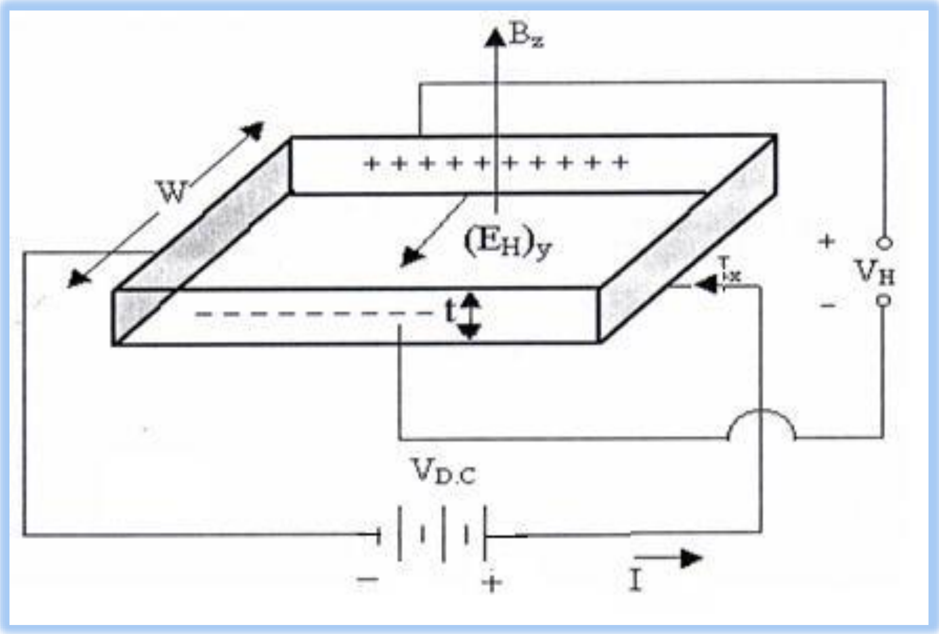

Figure(2.7): Hall Effect Measurement Circuit [60].

The Hall coefficient can be calculated from the following relationship**[60]**:

$$R_H = V_H/I_H \,.t/Bz \tag{2.21}$$

Where R_H is Hall coefficient, V_H Hall voltage, I_H Hall current, t the thickness of the sample[60].

The Van der Pauw method which was promoted by L. J. Van der Pauw in 1958, it is used to measure the hall effect, which characterizes a sample of semiconductor material and can be successfully completed with a voltmeter current source, and a magnet, where the signal is a negative coefficient of the semiconductor, the type of n-type and if positive is a of p-type [61].

$$R_H = \pm r/qn \tag{2.22}$$

Where n : Concentration of carriers, q : Electron charge and r : Factor scatterometer $r \leq 1$.

2.6 Solar Cell Work

When light (photons) is incident on a semiconductor surface, part of it is reflected and the rest is transmitted or absorbed, a photon with energy less than the band gap of the semiconductor does not contribute to the photovoltaic effect[61].

A photon with energy greater than the band gap is absorbed by the semiconductor and in turn leads to the formation of electron-hole pairs and these electron hole pairs are separated across the junction leading to the generation of current, there are some of the parameters that play an important role in the performance of a solar cell [61].

2.6.1 Resistivity (ρ)

The conductivity of semiconducting material in addition to being dependent on hole and electron concentration, is also a function of the charge carrier mobilities. The resistivity can be calculated from the relation [62]:

$$\rho = R_e \times A^* / L \qquad (2.23)$$

Where A* is the cross section area (film sheet) and L is the conductor length (inter electrode spacing), R_e is resistance of electron . The resistivity of the films related to the electric field and the current passing through the film is [62]:

$$\rho = E / J \qquad (2.24)$$

Where (E) is the electric field equals to (V/d), (V) is the applied voltage, (d) is the electrode spacing distance, and (J) is the current density equals to (I/A*).

It depends on the resistivity (or conductivity), that is on the carrier concentration (electrons or holes). It is affected by so many parameters or conditions mainly the doping, temperature, and deposition technique [62].

2.6.2 Mobility (μ)

Mobility is an important parameter for carrier transport because it refers to how strongly the motion of an electron is influenced by an applied electric field [66]:

$$\nu_n = \mu_n E \tag{2.25}$$

Analogous expression can be written for electrons in the conduction band and holes in the valence band respectively [67]:

$$\nu_p = \mu_p E \tag{2.26}$$

Where (μ_n) and (μ_p) are the electrons and holes mobility respectively, (E) is the electric field, (ν_n) is the electron drift speed and (ν_p) is the hole drift speed. The negative sign is removed in eq. (2.18) because the holes drift in the same direction as the electric field [66].

2.7 Current-Voltage (I-V) Characteristic

The solar cell is a photovoltaic transformer convert direct sunlight into an electric current which has been development of many technologies for the production of solar cells through the serial processes of physical, chemical and electrical processors [65]. The main parameters that are used to characterize the performance of solar cells are the peak power (P_{max}), the short-circuit current density (J_{sc}), the open-circuit voltage (V_{oc}), and the fill factor (F.F). These parameters are determined from the illuminated J-V characteristic as illustrated in Figure(2.8).

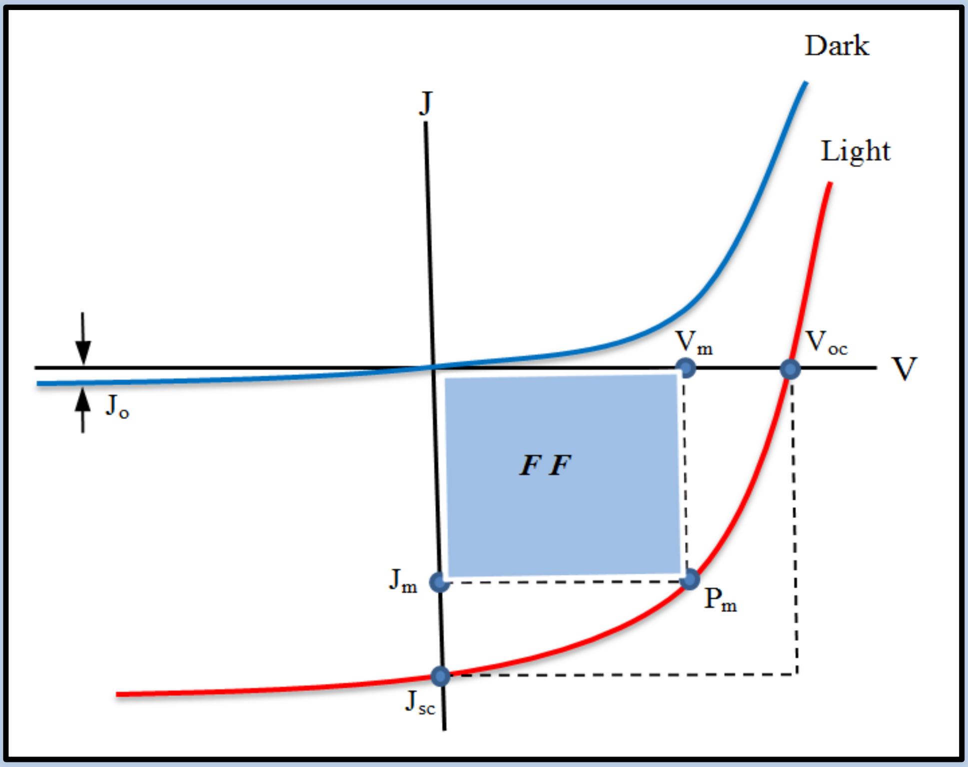

Figure(2.8): The Dark and Light I-V Curves for The Ideal Solar Cell [63].

The conversion efficiency (η) is determined from these parameters.

1. Open Circuit Voltage (V_{oc})

Open circuit voltage (V_{oc}) is the maximum voltage that the cell can deliver at zero current (i.e. the voltage produced when the load resistance is infinite), given by the relation [64]:

$$V_{oc}=\frac{kBT}{q}\ln(\frac{Isc}{Is}+1) \qquad (2.27)$$

Where BT is boltzman factor, q the charge of electron, Isc the short circuit current , Is the saturation current[64].

2. Short Circuit Current (I_{sc})

It is the maximum current that flows in the device at zero voltage (i.e. the current generated in the cell when the load resistance is zero) is given by the equation [65]:

$$I_{sc} = I_s[exp(qV_{oc} \backslash k_B T) - 1] + V_{oc} \backslash R_{sh} \tag{2.28}$$

The short circuit current is dependent on a number of factors which are:

1- The area of the solar cell,
2- The power of the incident light,
3- The spectrum of the incident light,
4- The absorption characteristics and the collection probability.

3. Fill Factor (F.F)

The F.F is defined as the ratio of the maximum power that can be derived from a solar cell to the product of the I_{sc} and V_{oc}, or this indicates the “squareness” or sharpness of the knee of the (I-V) curve, i.e. how well the maximum power rectangle fits the area covered by the (I-V) curve, this relation is given by[66]:

$$F.F = I_m\, V_m \backslash V_{oc}\, I_{sc} \tag{2.29}$$

4. The Conversion Efficiency (η)

This is the ratio of the power generated by the cell to the power of the incident light and expressed mathematically, as [67]:

$$\eta = P_m / P_{in} \times 100\% \tag{2.30}$$

Where ($P_m = P_{out}$).

3.1 Introduction

This chapter include on the experimental details used in fabrication and investigation of pure (CuO) and Cu_2O -doped CuO) thin films. This chapter is dedicated to the experimental part, which plays a significant role in determining the results. It begins with the deposition of $CuO:Cu_2O$ thin films by using vacuum evaporation method.

The techniques used for preparation and testing the structure of the thin films are the investigation about of the structural and morphological features by atomic force microscopy (AFM) and X-ray diffraction (XRD) and respectively, and the determination of grain size are presented. The optical measurements of thin films such as transmittance (T), absorbance (A), the absorption coefficient (α), optical energy gap (Eg), refractive index(n), extinction coefficient (k_o), and the dielectric constants (ε_r and ε_i). The electrical properties of the thin films such as Hall effect, current-voltage (I-V), and study of the experimental work is shown in Figure (3.1).

3.2 Work Scheme

The experimental procedure are shown in Figure (3.1) as a block diagram of the main steps that are followed in this work. It includes the steps of preparation and measurements for used chemical materials whose characteristics are summarized in this chapter

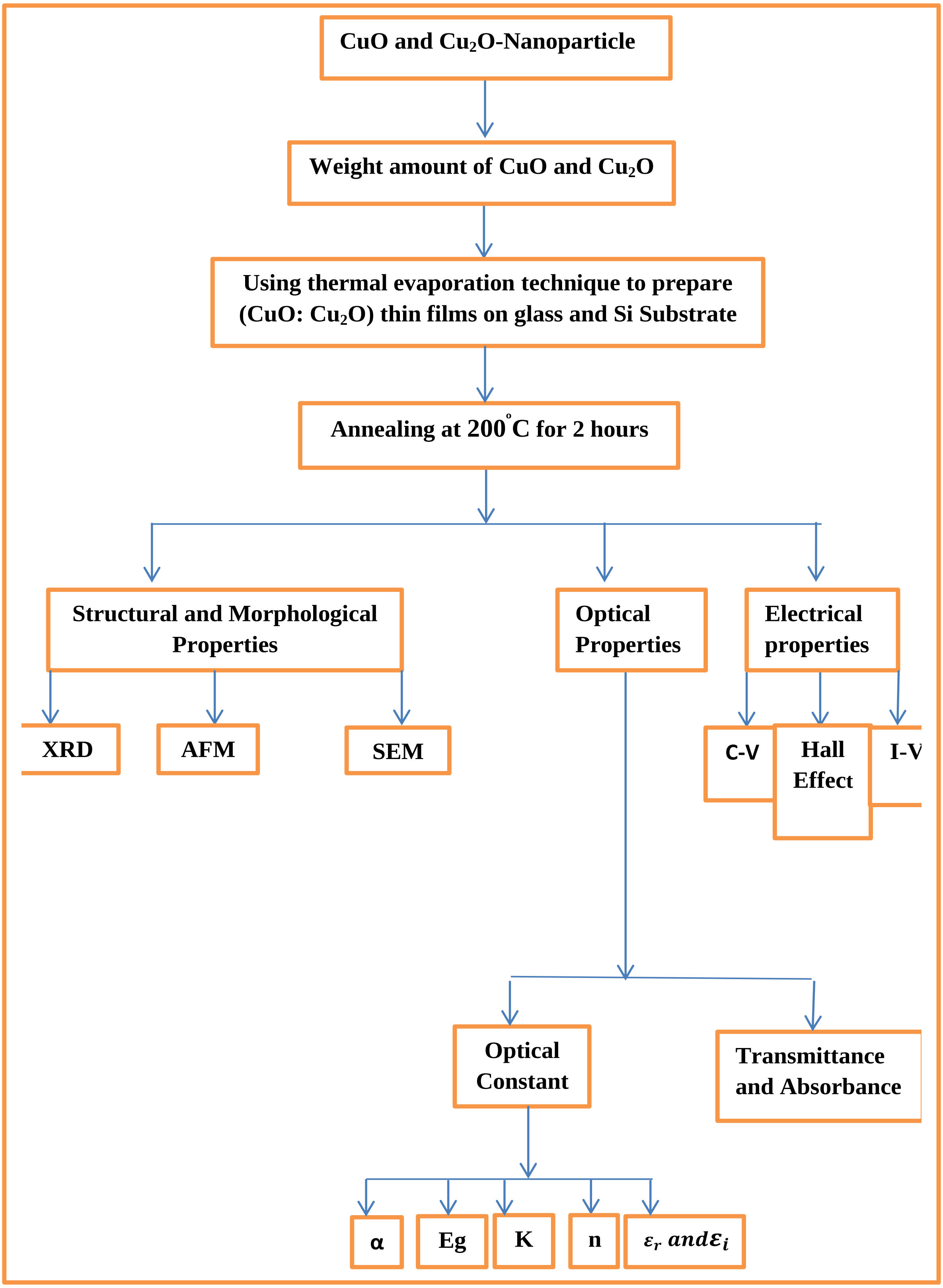

Figure(3.1) : Main Steps of the Work Scheme.

3.3 Matrix Material

Copper oxide (CuO) it was observed as powder from Zhengzhou dongyao nano materials Co. LTD china company, with nano grain size 50 nm, density 5.606 g/cm^3, color white, and high purity (99.99 %), in this work we used Copper oxide (CuO) of different weights to form films, a glass substrate was cleaned by distilled water and ethanol to remove surface contaminants and allowed to by completely dry, and the material was placed in a Molybdenum boat in modified thermal evaporation system (Edward C-306).

The experimental details used in fabrication and investigation of pure CuO and Cu_2O -doped CuO thin films with different doping ratio (0.002, 0.004, and 0.006) wt.% as shown in the Table (3.1). The chamber was covered tightly and pumped down to (1×10^{-7}) mbar. CuO annealed in the vacuum oven at temperature (200)℃ for one and two hours. The thickness was converging to be (75) nm.

Table (3.1): The prepared thin film of CuO:Cu_2O at thickness(75)nm.

CuO	Cu_2O
0.01	0
0.0098	0.0002
0.00096	0.0004
0.0094	0.0006

3.3.1 Cuprous Oxide (Cu_2O)

Cuprous oxide (Cu_2O) as a typical p-type semiconductor, has been one of the most intensively investigated binary transition metal oxide crystals decades [68].

Besides the well-known merits including low-cost, nontoxicity, abundance and easy synthesis, the tailored architectures of Cu_2O crystals have attracted great research interests because of their physicochemical properties for achieving various functions [69].

Especially, very exciting progresses in the fields of energy conversion, catalyst, sensor and chemical template with the involvement of Cu_2O have strongly stimulated the rapid development of Cu_2O with controllable size, shape, facet, defect, dopant and hetero-structuring[70]. Up to date, various Cu_2O micro-Nanocrystals with tailored architectures have been reported, such as three-dimensional solid architectures, hollow and porous structure, thin films, and low-dimensional nanostructures[71].

Lately, special focusing is devoted to copper, cuprous oxide (Cu_2O), and cupric oxide (CuO) NPs for their characteristic chemical and physical features. Nanoparticles of copper basis can be produced in different ways, such as thermal decomposition, chemical reduction, microwave-assisted, solvothermal and electrochemical synthesis, and by some physical methods[72]. These advantageous properties have made the copper oxide as common material in solar cell fabrication and photo electrochemical water-splitting application [73]. The potential for Cu_2O using in semiconducting devices has been recognized since, at least, 1920. Interest in Cu_2O revived during the mid-seventies in the photovoltaic community.

Several primary characteristics of Cu_2O make it potential material to be used in thin film solar cells: its non-toxic nature, a theoretical solar efficiency of about (9-11)%, an abundance of copper and the simple and inexpensive process for semiconductor layer formation. Therefore, it is one of the most inexpensive and available semiconductor materials for solar cells. In addition to everything else, cuprous oxide has a band gap of (2.0) Ev, which is within the acceptable range for solar energy conversion, because all semiconductors with band gap between 1 eV and 2 eV are favorable material for photovoltaic cells [76]. The physical properties of cuprous oxide are listed in Table (3.2).

Table (3.2):Physical properties of cuprous oxide (Cu_2O)[75].

Properties	**Values**
Structure	Cubic < 570 Orthorhombic > 570
Band gap	(3.40-4.00) eV
Refractive index	2.08 from α 2.35 from β
Resistivity	$1.6*10^4 \Omega.\ cm$
Molecular weight	$143.09 g/mol$
Boling point	1800℃
Melting point	1232℃
Density	$6.0 g/cm^3$
Dielectric constant	7×10^{-9}
Color	White powder

3.3.2 Silicon (Si)

In the 1879s advances in the passivation of both cell surfaces led to the first crystalline silicon solar cells with conversion efficiencies above 20%**.** Given the trend towards lower cost, but also lower quality (Si) materials such as block cast multicrystalline Si, ribbon Si or thin film polycrystalline Si, the most promising surface passivation methods identified to date are the fabrication of a (p-n) junction, the subsequent passivation of the resulting silicon surface with plasma silicon nitride as this material, besides reducing surface recombination and reflection losses, additionally provides a very efficient passivation of bulk defects [76].

Crystalline silicon photovoltaic (PV) cells are used in the largest quantity of all types of solar cells on the market, representing about 90% of the world total PV cell production in 2008. Crystalline silicon solar cells are also expected to have a primary role in the future PV market [77]. The physical properties of silicon are listed in Table (3.3).

Silicon is safe for the environment and one of the most abundant resources on Earth, representing 26% of crustal material. The abundance and safety of silicon as a resource grants the silicon solar cell a prominent position among all the various kinds of solar cells in the PV industry [78].

Table (3.3): Physical properties of silicon (Si)[79].

Properties	**Values**
Atomic weight	28,08 g/mol
Band gap	1.12 ev
Atomic number	14
Melting point	1414°C
Boiling point	3265°C
Melting enthalpy	9470 cal/at.g
Density	2.3296 g cm^{-3}
Electric resistivity	$85*10^{-6}$ (at 25°C)
Thermal conductivity	0.20 (at 20°C)

3.3.3 Copper Oxide (CuO)

Copper oxide is a defect semi-conductor but nowadays it is well established that Cu, O is a natural p-type semiconductor, whose carrier concentration depends on the amount of caution deficiency [80]. Copper (I) oxide (Cu,O), in particular, has been synthesized extensively in polycrystalline form by electrode position from solutions near room temperature, however, recently efficiency of (3)% has been reported [83].

The researches carried out during the mid-seventies and early eighties have now helped in revealing some of the mysteries surrounding this material and a perfect understanding of the various causes for the poor performance of Cu,O solar cells are now known [21]. Copper and copper oxide (metal-semiconductor) are one of the first photovoltaic cells invented [81]. CuO has a direct band-gap of (2.17) eV which is suitable for photovoltaic conversion theoretical calculations have predicted an electrical power conversion efficiency of approximately (9-12) %, the practical electrical power conversion efficiencies obtained by researchers, in the past, are below (2)% [82]. The physical properties of copper oxide are listed in Table (3.4).

Table (3.4):Physical properties of copper oxide CuO [84].

Properties	**Values**
Compound formula	CuO
Molecular weight	79.55 g/mol
Appearance	black to brown powder
Melting point	1201℃
Boiling point	2000° C
Density	6.31 g/cm^3
Solubility in H_2O	Insaluble
Exact mass	78.9245 g/mol
Band gap	2.17 ev

3.4 Substrate Preparation

Type and nature of the substrate are the influence parameters and have the most important effects on the properties of the deposited films. One type of substrates is used in this study, glass slides which were used to study the structural, electrical and optical properties of CuO thin films. First step glass slides and cleaning, the substrate used for deposits CuO thin films in this work was a microscopic glass slides. These glass slides substrates (8×2.5) cm^2 with (1) mm thickness were subjected to the following steps:

1- The substrates were cleaned by water and a detergent solution to remove any oil or dust that might be on their surface.

2- The substrates were immersed in a clean beaker containing distilled water.

3- The distilled water was replaced by pure alcohol and the previous step was repeated and the glass substrates were wiped with soft paper.

3.5 The Specification of Boat

Various types of sources were used for the evaporation. A spiral boat source of tungsten material were used for the (Al) evaporation to make electrodes, and molybdenum boat source was used for the deposition of (CuO) thin films as shown in Figure (3.2).

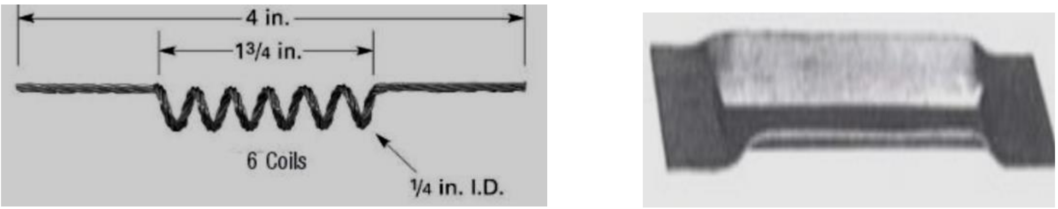

(a) (b)

Figure(3.2): (a) Spiral Tungsten Boat and (b) Molybdenum Boat.

3.6 The Coating Unit

The vacuum unit system, Edwards coating unit model Edwards-c has been used for the deposition of CuO thin films. The main constructions of the typical vacuum coating unit are shown in Figure (3.3).

Figure(3.3): Thermal Evaporation System.

The system is pumped down to a vacuum of (1×10^{-7}) mbar, an electric current was passed through the boat gradually to avoid breaking the boat. When the boat temperature reached the required temperature the deposition process starts with constant rate of deposition equal to (0.5) nm/s. After these steps, the current supply was switched off and the samples were left in the high vacuum, and then the air was entered to the chamber, and the films were taken out from the coating unit and kept in the vacuum desiccator until the measurements were made. All the samples were prepared under constant conditions (pressure, substrate temperature and rate of deposition); the main parameters that control the nature of the film properties had a thickness (75) nm.

In this work the evaporation processes have been performed at room temperature (RT) and the distance between the source and substrate was kept at(15) cm. This system is found in the Department of Physics/ College of Education for Pure Sciences/ university of Babylon.

3.7 Thin Film Growth

In the present work, thin films layers of copper oxide (CuO) have been obtained by doping cuprous oxide (Cu_2O) powder and, the deposition of $CuO:Cu_2O$ thin films were performed by electrical resistance heated thermal evaporation process. In this process, the electrical power is passed through the boat to create a vapor which travels in straight line paths to the substrate. In general, there are three steps in any vacuum deposition process, creation of an evaporate from the source material, transport of the evaporate from the source to the substrate and condensation of the evaporate on to the substrate to form the thin film deposited . In this work, the evaporation processes have been performed at room temperature (R.T). The pressure during the evaporation was approximated to (1×10^{-7}) mbar with a rate of deposition (0.5) nm.s^{-1}. The distance between the source and substrate was kept at (15) cm.

3.8 Solar Cell Preparation and Ohmic Contact

After evaporating $CuO:Cu_2O$ thin film on silicon wafer, p-n junction solar cell is formed and Ohmic contacts for the prepared films are produced by evaporating (Al) to forms solar cell electrodes.

3.9 Preparation of Masks

Various shapes of thickness were deposited on the surface of $CuO:Cu_2O$ thin films using thermal evaporation equipment through a mask giving active area of (0.2×0.2) cm^2.

3.10 Thickness Measurement

Thickness is one of the most important thin film parameters. There are several methods used for measuring the thickness of thin film. In this work, the thickness of the films were measured by the weight method.

3.10.1 Weighting Method

Thickness of the thin films has been calculated according to the following equation [85]:

$$t = \frac{m}{2\pi\rho R^2} \tag{3.1}$$

Where (t) is thickness of the thin films (nm), (m) is a mass of the material in (g), (ρ) is the density of material (g/cm^3) and (R) is the distance between the substrate and the boat (cm). This method gives an approximate thickness because some of the material lost or fleeing on the sides of the heater.

3.11 Structural and Morphological Measurements

These measurements include the following:

3.11.1 Atomic Force Microscopy (AFM)

The atomic force microscopy (AFM) which exist in university of Babylon / Department of Physics College of Education for pure Sciences, the (AFM) enables us to have a look at the surfaces on a molecular level.

Instead of only pictures real topography data are collected. AFM determines the size and other characteristics of the synthesized nanoparticles, an atomic force microscopy (AFM) were used.

3.11.2 X-ray Diffraction (XRD)

The main purpose of these measurements is to investigate the type of the structure of the prepared thin films. This experimental technique has long been used to determine the overall structure of bulk solids, including lattice constants, identification of unknown materials.

Orientation of single crystals, orientation of polycrystals, defects, stresses, etc. X-ray diffraction using (SHIMADZU X-ray diffracts meter system (XRD-6000)), which records the intensity as a function of Bragg's angle. The conditions of the system were; Source CuK_{α} with radiation of wavelength λ = 1.5406 $\mathring{A}$, Target: Cu, Current = $30\ mA$. Voltage=40 kV. Scanning speed = 0.25 deg/min, the examinations were made at XRD Laboratory - University of Kufa.

Figure(3.4): X - Ray Diffraction Device.

3.11.3 Scanning Electron Microscopy (SEM)

The scanning electron microscopy (SEM) which typically has an energy ranging from (0.4-5) KeV, is focused by one or two condenser lenses to a spot about (0.4-5) nm in diameter. The beam passes through pairs of scanning coils or pairs of deflector plates in the electron column, typically. In the final lens.

3.12 Optical Measurements

The optical measurements of $CuO:Cu_2O$ thin films are obtained by using spectrophotometer (Shimadzu UV- 1650 PC) made by Phillips, (Japanese company). The optical properties were calculated from those optical measurements.

3.13 Electrical Measurements

The electrical measurements are achieved on prepared thin films including Hall effect and I-V characteristics.

3.13.1 Hall Effect Measurements

Carrier concentration, carrier type and mobility have been determined from Hall measurements for CuO thin films having different CuO - contents and deposited on glass substrates.

3.13. 2 Current-Voltage Measurements for The Hetero-junction Under Illumination

The study of electrical and photovoltaic properties of solar cells consists of the following equipment's:

1- D.C. Power supplied of type (6291A).

2- Micrometer type (Keithley 177 Micrometer Dmm).

3- Voltmeter made in china type (DT890G).

4- Halogen light with power (120W) gives radiation density from shunt voltage.

4.1 Introduction

This chapter presents the results and discussion of the structural, morphological, and optical properties of CuO nano-film with thickness (75) nm that prepared onto glass substrate by thermal evaporation technique at room temperature(R.T). In addition, study the structural, optical, and electrical properties of prepared nano-film. Finally Hall effect and electrical measurements of heterojunctions including current-voltage in two case of darkness and lighting illuminations were studied.

4.2 Measurements and discussions:

In this paragraph several measurements are included:

4.2.1 Atomic Force Microscopy(AFM)

The AFM image of pure and Cu_2O-doped CuO with different doping of CuO (0.002,0.004 and 0.006) wt.%. Thin films were prepared by thermal evaporation technique under pressure of (1×10^{-7}) mbar with rate of deposition (0.5) $nm.s^{1}$, which annealed temperature (200)°C for one and two hours and thickness 75 nm .

From these Figures ((4.1)-(4.3)) the 2D and 3D AFM surface images, distribution granular, and grain histogram thin films of CuO thin films annealed for one and two hours at temperature $(200)^{\circ}$C. It can be observe that the roughness decrease from (0.467 to 0.337) nm and root mean square (RMS) decrease from (0.581 to 0.426) nm and the average grain diameter was evaluated from the plane view image that decrease from (149.1 to 143.2) nm.

The ten point height represent the surface morphology on the thin film ,which refer to the height of ten points measured by AFM device. Which is in accordance with the findings of researches of [85, 86] . They decrease from (4.15 to 2.19) nm as in part (a)and (b) from the Figures((4.1)-(4.3)) where (a) represents a picture in three dimensions and the highest level was a peak with a rate of (2.29-2.23) nm for the surfaces of these membranes, (b) represents a picture in two dimensions, these results show a uniform granular surface morphology as listed in Table (4.1). The results are in accordance with the findings of researches [61,62]. The average grain diameter was evaluated from the plane view images.

Part (c) from the Figures((4.1)-(4.3)) represents the granular distribution on the surface of these membranes. Which related to the 2D distance of grain molecule that appear in the measurements of AFM device. Part (d) from the Figures ((4.1)-(4.3)) refers to the height histogram which describes the relationship between the height of the grains and its volumes.

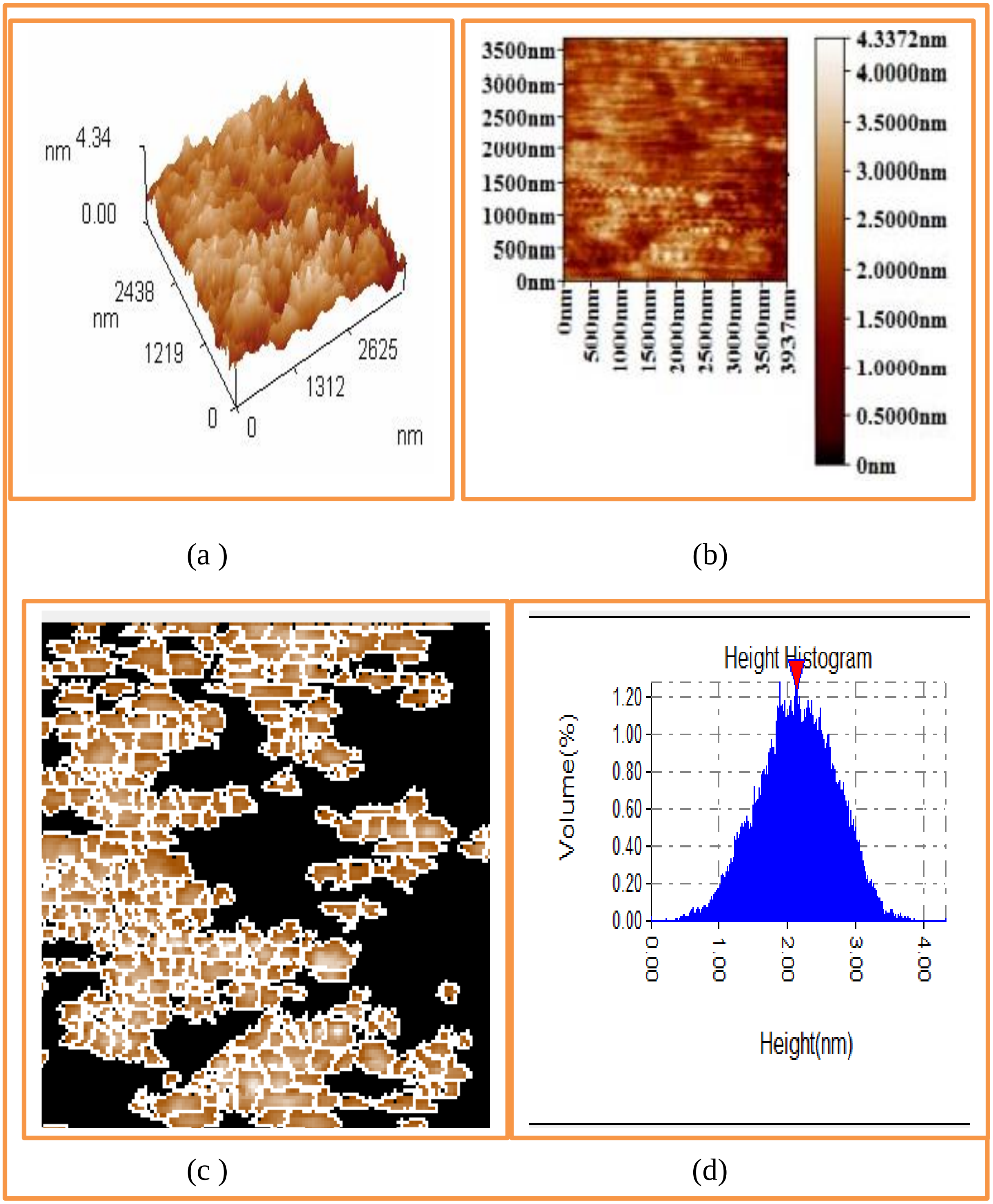

(a) (b)

(c) (d)

Figure(4.1):The AFM Images of Pure CuO Thin Film at Various Annealing Times, a-3-D ,b-2-D, c-Total No. of Particles, and d-Height Histogram.

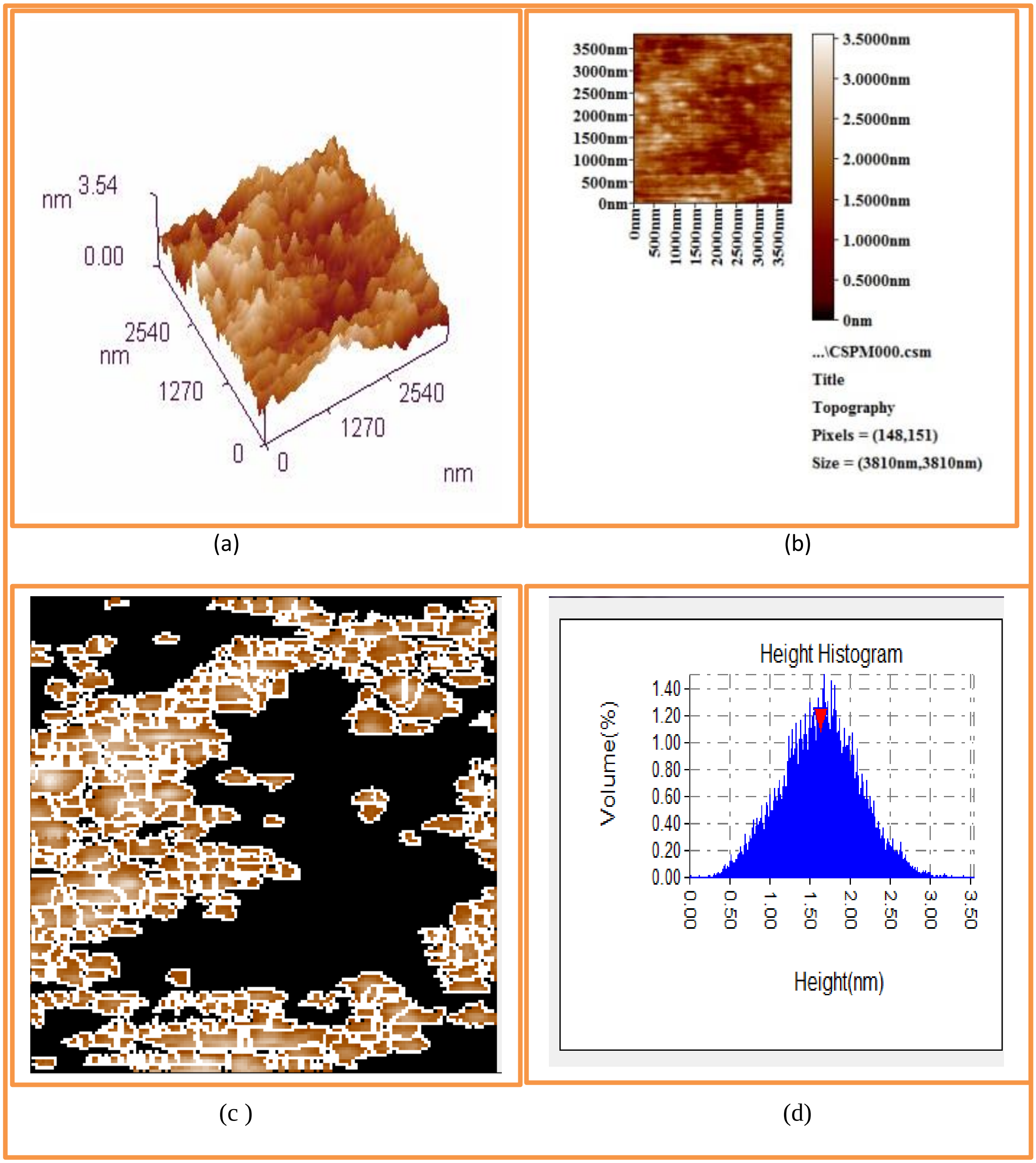

(a) (b)

(c) (d)

Figure(4. 2):The AFM Images of Pure CuO Thin Film at Various Annealing Times a-3-D ,b-2-D, c-Total No. of Particles, and d-Height Histogram.

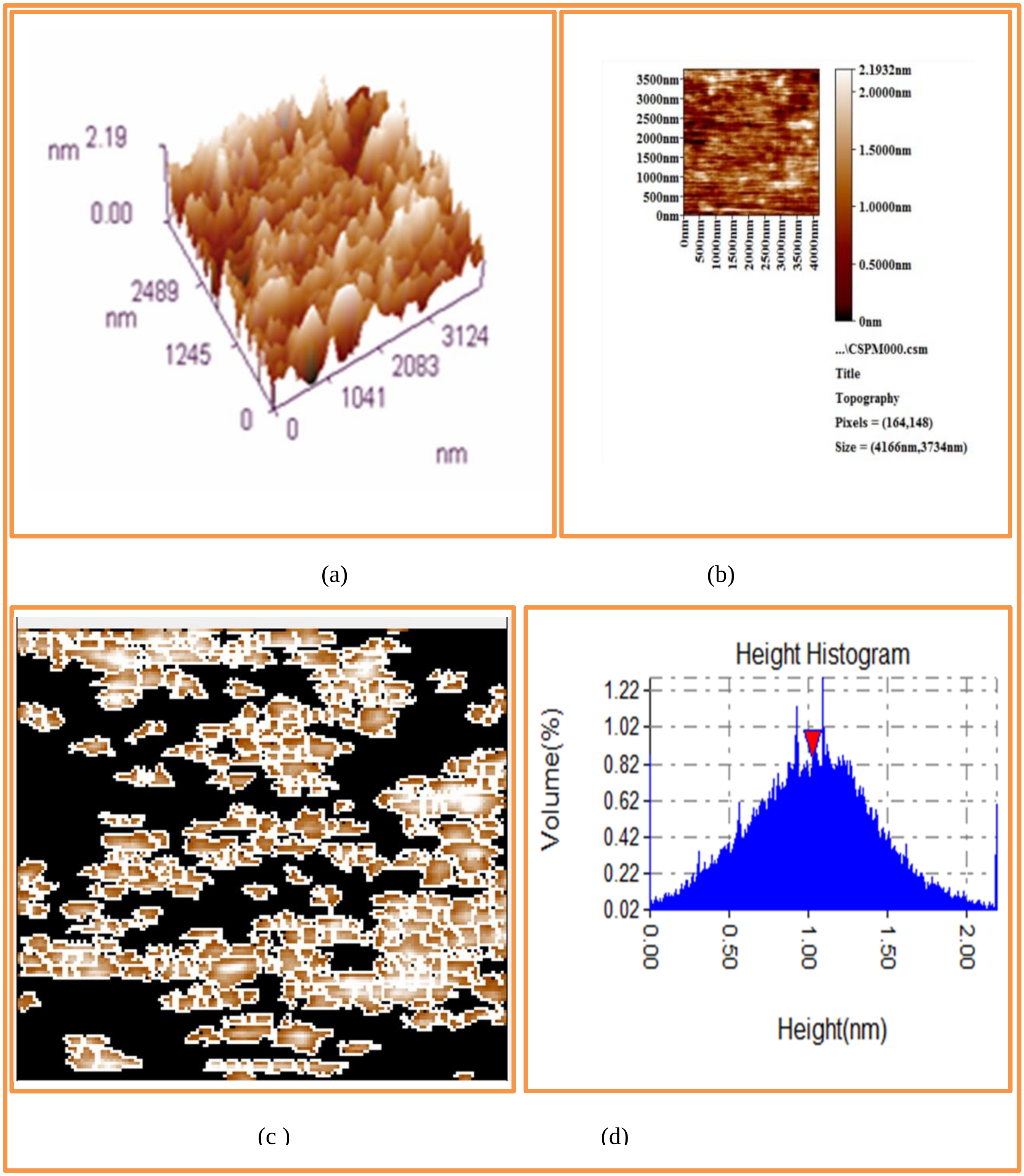

(a) (b)

(c) (d)

Figure(4. 3) :The AFM Images of Pure CuO Thin Film at Various Annealing Times, a-3-D ,b-2-D, c-Total No. of Particles, and d-Grain Histogram.

Table (4.1) Morphological characteristics of CuO thin films at thickness(75) nm at various annealing times.

Thin films type	Roughness average Sa (nm)	Root mean square Sq (nm)	Ten point height Sz (nm)	Average diameter(nm)
CuO at (R.T)	0.467	0.581	4.34	149.1
CuO annealed for 1 hour	0.393	0.493	3.54	142.6
CuO annealed for 2 hours	0.337	0.426	2.19	143.2

After annealing for two hours with various amount of Cu_2O –doped CuO, we found that all morphological film morphology and surface roughness were affected by adding Cu_2O also, (RMS) root mean square and roughness average are increased with nanoparticle additive. As shown in Figures from((4.4) -(4.6)) respectively.

As seen in Figures (4.3), ((4.4)-(4.6)), it can be observed that the roughness decreased from ((3.58)-((0.467)) nm, also root mean square (RMS) decreased from (4.23) nm for pure CuO to (1.48) nm for CuO:0.002% Cu_2O thin film and also the roughness decreased to ((1.82)-((0.581)) nm. The ten point height decreased from ((9.45) to (4.15)) nm. The average diameter decreased from ((153.2) to (149.1)) nm. All results are listed in Table (4.2), the 2D and 3D AFM surface images, distribution granular, and grain histogram thin films, the images show a uniform granular surface morphology as in Figures ((4.4)- (4.6)).

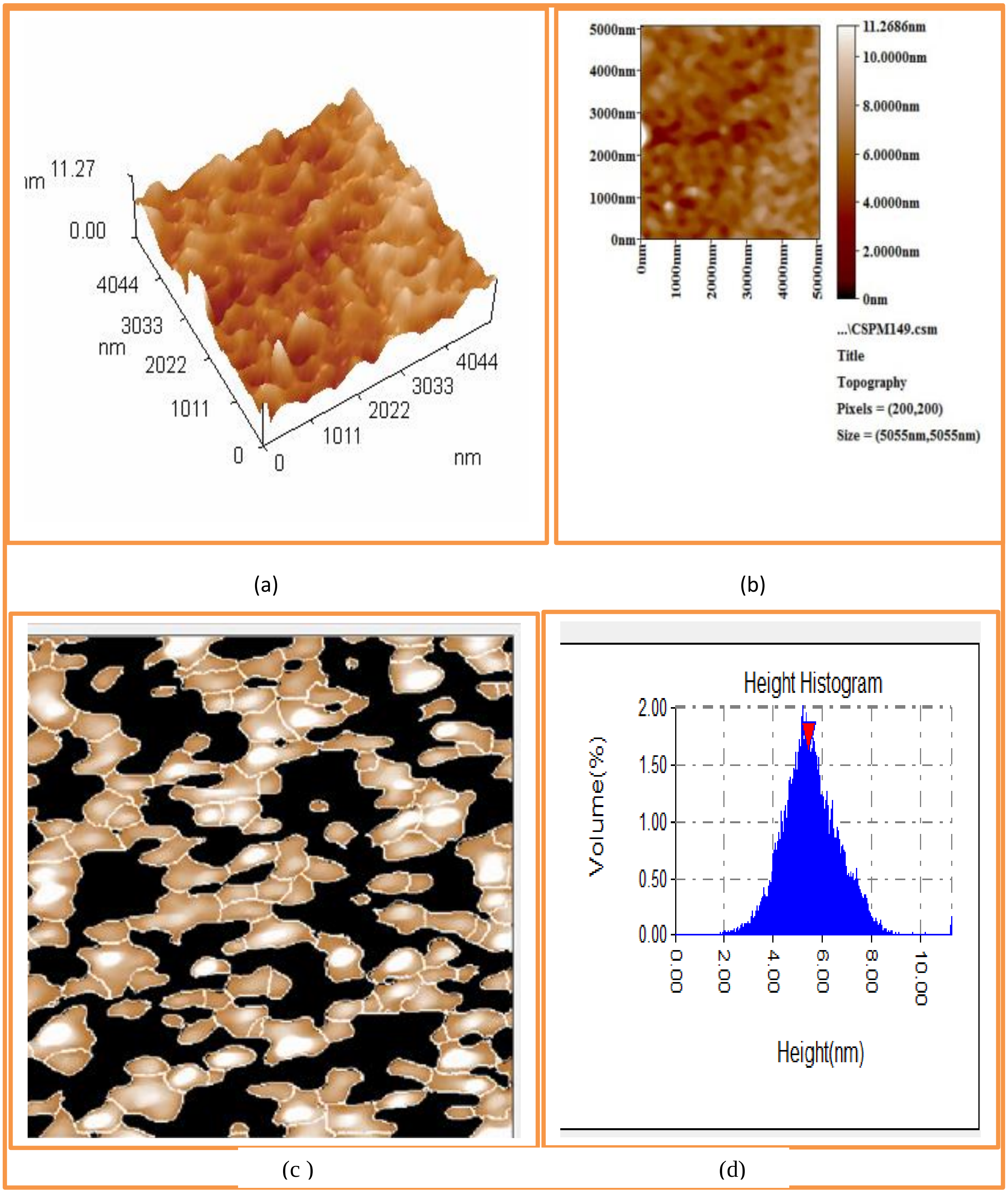

(a) (b)

(c) (d)

Figure(4.4): The AFM Images of CuO :0.002% Cu_2O Thin Film ,a-3-D ,b-2-D, c-Total No. of Particles, and d-Grain Histogram.

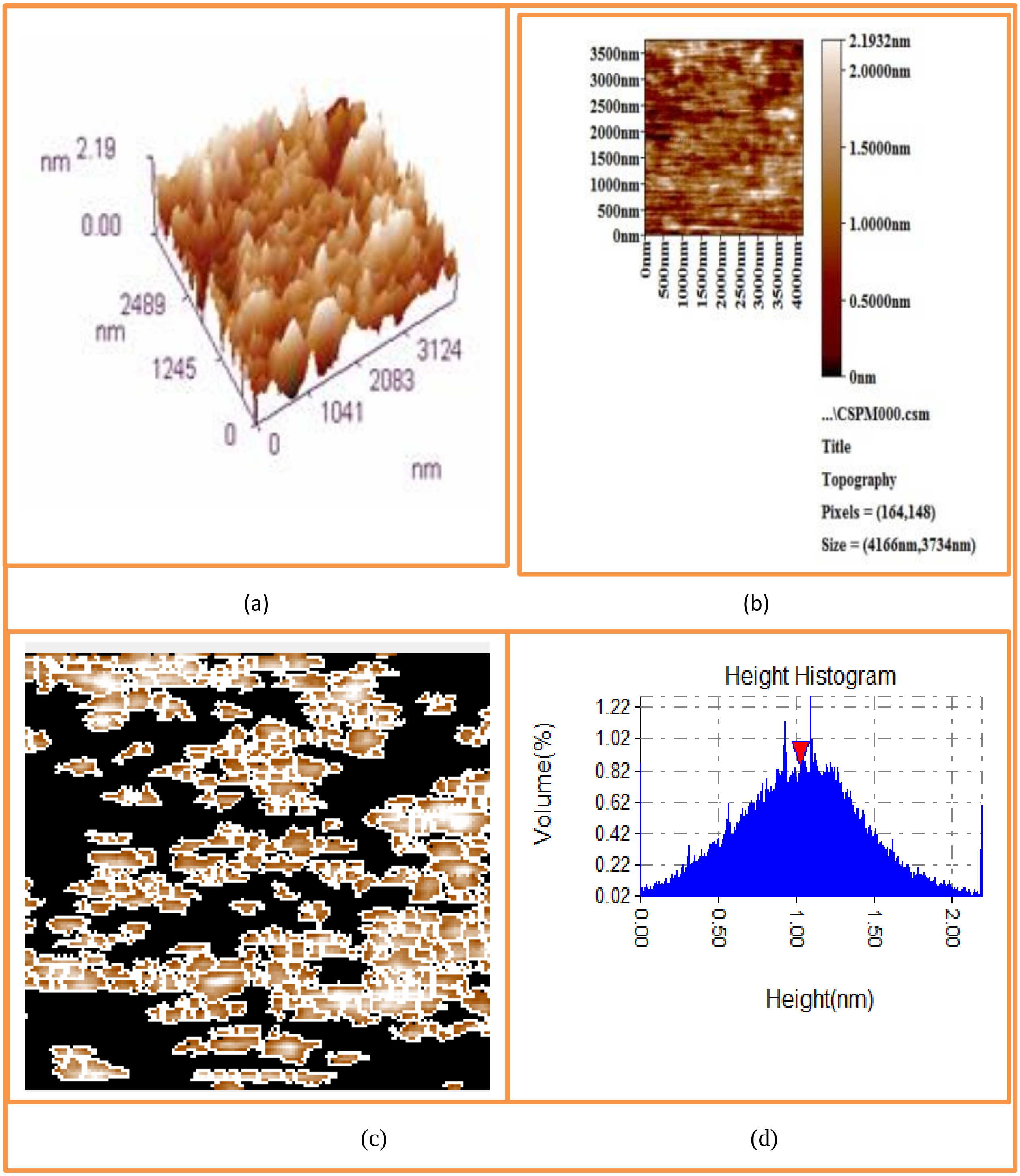

(a) (b)

(c) (d)

Figure(4.5) :The AFM Images of CuO:0.004%Cu_2O Thin Film a-3-D ,b-2-D, c-Total No. of Particles, and d-Grain Histogram.

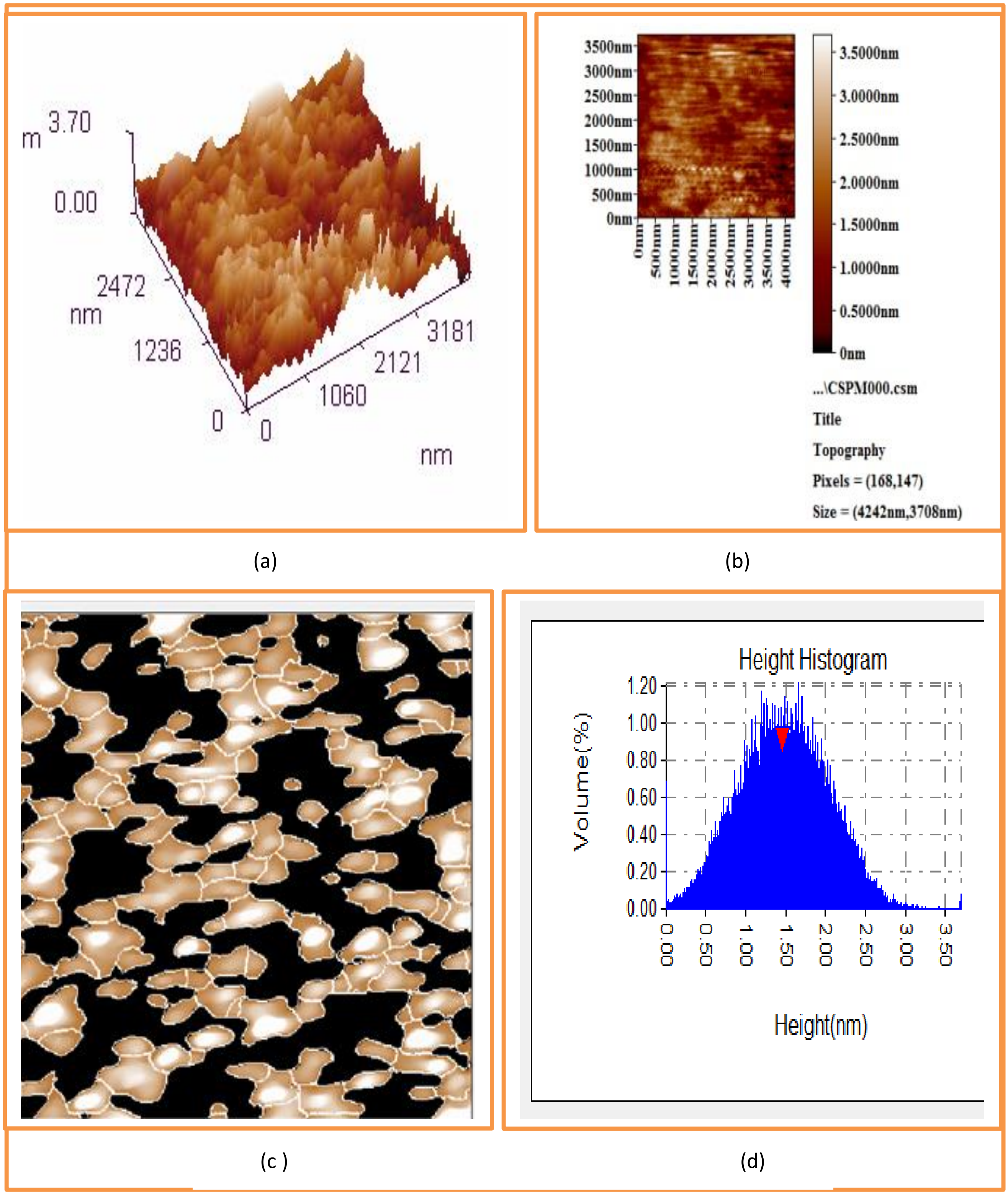

(a) (b)

(c) (d)

Figure(4.6) :The AFM Images of CuO :0.006% Cu_2O Thin Film a-3-D ,b-2-D, c-Total No. of Particles, and d-Grain Histogram.

Table (4.2): Morphological characteristics of Cu_2O:CuO thin film deposited at different doping weight ratios of Cu_2O.

Films Type	Roughness Average Sa (nm)	Root mean square Sq(nm)	Ten point height Sz (nm)	Average diameter(nm)
Pure CuO	0.5	0.581	4.34	149
CuO:0.002wt.%Cu_2O	0.393	0.493	3.41	142.6
CuO:0.004wt.%Cu_2O	0.337	0.426	2.09	143.2
CuO:0.006wt.%Cu_2O	0.465	0.577	3.5	149.4

4.2.2 X-Ray Diffraction of CuO and CuO: Cu_2O Thin Films

The technique of X-ray diffraction (XRD) was used to know the nature of the crystal structure, the main crystalline stages, and the orientation of the prepared thin films under certain conditions, as well as to identify some structural variables such as the crystal size. The X-ray Diffraction (XRD) spectra of pure and Cu_2O-doped CuO thin films with different amounts of Cu_2O doping, prepared by thermal evaporation technique at room temperature under pressure up to (1×10^{-7}) mbar, rate of deposition (0.33) $nm.s^{-1}$, which annealed at a temperature (200)°C for two hours and thickness of (75) nm. Peaks of XRD were recorded (2θ) between (10°-80°). In the XRD pattern as shown in the Figures ((4.7)-(4.10)), the main peak was observed at ($2\theta = 32.321^\circ$), to the reflection plane (110) for pure CuO at the greatest intensity(100) with crystallite size (18) nm. The preferred orientation of the particle is due to the growth process is controlled by nucleation [88].

Figure (4.7) illustrate that the predominant peak was observed at 2θ =44.667º (200) which correspond to CuO. The other peaks for the CuO film were observed at 2θ =28.275º(112), 34.410º (111), 51.057º (020), 54.813º (220), 78.229º (311), all the peaks indicated the CuO [57,87,88].

Figure (4.8) represents the 0.002wt.% Cu_2O-doped CuO film. The small peaks intensity that appeared in pure CuO films are disappear in the Cu_2O-doped CuO films implies that the particles are CuO with(0.002) wt.% Cu_2O, it observe that the old peaks disappeared and show a new and special peaks correspond to Cu_2O in addition to the peaks for CuO, a predominant peak was observed at (2θ =44.667°) (200), a main peak was observed at 2θ = 32.162° when reflection plane (110) with crystallite size (13) which will decrease in comparison with the crystallite size in Figure (4.7) for the same 2θ, it can note that the broadening in full width at half maximum (FWHM) indicating the small particle size. When the annealed temperature is (200) °C, the number of particles increases, which puts it under pressure on these particles, the other peaks for the CuO film were observed at 2θ =29.563° (112), 34.40° (111), 64.87° (220), 78.14° (311). Also appears other peaks for the Cu_2O film were observed at 2θ =41.033°, 2θ =44.667° which is in agreement with [56].

The main peak was observed at 2θ = 32.162º when reflection plane (110) with crystallite size (13) nm, which will decrease in comparison with the crystallite size in pure CuO film. Because of the Cu_2O doping, it can note that the broadening in full width at half maximum (FWHM) indicates the small particle size. The other peaks for the CuO film that observed at 2θ = 29.563º (112), 34.40º (111), 64.87º (220), 78.14º (311), also appear other peaks for the Cu_2O film were observed at 2θ = 41.033º, which is in agreement with [58].

From Figure (4.9) and through the study of the surface composition of the films, it was observed that the particles with doping 0.004wt.%Cu_2O, show a strong peak was observed at 2θ=(22.178° and 27.821°) at reflection plane (101), (112). The crystallite size is (5) nm for (2θ=22.178°) at greatest intensity(100) and the crystallite size is (4) nm for (2θ=27.82°) with intensity (94.9), the crystallite size was calculated by using the Scherer's formula according to the equation (2.2). The predominant peak in this Figure is (44.667)° (200) noticed a decrease in this peak by combining with Figures ((4.7)-(4.8)), also there is a decrease in the main peak (32.821°) and became(10) and more sharpness as compression with figures below.

The appearance of the peak (110) at the angle (2θ = 32.821°) which returns to the crystal plane which is ascribed to the improvement of the crystallinity in the films. The surface was polycrystallite and there is no direction of the films, no peaks appear to refer to so fine crystal structure [56]. The diffraction peaks located at (2θ=34.4° and 51.07°) corresponding to (111), (020) of Cu_2O respectively. Also the diffraction peaks that belong to CuO a (2θ=64.813°) at reflection plane(220), by increasing the doping of Cu_2O the peaks become more randomly as the crystallite size decreases when (FWHM) indicating the small particle size .

Figure (4.10) shows a rise in the peaks and becomes sharp for the crystal planes with doping 0.006 wt.%Cu_2O, a predominant peak was observed at(2θ = 44.588°) at reflection plane (200). The main peaks in this Figure were at (2θ = 24.79° and 29.38°) with crystallite size (4 and 6) nm and intensity (100,56.2) respectively. Because the Cu_2O –doping, a decrease in crystallite size for the main peak at (2θ =31.221°) with reflection plane (110) and became(5) that is why the peaks become more randomly as the crystallite size decreases and more sharpness as compression with Figures ((4.7)-(4.9)).

The other peaks for the CuO film were observed at (2θ= 34.180°) (111) , (64.8°) (220) respectively. Because the Cu_2O –doping, the results are represented in figures (4.9) and (4.10). The films were polycrystalline with the orthorhombic structure [41,83]. The results are the same as represented in the results of AFM and SEM measurements. We can notice that the crystallite size decreases in both of them and they are listed in Figures mentioned in AFM results.

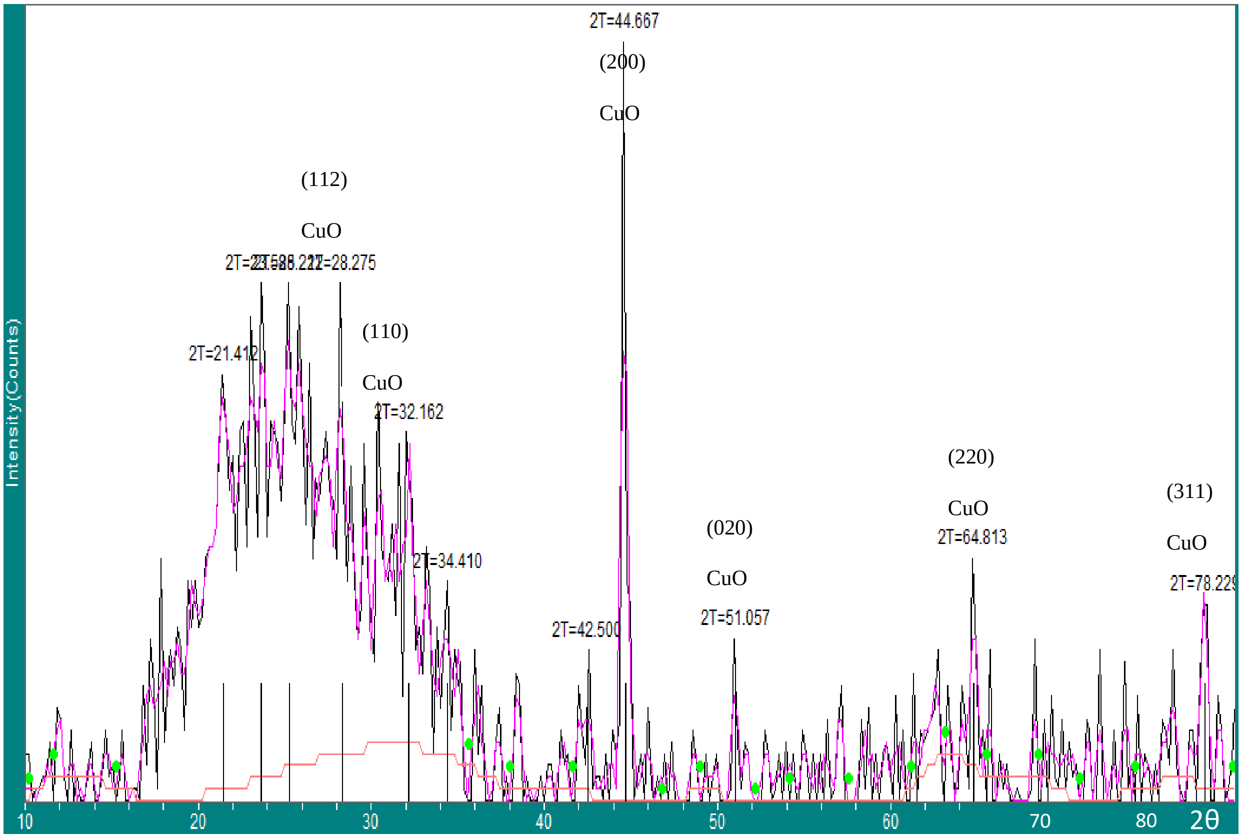

Figure(4.7): The (XRD) Diffraction Pattern of Pure CuO Thin Films.

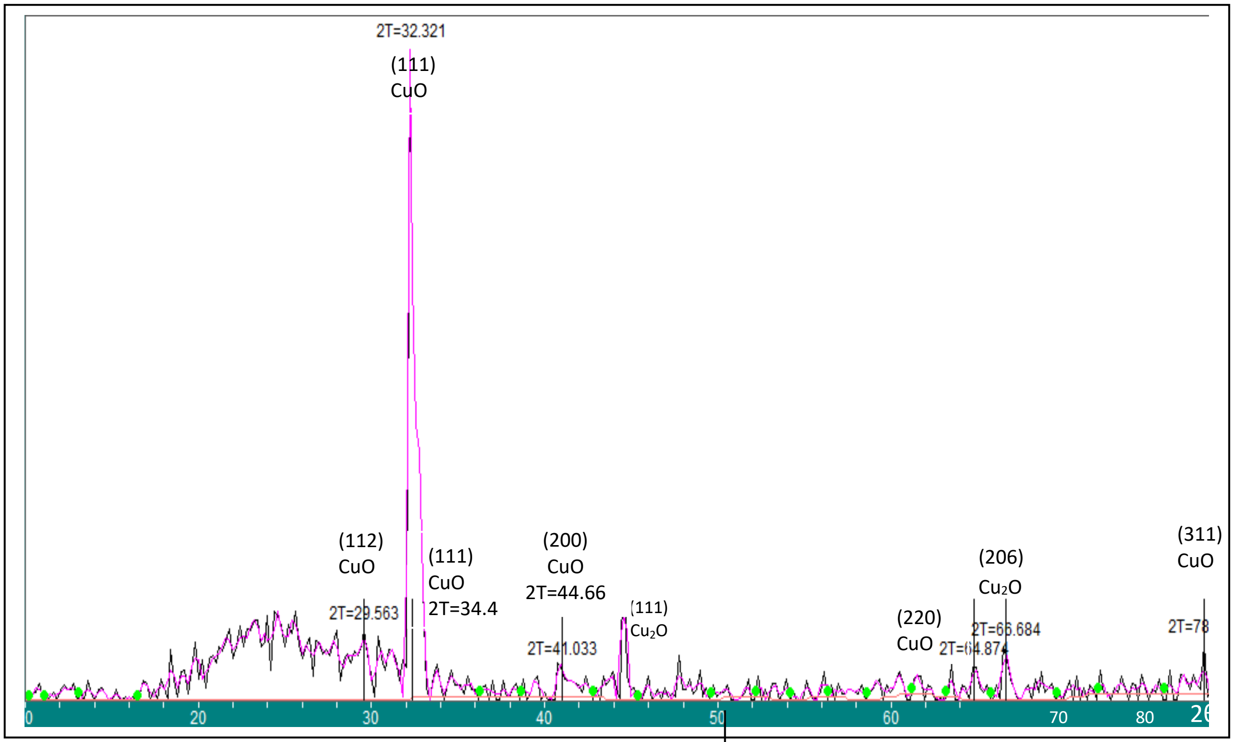

Figure(4.8): The (XRD) Diffraction Pattern of CuO:0.002 wt % Cu_2O Thin Films .

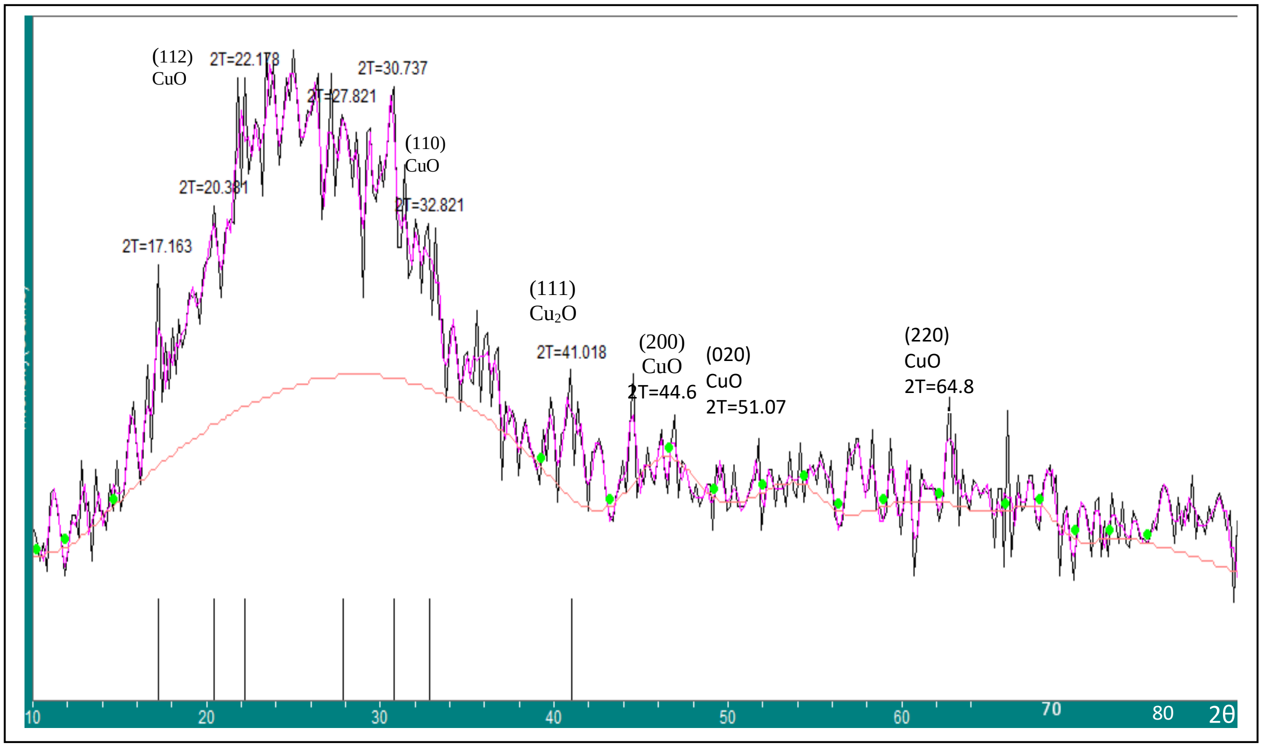

Figure(4.9): The (XRD) Diffraction Pattern of CuO:0.004 wt % Cu_2O Thin Films.

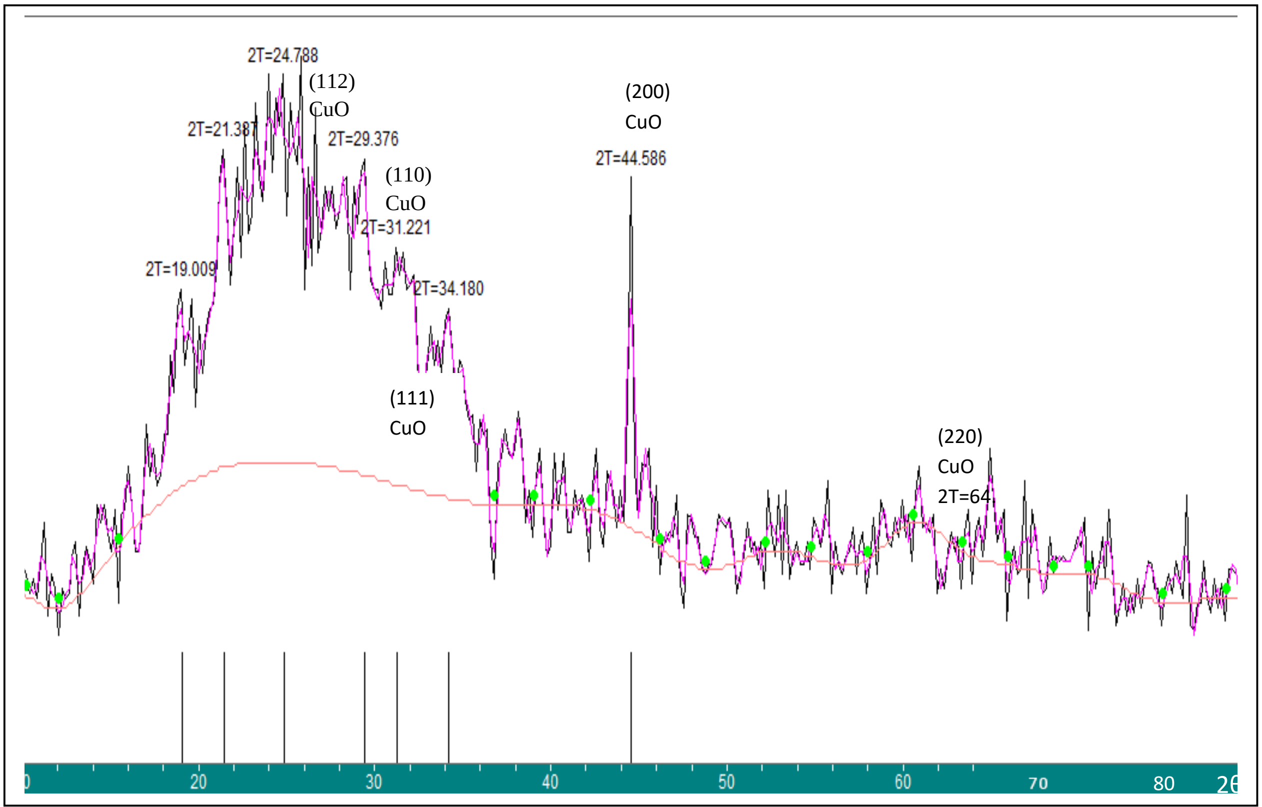

Figure(4.10):The XRD Pattern of CuO:0.006 wt %Cu_2O Thin Films.

The average crystalline size, FWHN, and peak position of the prepared thin film grains on the glass slide at different concentrations are shown in Table (4.3).

Table (4.3): The average crystalline size, FWHM, and peak position at different concentrations of CuO:Cu_2O thin films.

Cu_2O-doped CuO(wt%)	2θ (degree)	hkl	d(nm)	BG	Height	Area	I%	FWHM	XS
Pure CuO	32.321	(111)	0.27675	0	287	793	100	0.47	18
CuO:0.002Cu_2O	25.212	(002)	0.35295	3	42	357	100	1.445	8.6
	32.162	(111)	0.27808	5	27	101	28.3	0.636	
CuO:0.004Cu_2O	22.178	(101)	0.40049	64	72	631	100	1.49	11.5
	27.821	(112)	0.3204	71	57	599	94.9	1.786	
	32.821	(111)	0.27265	68	36	173	27.4	0.817	
CuO:0.006Cu_2O	24.788	(002)	0.35888	64	83	889	100	1.821	10
	29.376	(112)	0.30379	61	68	500	56.2	1.25	
	31.221	(111)	0.28625	59	51	481	54.1	1.603	

4.2.3 Scanning Electron Microscopy (SEM):

The surface topography was studied using a scanning electron microscopy ,which determined shape and size of the prepared samples from pure and Cu_2O-doped CuO with different doping of Cu_2O (0.002,0.004 and 0.006)wt.% thin films at high-magnification scan range. The position of pure and Cu_2O –doped CuO on glass substrate for all samples is shown in Figures ((4.11)-(4.14)) .

In Figure (4.11) show that the pure CuO thin film exhibits a smooth surface consisting of small spherical grain size particles. Size measurement showed that these particles size from (30.31 to 35.05) nm .

It can be noticed that the CuO NPs surface layer appeared to cover all the regions of the substrate very well without the presence of voids, pinholes or cracks. Figure(4.11) indicated the regular distribution free of holes and defects of nanopareticles during the deposition procedure. This figure showed the magnified view and the spherical morphology is evident, which revealed the interesting distribution of shaped nanoparticles. A few of the particles appeared larger, while most of them were the same size. The grain take form of spheres, which increased the size of nanoparticles others are irregular in shape. With some holes, although grouped together but not contiguous due to a number of complications.

The inset in Figure (4.12) of CuO:0.002 Cu_2O thin films with magnification (100) kx. Size measurement showed that these particles size from (15.42-24.92) nm, is totally coated the substrate ,and the surface morphology of the CuO films seems to be influenced by the Cu_2O, also a small spherical granules distributed over the substrate surface, and the size of these grains increased with increasing doping ratio [89].

The inset in Figures (4.13-4.14) show CuO:Cu_2O tin films are homogeneous, smooth, totally coated the substrate, and free from defects such as pinholes and cracks. The beans are distributed in the same size, dense, well defined. Size measurement showed the particles size from (23.05 to 30) nm. It was observed that the small spherical granules distributed over the substrate surface[90]. Figure (4.14) showed particles size from (34.56-35.05) nm. The results refer that by doping additive amounts of Cu_2O will produce high potential on the original grain particles which don't let them grow up.

A very fine surface make these agglomerations seem as individual grains. The tilted image exposes grain heights of a few tens of nanometers. From the results of the SEM measurements, the decrease in crystallite size as matched with the XRD results, which led to the formation of grain particles that are evident as in[91-92].

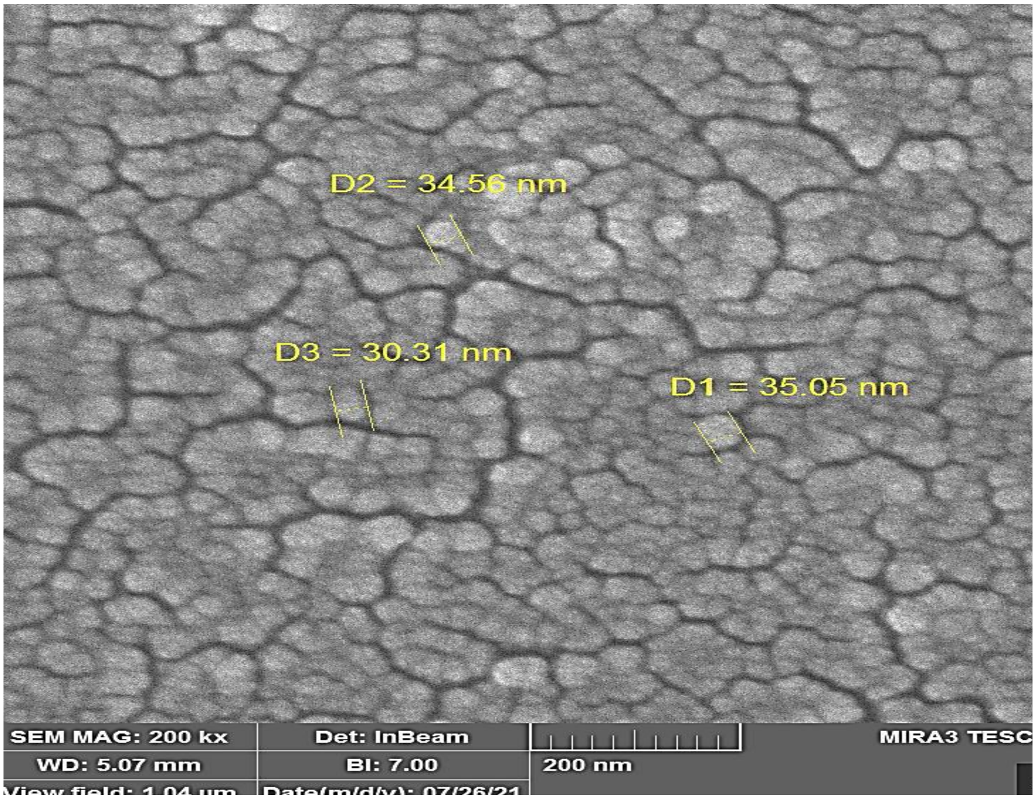

Figure(4.11): SEM Image of Pure CuO NPS with Magnification 200 kx .

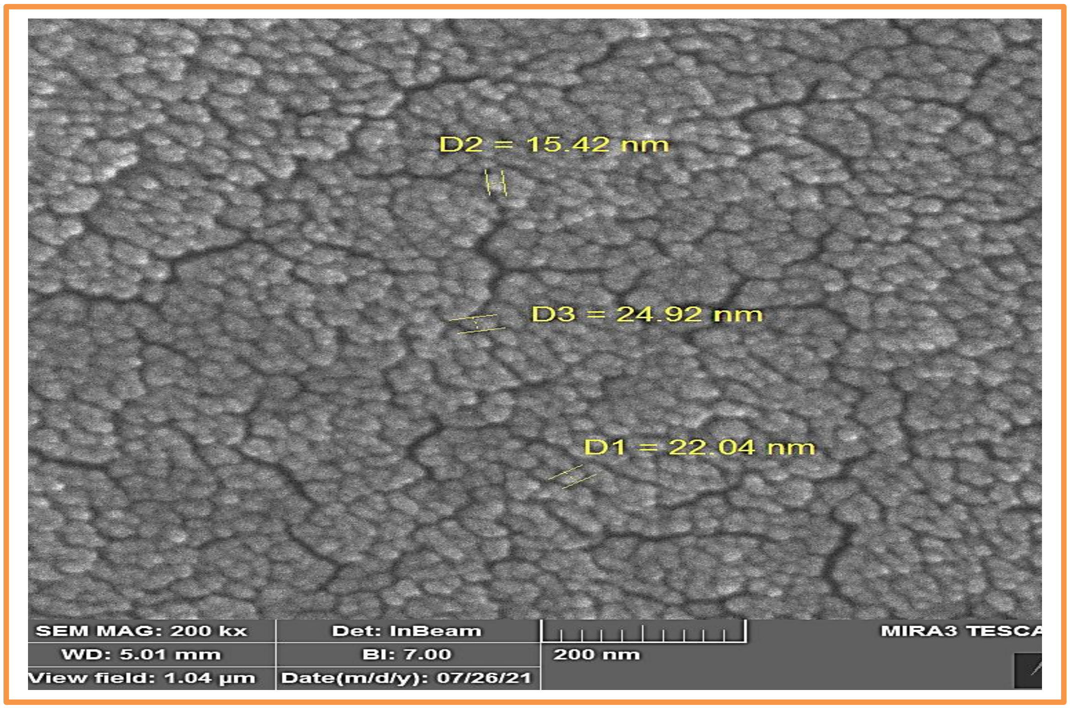

Figure(4.12): **SEM Images of the CuO:0.002 wt.%Cu_2O Thin Films with Magnification 200 kx.**

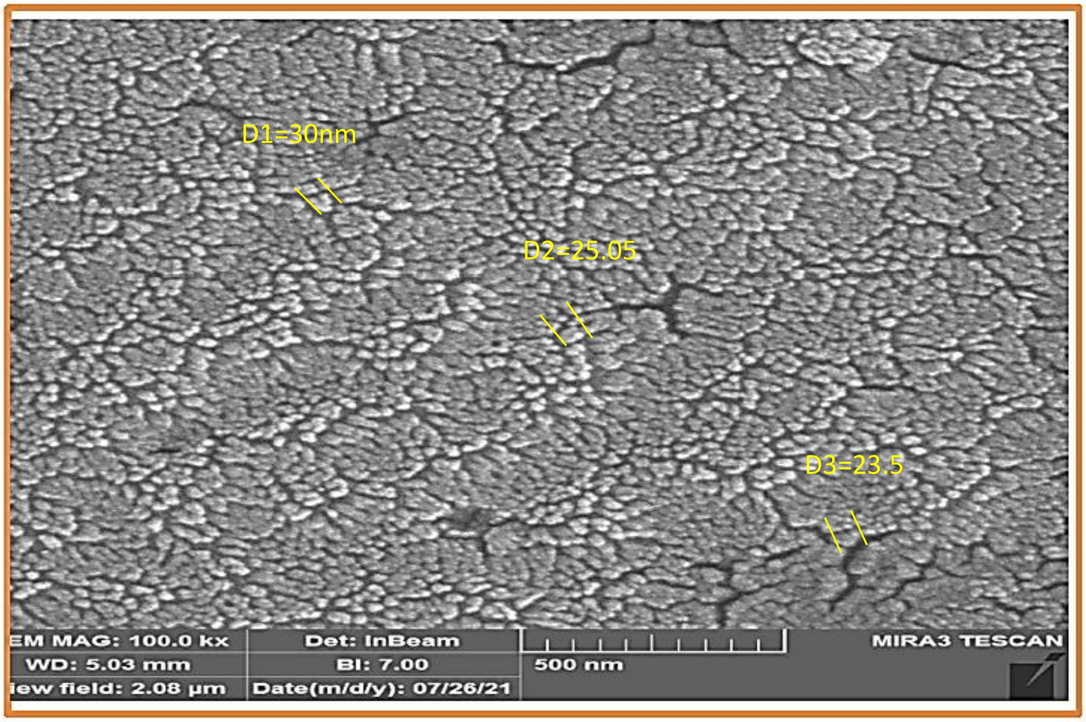

Figure(4.13): **SEM Images of the CuO:0.004 wt.%Cu_2O Thin Films with Magnification 200 kx.**

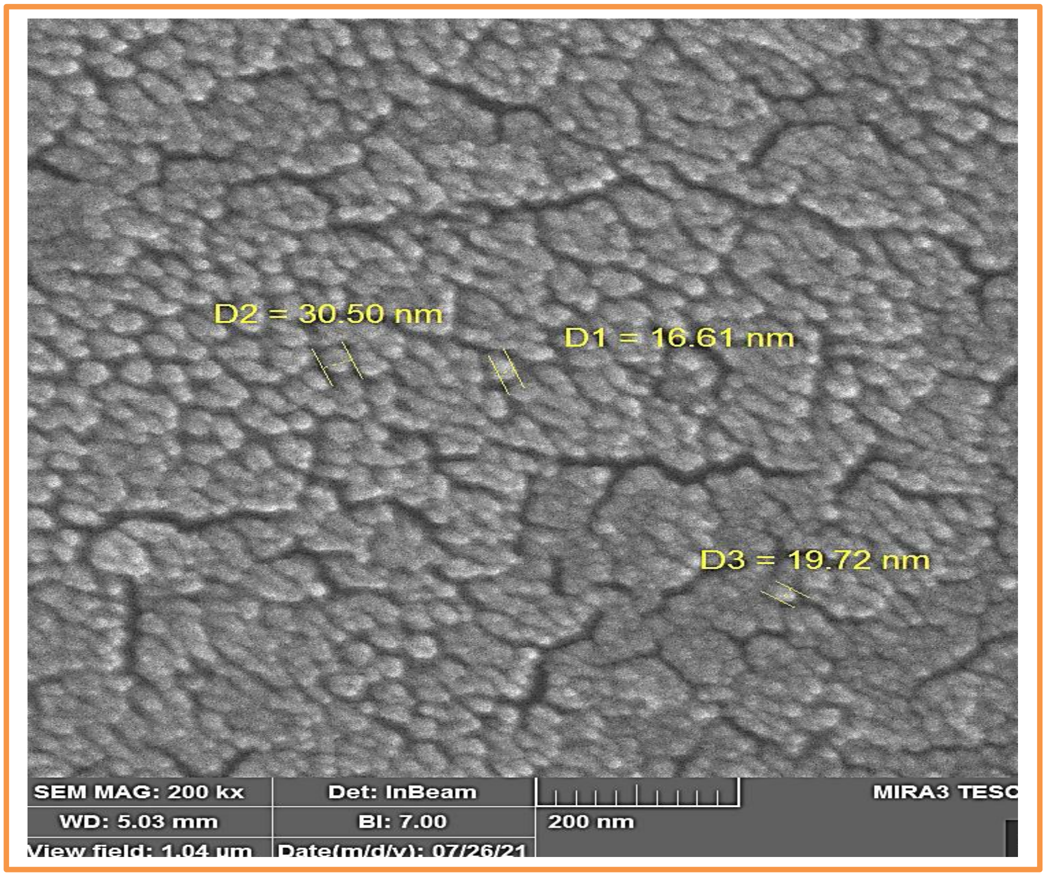

Figure(4.14): **SEM Images of the CuO:0.006 wt.%Cu_2O Thin Films Magnification 200 kx.**

4.2.4 Optical Properties of Pure CuO Thin Films:

The optical properties of the pure CuO and Cu_2O prepared by thermal evaporation technique under pressure of (1×10^{-7}) mbar with rate of deposition (0.5) nm.s^{-1}, which annealed temperature (200)$^{\circ}$C for one and two hours with thickness (75) nm. The study of the optical properties is useful in the task of determining the nature of the practical application that can be used to record thin film material.

The optical measurements were determined by using UV-Spectrophotometer, in spectrum range of (300–1100) nm which include spectral transmittance (T) and Absorbance (A). They were studied by recording the absorbance spectra at the range of wavelength between (300-1100) nm. It determined the optical properties such as transmittance, absorption coefficient (α), refractive index (n), optical energy gap (E_g), dielectric constant (real (ε_r) and imaginary(ε_i) using computer program, for a good understanding to the band structure and energy band gap (E_g) for an amorphous materials, there is an a productive tools by the analysis of optical transmission spectra and the absorbance. To study the effect of thermal annealing on the optical transmission of copper oxide (CuO) thin films, the effect of doping with various weight ratio of Cu_2O is also studied.

4.2.4.1.1 The Absorption spectra of pure CuO (A):

The optical absorbance as a function of wavelength in the range (280-1080) nm, the CuO thin film have deposited on glass substrate annealed for one and two hours at temperature (200)°C as shown in Figure (4.15), it can be observed that the absorbance spectra of CuO thin films increased with the increasing of annealing temperature. This behavior can be attributed to the increasing in the grain size with temperature, which is in accordance with the findings of researchers [67,93]. This physically means that incident photon is not able to excite the electron and transfer it from valence band to the conduction band because the energy of incident photon is less than the value of the energy gap value of the semiconductor which leads to the absorbance increased with increasing the temperature.

It is also noticeable that the shifts of absorbance spectrum to higher wavelengths (low energies) with the increase of annealing temperature for all thin films may be attributed to the crystallization of thin films structure by decreases the grain size [94], which is in agreement with the result of AFM. Absorption spectra optical depends on the chemical composition crystal structure, energy of the incident photon, film thickness, and film surface morphology.

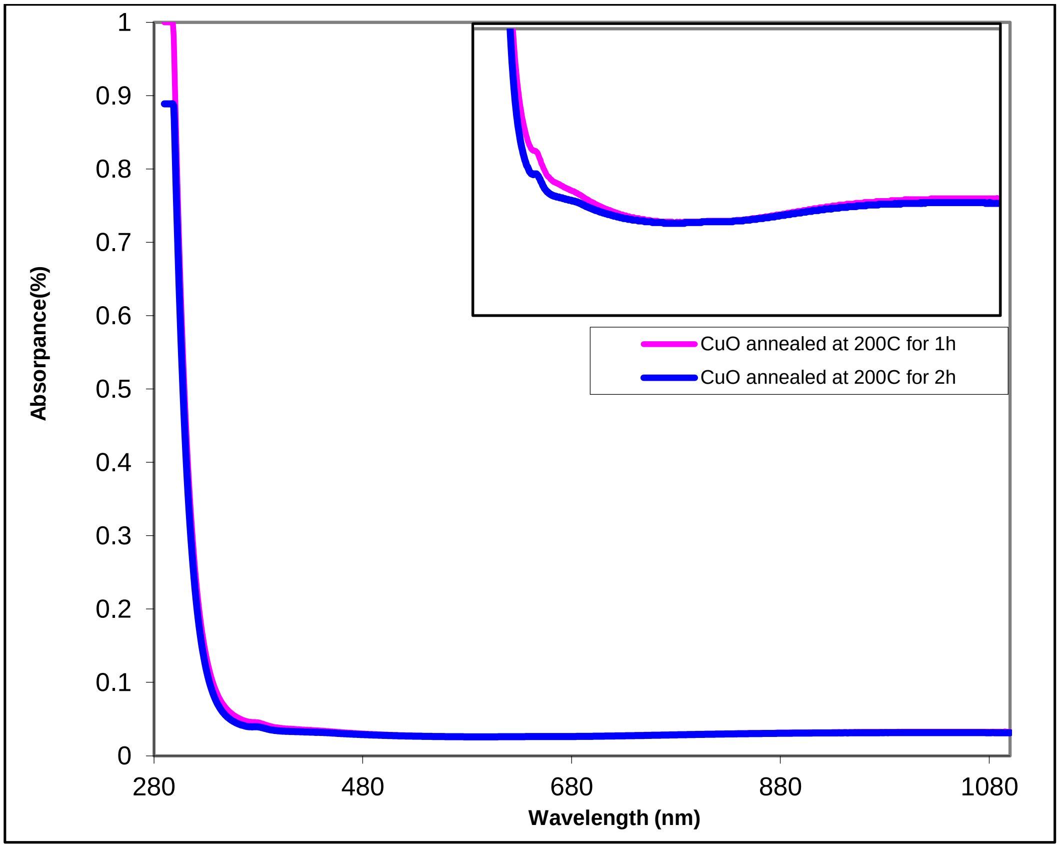

Figure(4.15): The Absorbance Spectra As a Function of Wavelength of CuO Thin Films at Various Annealing Time.

4.2.4.1.2 The Transmittance

The transmittance spectra of CuO film were decreased with increasing of the annealing temperature as shown in Figure (4.16). This figure present the graphic relationship between transmittance and wavelength. It can be noticed that the transmittance slightly increases with increasing annealing temperature. Transmittance demonstrated behavior opposite of absorbance as shown in figures below. The transmittance of prepared films decreases with increasing of temperature that could due to the increasing crystallinity of CuO film due to formation of a new localized levels under the conduction. The decreased in transmittance due to an increase in the number of atoms, which increasing the number of photon colliding with incident atoms.

The transmittance spectra was calculated by using equation(2.12) resulting in a decrease in the transmittance. As well the drop in transmittance due to the shift of the absorption edge for thin film become less sharp, which is attributable to the fact that larger crystallite volume are deposited because since more atoms are found in the material, more states would be required for photons to be absorbed, which is in accordance with the findings of researchers [55,64].

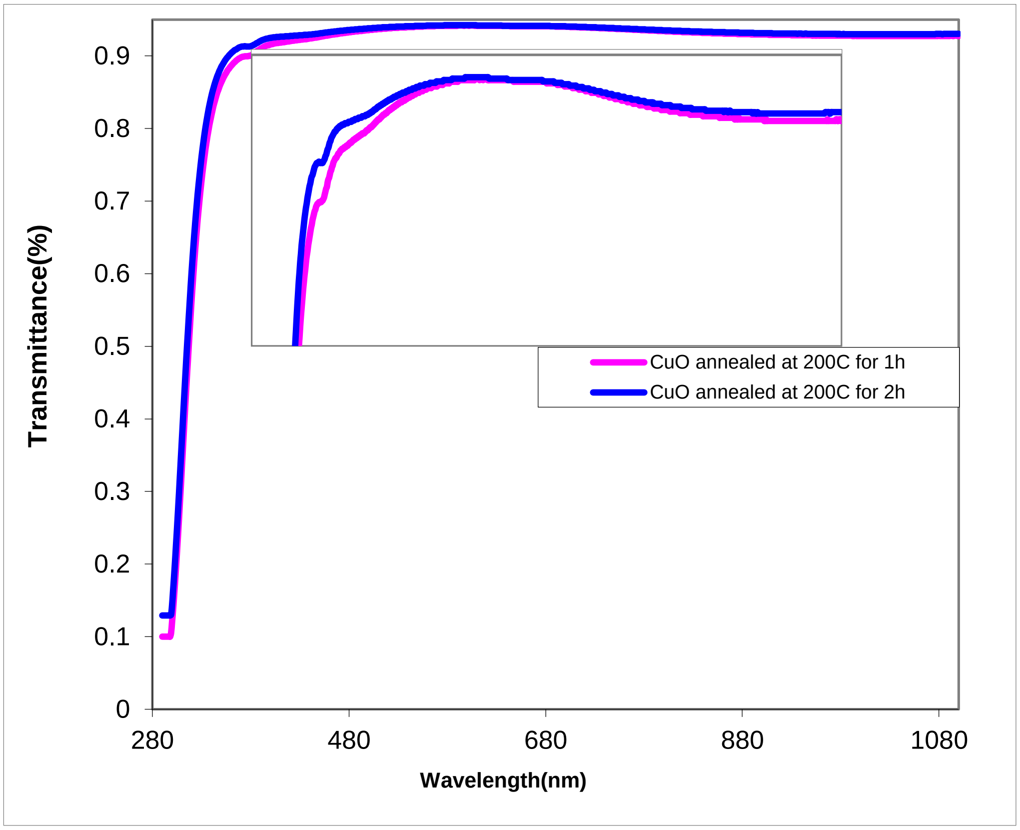

Figure(4.16): The Transmittance Spectra as a Function of Wavelength of CuO Thin Films at Various Annealing Time.

4.2.4.1.3 The Absorption Coefficient (α)

Figure (4.17) displays the optical absorption coefficient as a function of a wavelength for CuO thin film. The absorption coefficient was calculated using equation(2.15). The study of absorption coefficient spectra might expose the energy gap (E_g) among the valence band and the conduction band due to the transitions of direct and indirect for both amorphous and crystalline materials. It noticed that all the thin films prepared have high absorption coefficient ($\alpha > 10^4$ cm^{-1}) which indicates the increase of the probability of the occurrence of direct transitions. It is noticed from Figure (4.17) that the absorption coefficient of the films increased gradually with increasing the annealing temperature[70].

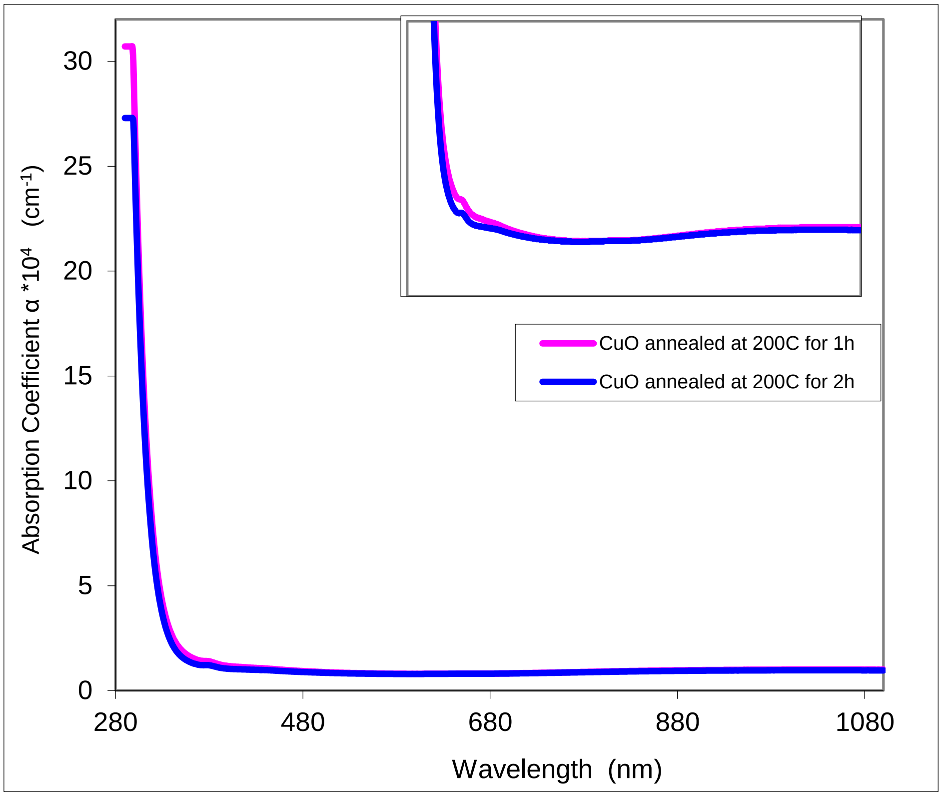

Figure (4.17): Absorption Coefficient (α) as a Function of wavelength for CuO Thin Film at Various Annealing Time.

4.2.4.1.4 The Optical energy gap (Eg)

The variance of direct for permitted transfer as a function of the photon energy of CuO thin film is depicted in Figure (4.18), according to the model of direct transition for amorphous semiconductors planned by Tauc [71]. Figure (4.18) shows the relation between $(\alpha h\upsilon)^2$ on the y-axis and photon energy ($h\upsilon$) on the x- axis. The optical energy gap of the allowable direct transition from the tangent extension of the curve was calculated to meet the photon energy axis at point $(\alpha h\upsilon)^2 = 0$. Since intersection point represent the optical energy gap of the allowed direct electronic transitions and was found to increase with the increasing of annealing temperature.

The optical energy gap was calculated by using equation(2.7). It is seen that the concentration of CuO rising in the system leads to increasing in Eg. From Figure (4.18), the energy gap increased from (3.6) to (3.65) eV. Table (4.2) shows the optical energy gap values for CuO thin films at various annealing time, the energy gap increased by increasing the annealing temperature of the preparing films due to decrease in the number of located levels between the conduction band and valence band[71] .

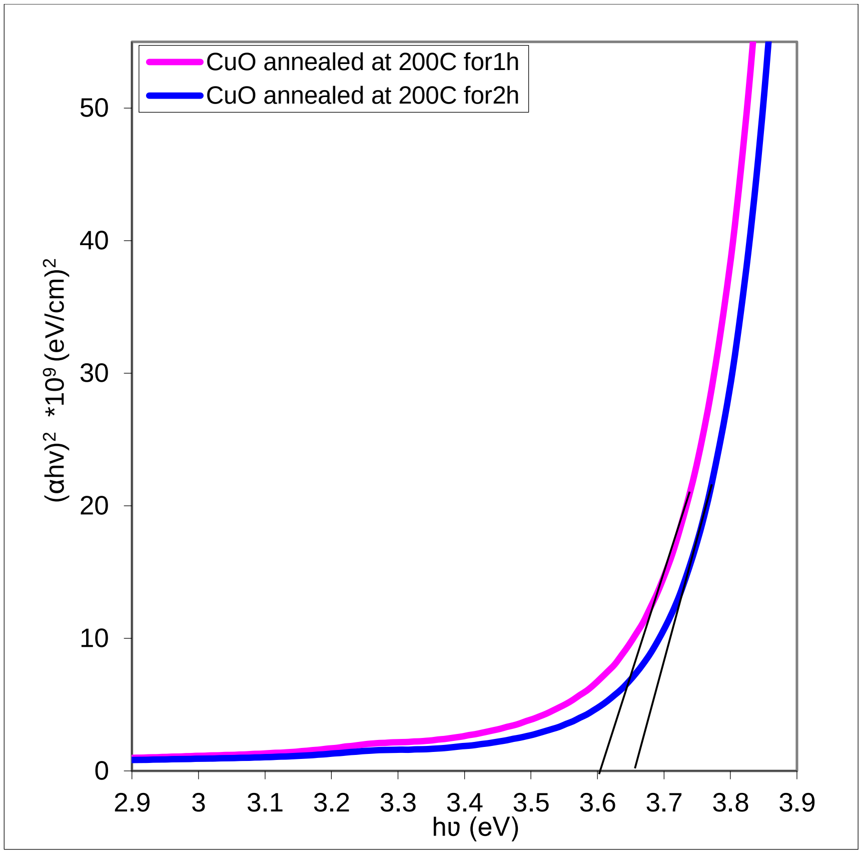

Figure (4.18): A plot of Optical Energy Gap $(\alpha h\nu)^2$Verses Photon Energy (hυ) of CuO Thin Films at Various Annealing Time.

Table (4.4): The optical energy gap of Cu_2O -doped CuO thin film annealed for one and two hours.

Thin Films Type	Optical Energy Gap (eV)
CuO annealed for 1hour	3.6
CuO annealed for 2 hour	3.65

4.2.4.1.5 The Extinction Coefficient (k)

The extinction coefficient (k) describes the properties of the material with respect to light of a given wavelength and indicates the absorption changes when the electromagnetic wave propagates through the material [95]. The extinction coefficient (k) were calculated by using equation (2.17), the extinction coefficient as a function of wavelength of pure CuO at various annealing temperature is shown in figure (4.19).

From this figure, it can be describe the relation between extinction coefficient and wavelength of deposited CuO films. It observed that the extinction coefficient increased with increasing the temperature to (200)˚C for two hours. The behavior explanation is the increased of the absorbance or the absorption coefficient and consequently (k) will increased which is in accordance with [97-98].

In general the behavior of (k) similar to the behavior of (α). This is attributed to the same reason mentioned previously. Since the increasing annealing temperature of CuO thin film leads to decrease the optical energy gap as a result of absorbance increased.

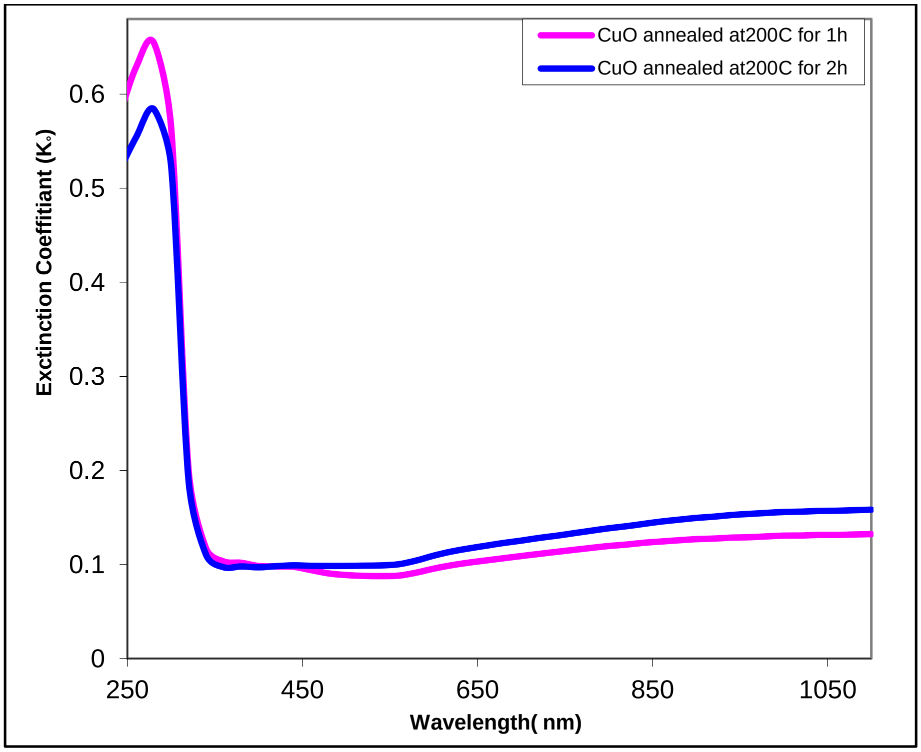

Figure(4.19): Variation of Extinction Coefficient with Wavelength of Pure CuO Thin Films at Various Annealing Time.

4.2.4.1.6 The Refractive Index (n)

Evaluation of the refractive indices of optical materials is considerably important for the applications in optics devices[99]. The index of refraction is useful for optical constants and calculated from the equation (2.16). The Figure (4.20) shows the variation of the refractive index versus wavelength in the range of (300–1100) nm for CuO films at annealing temperature for one and two hours at 200°C. It can display the increasing of refractive index by increased the temperature. This behavior can be explained on the basic of that increased the annealing temperature leads to make prepared samples more dense and the change in crystalline structure, which in turn increasing propagation velocity of light through the sample, which results increasing of the refractive index (n)[71] .

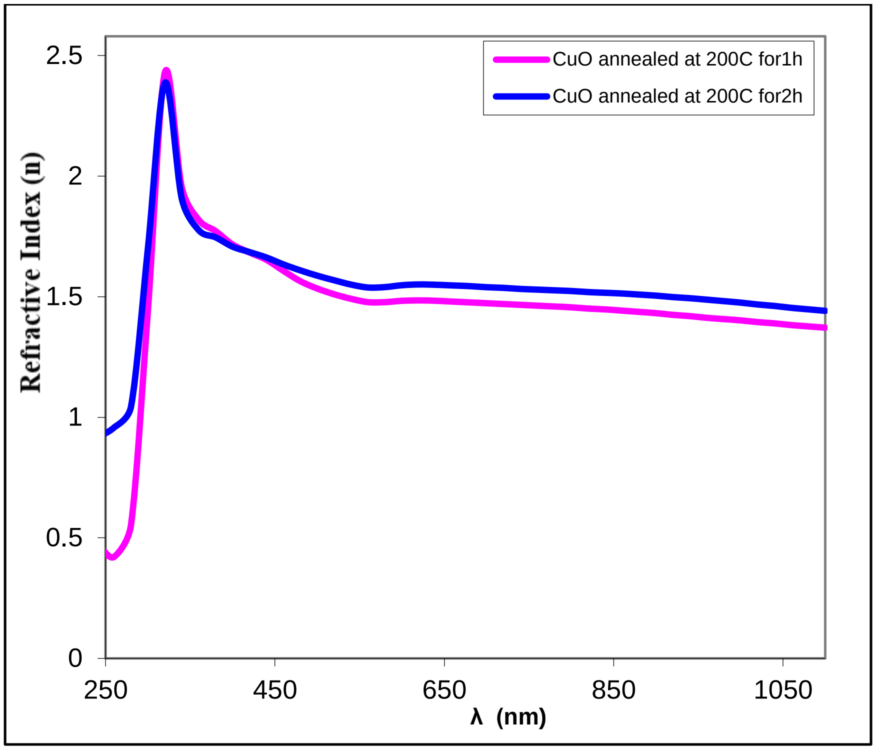

Figure(4.20): Variation of Refractive Index with Wavelength of Pure CuO Thin Films at Different Annealing Time.

4.2.4.1.7 The Dielectric Constant (ε_r, ε_i)

The real (ε_r) and imaginary (ε_i) dielectric constants for CuO thin films system are determined by using equation (2.18), the variation of real (ε_r) and imaginary (ε_i) parts of dielectric constant values versus wavelength for pure and doped CuO thin film as displays in Figures (4.21) and (4.22). The real and imaginary portions of the dielectric constant were improved because of the extinction coefficient and refractive index amassed [100]. It is found that ε_r and ε_i increases with increasing the annealing time for two hours. This behavior of ε_r is similar to that of the refractive index because of the smaller value of K^2 compared with n^2, while ε_i is mainly depended on the k values according to equation (2.14). This behavior is in agreed with the results as [56].

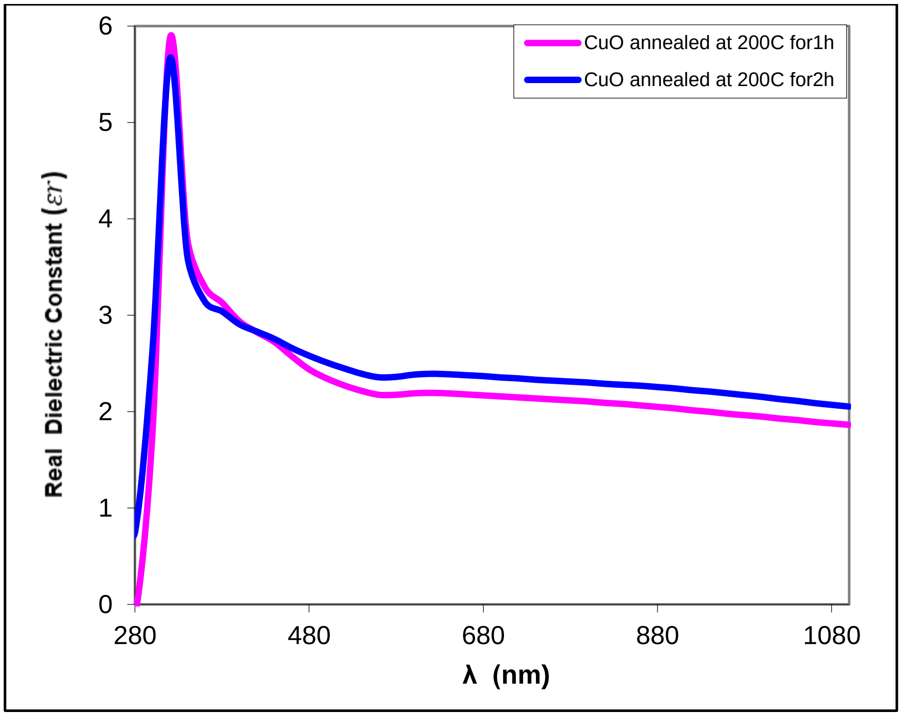

Figure(4.21):Variation of (ε_r) with Wavelength of Pure CuO Thin Films at Various Annealing Time.

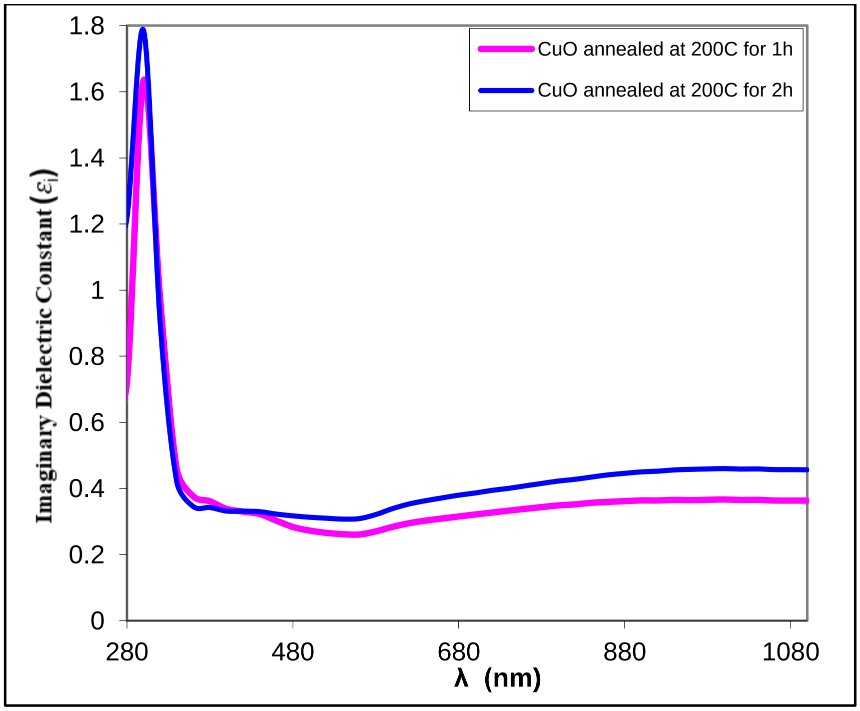

Figure(4.22):Variation of (ε_i) with Wavelength of Pure CuO Thin Films at Various Annealing Time.

The optical properties of CuO, after doping various amount of Cu_2O thin films were include spectral transmittance (T) and absorbance (A). Then, they were studied by recording the absorbance spectra at the range of wavelength between (300-1100) nm. Will changes as following

4.2.4.2.1The absorbance

After doping with various amount of Cu_2O –doped CuO. It can be observed that the absorbance increased with the increasing the Cu_2O -doped for the prepared thin films. It can be noticed that absorbance increases after annealing temperature. This is due to Increase crystallization of the material and reduce crystalline defects, as shown in Figure (4.23)[101].

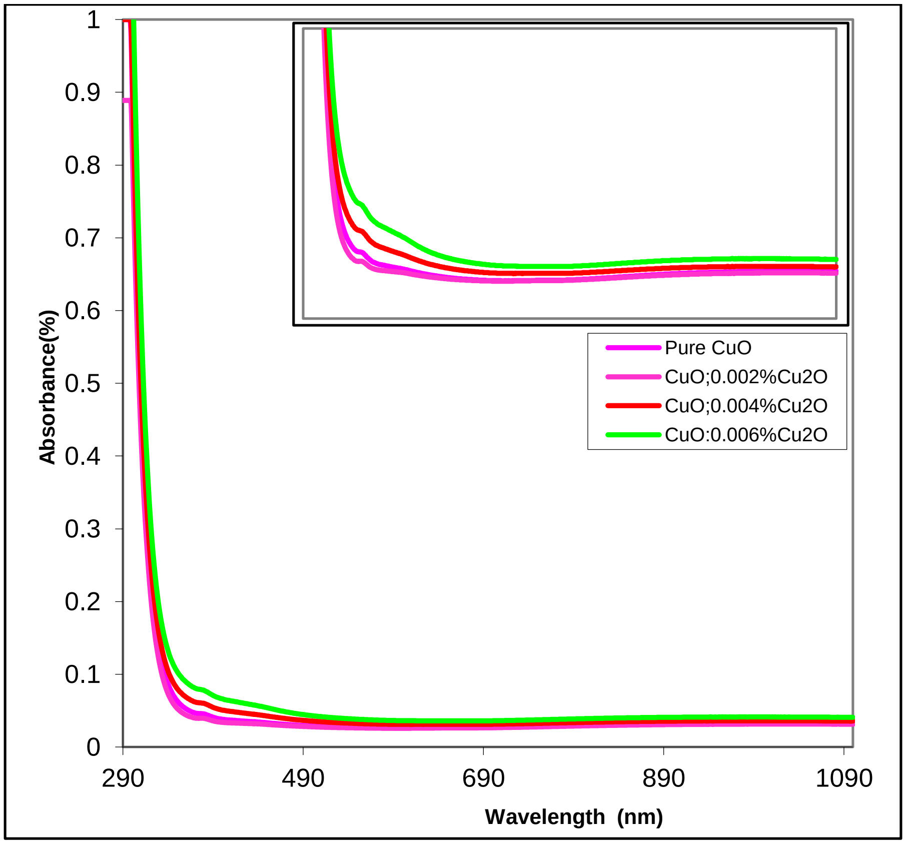

Figure (4.23):The Absorbance Spectra as a Function of Wavelength of $CuO:Cu_2O$ Thin Films with Various Weight ratios of Cu_2O.

4.2.4.2.2 The Transmittance

From Figure (4.24), After doping with various amount of Cu_2O. For the prepared thin films, it can be observed that the average transmittance of Cu_2O thin film decreases with increasing of Cu_2O -doped and then dropped This may be due to the increase in film homogeneity, with the increase of the surface roughness promoting the increase of the surface scattering of the light, which is in accordance with Beer-Lambert law and the findings agreement with [62-102] .

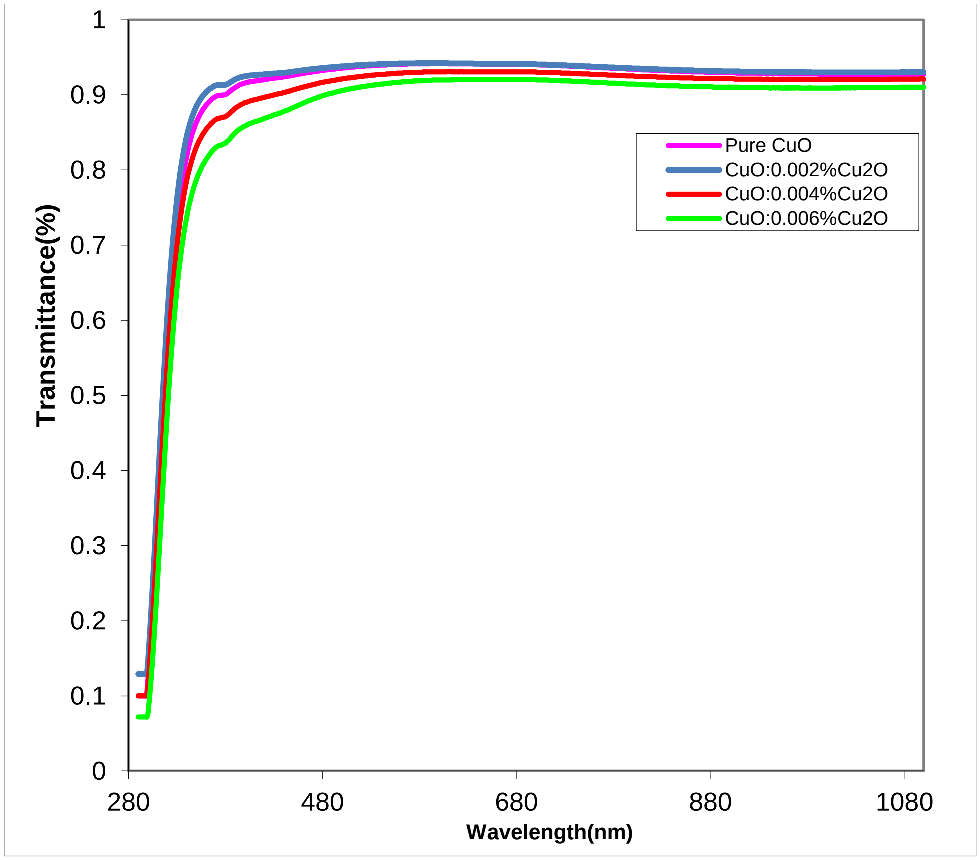

Figure (4.24):The Transmittance Spectra as a Function of Wavelength of $CuO:Cu_2O$ Thin Films with Various Weight Ratios of Cu_2O.

4.2.4.2.3 The Absorption Coefficient

Absorption coefficient (α) of CuO:Cu_2O thin films are calculated by using equation (2.15). The absorption coefficient is determined from the region of high absorption at the fundamental absorption edge of the thin films, the variation of the absorption coefficient versus wavelength for pure CuO and Cu_2O –doped CuO with different ratio of Cu_2O (0.006) wt.%. Figure (4.25) shows the plot of (αhυ) with the incident photon energy (hυ) of the CuO films, the copper oxide thin films prepared through the thermal evaporation method are direct transition, a straight line can be used higher energy, which is in agreement with [103, 104] . The band gap of the CuO thin films can be determined by extrapolating the linear part of the graph to the hυ of the x-axis. To fitting the curve as tabled in Table (4.5).

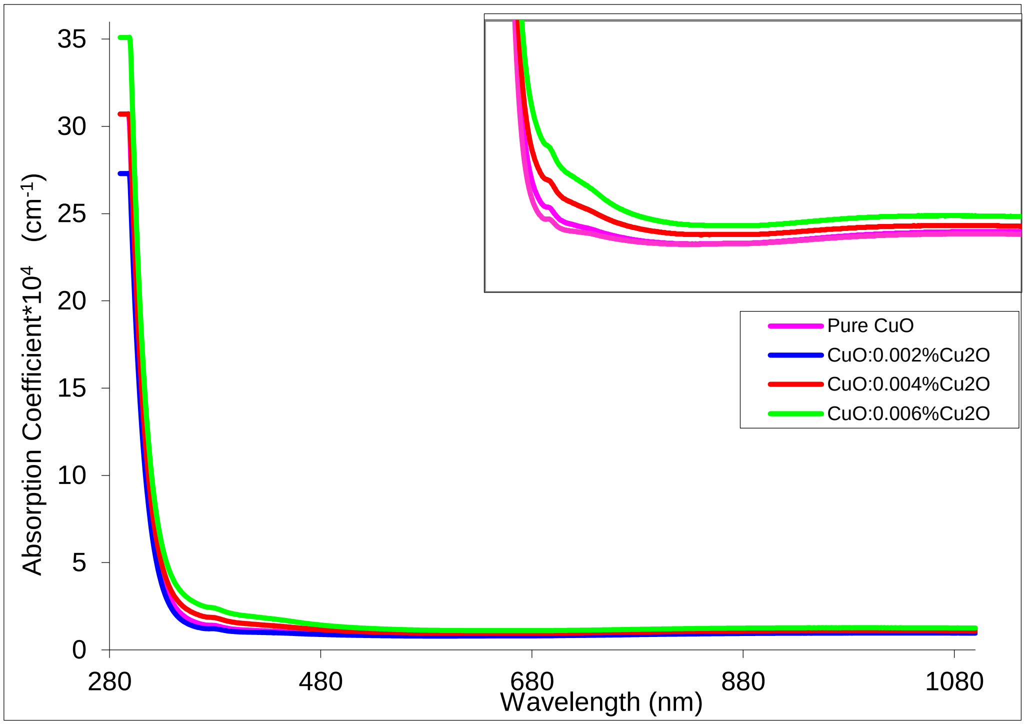

Figure (4.25): A plot of $(\alpha h\nu)^2$Verses Photon Energy (hυ) of CuO:Cu_2O Thin Films with Various Weight Ratios of Cu_2O.

4.2.4.2.4 The Optical Energy Gap

After annealing for two hours with various amount of Cu_2O-doped CuO. For the prepared thin films, it can observe that the concentration of CuO rising in the system leads to a reduction in energy gap. From Figure (4.26) the energy gap reduced from (3.58) to (3.42) eV as listed in Table (4.5). This decrease in the energy gap by refer that the CuO nanofilm after doping with various amount of Cu_2O. This decreased in energy gap can be due to the prohibited impurities that led to the formation of secondary located levels within the energy gap near the conduction band. Thus, it will absorb photons of low energy. These results show a good agreement with the findings of researchers[37,88,89].

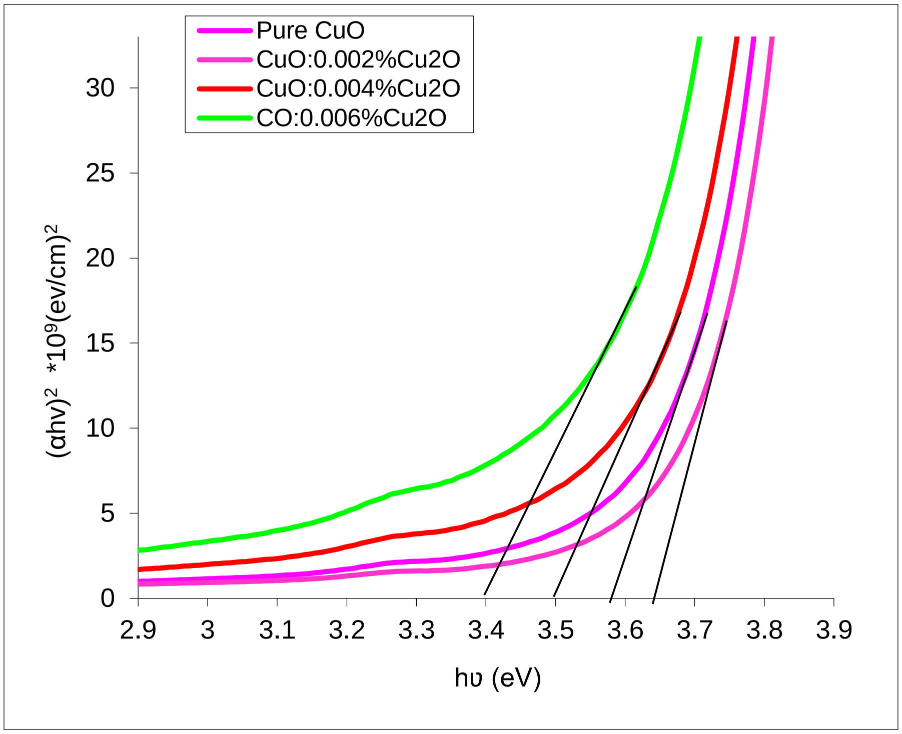

Figure (4.26): A plot of Optical Energy Gap $(\alpha h v)^2$Verses Photon Energy (hυ) of CuO:Cu_2O Thin Films with Various Weight Ratios of Cu_2O.

Table (4.5): The optical energy gap of Cu_2O -doped CuO thin film at various weight ratios of Cu_2O.

Films Type	Optical Energy Gap (eV)
Pure CuO	3.64
CuO:0.002wt. % Cu_2O	3.58
CuO:0.004 wt. % Cu_2O	3.5
CuO:0.006 wt. % Cu_2O	3.4

4.2.4.2.5 The Extinction Coefficient

It was observed that the extinction coefficient varies with the wavelength, and the peak of the extinction coefficient increases with increasing the doping weight ratios of Cu_2O due to the increase the absorption coefficient, where the extinction coefficient depends on the absorption coefficient. From Figure (4.27) it is found that the extinction coefficient is increasing with the increasing of Cu_2O doping for all prepared thin films. This is in agreement with [105].

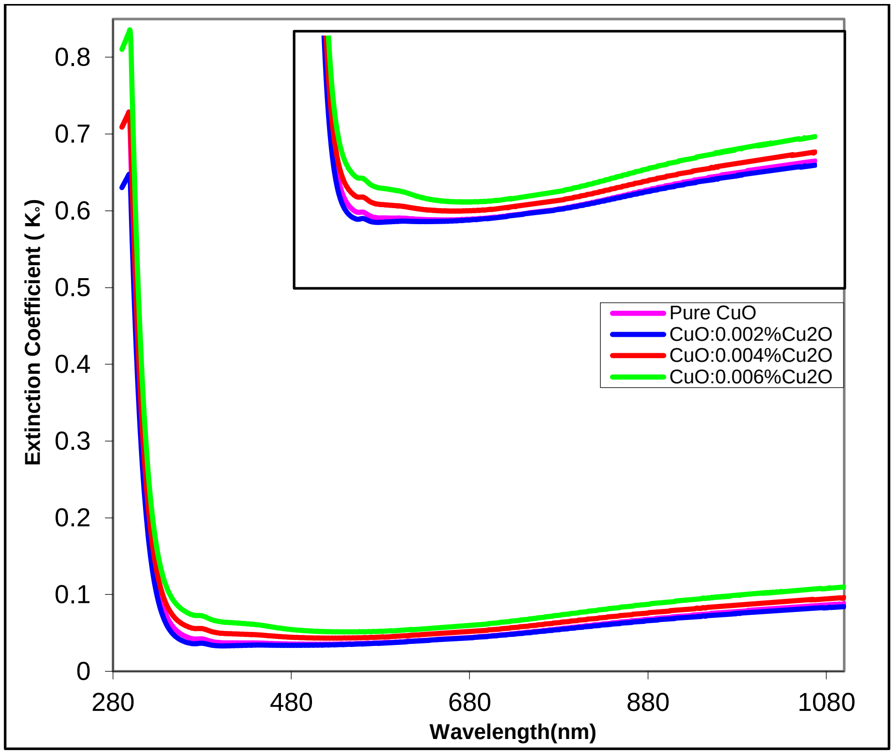

Figure(4.27):Variation of Extinction Coefficient with Wavelength of CuO:Cu_2OThin Films with Various Weight Ratios of Cu_2O.

4.2.4.2.6 The Refractive Index

From Figure (4.28), it can be noticed that the refractive index increase with the increasing of Cu_2O doping. An increase in the particle size of CuO film increases the refractive index. In other words, when the incident light interacts with a material which has a high amount of particles then the refractivity of the thin films increases. This is in agreement with [105].

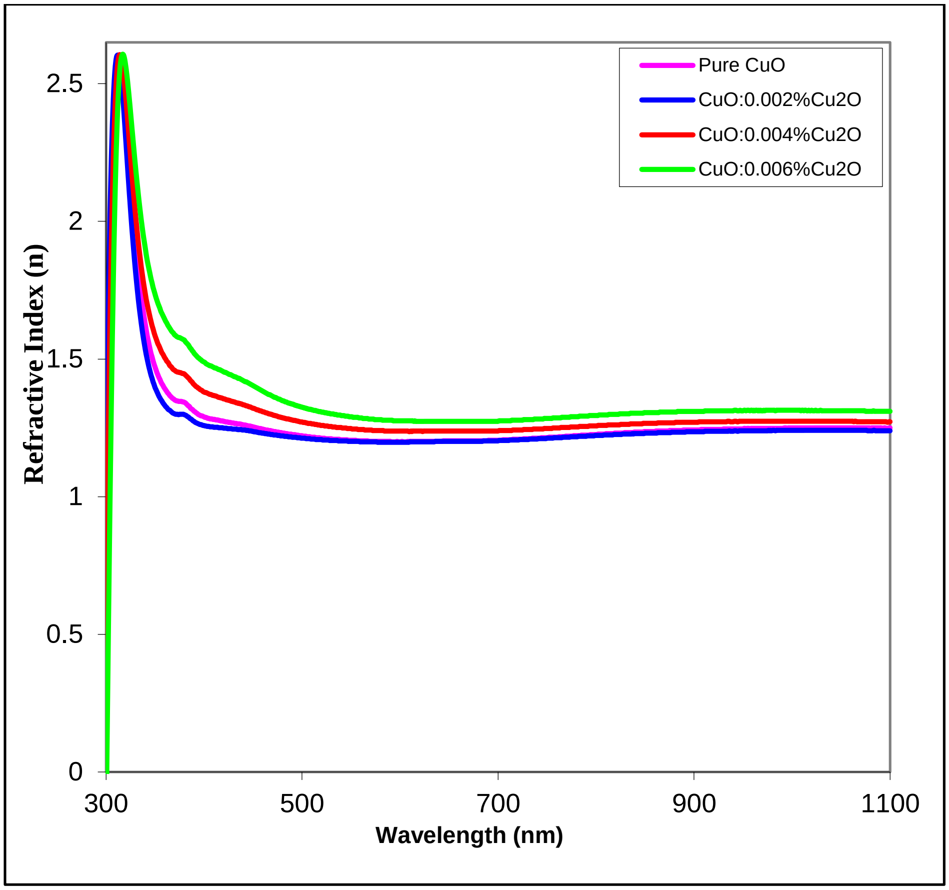

Figure(4.28):Show the Variation of Refractive Index with Wavelength of CuO:Cu_2O Thin Films with Various Weight Ratios of Cu_2O.

4.2.4.2.7 The Dielectric Constant ($\varepsilon_r, \varepsilon_i$)

The variation of real (ε_r) and imaginary (ε_i) parts of dielectric constant values versus wavelength for pure and Cu_2O- doped CuO thin films with different doping of Cu_2O (0.002, 0.004 and 0.006) wt.% are presenting in Figure (4.29) and (4.30). From these figures, found that ε_r and ε_i increase with doping ratio of Cu_2O.

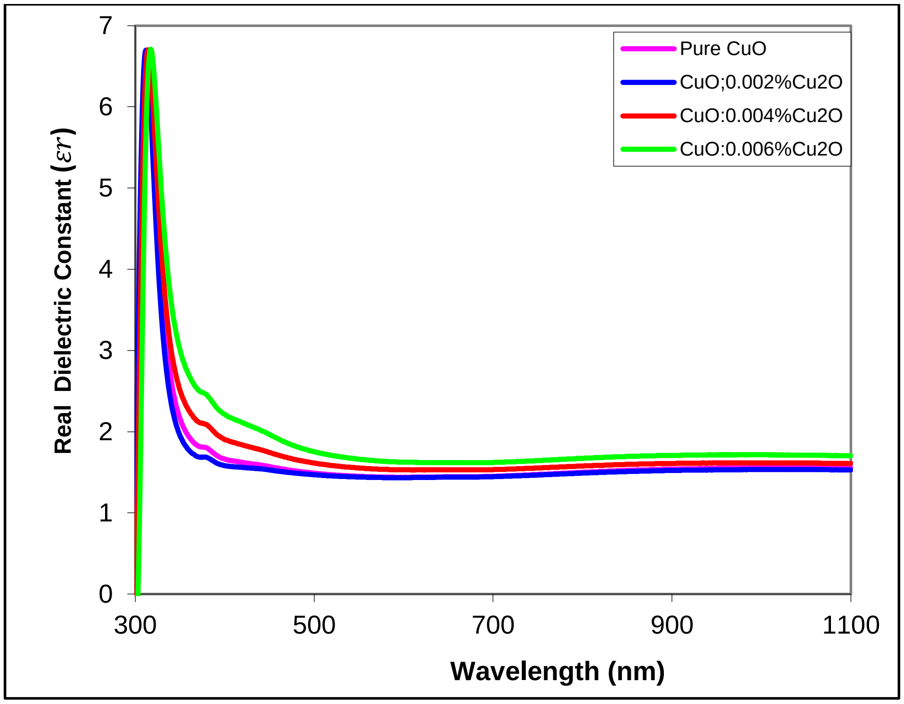

Figure(4.29):Variation of (ε_r) with Wavelength of CuO and CuO: Cu_2O Thin Films with Various Weight Ratios of Cu_2O.

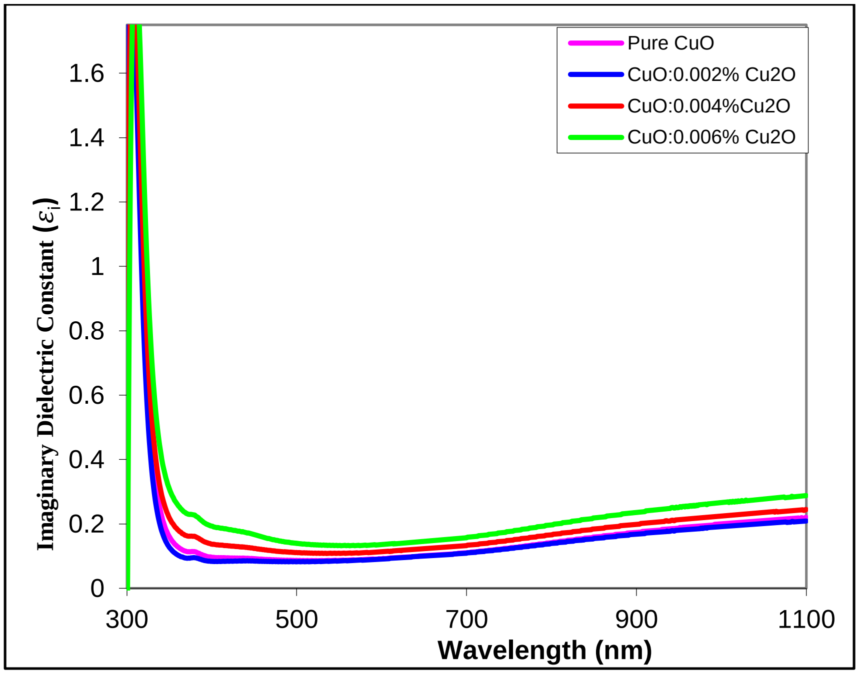

Figure(4.30):Variation of (ε_i) with Wavelength of CuO and CuO: Cu_2O Thin Films with Various Weight Ratios of Cu_2O.

4.2.5 Hall Effect

Hall voltage parameters were made of pure and CuO-doped Cu_2O thin films prepared by thermal evaporation technique by using Van-der Pau method at thickness(75) nm. The hall parameters such as, hall coefficient (R_H), carrier concentrations electrical conductivity(σ), and Hall mobility have been determined by using (Van-der Pauw) system that tabulated in table (4.6). It is obvious that the Hall coefficient increased with the increasing of Cu_2O weight ratios. In addition the (R_H) of the samples is negative, which indicated that the Cu_2O:CuO thin films are of n-type conduction, which is in accordance with [71].

For the purpose of identifying the type of charge carriers, their concentration, hall coefficient values, resistivity, and conductivity and mobility at room temperature. Hall coefficient (R_H) value, Cu_2O-doping of (0.004) wt.% thin films were converted from p-type to n-type from hall coefficient with (-4.425×10^8) of (R_H) value.

The reason for this transformation is the increasing in energy, which has resulted in a decrease in the crystallite size of the thin film. In addition, the values of the Hall coefficient are disparate for the n- type due to the increasing in energy due to the change in the crystallite size and the granular assemblies on the film due to deposition. It is noted from Table (4.6) the carrier concentration of the samples increased with increasing of Cu_2O -doping (0.006) wt.% .In addition, the (R_H) of the samples is (-2.722×10^8) negative, which indicates that the CuO:Cu_2O thin films are n-type conduction. Therefore, CuO:Cu_2O doping can be increase the carrier concentration, accordance with [106].

Table (4.6): The results of hall measurements for Cu_2O -doped CuO with various Weight ratio.

Sample Name	**Carriers Concentration n cm^{-3}**	**Conductivity $\sigma(\Omega.cm)^{-1}$**	**Resistivity $\rho(\Omega.cm)$**	**Mobility $\mu_H(cm^2/V.s)$ $\times 10^2$**	**Hall Effect $R_H(cm^2/C)$**	**Type of Carriers**
Pure CuO	6.721×10^{10}	2.422×10^{-7}	4.13×10^{6}	3.112×10^{2}	-3.546×10^{8}	n-type
CuO:0.002%Cu_2O	2.463×10^{10}	3.011×10^{-7}	3.321×1^{6}	2.424×10^{5}	-5.233×10^{8}	n-type
CuO:0.004%Cu_2O	5.856×10^{10}	4.341×10^{-7}	2.3×10^{6}	2.532×10^{5}	-4.425×10^{8}	n-type
CuO:0.006%Cu_2O	6.024×10^{10}	1.856×10^{-7}	5.4×10^{6}	4.022×10^{5}	-2.722×10^{8}	n-type

4.2.6 Current-Voltage Characteristic of CuO:Cu_2O Heterojunction under Dark and Illuminated Conditions

The study of current-voltage (I-V) properties in states of dark and lighting are important because it is a clear indication of the possibility of using CuO thin films as a light-sensitive material (solar cell). Where observing the effect of light is evident in the change of current and voltage values of the prepared samples the CuO: Cu_2O films by doping various content of Cu_2O (0.002, 0.004 and 0.006) wt.%. The junction Si/CuO:Cu_2O is formed by thermal evaporation technique, and experimental by I-V curves, which are of various behaviors according to the ambient of preparing the junction, the pure CuO and CuO:Cu_2O were n-type semiconductors.

Where (I_d) was the current under dark conditions, (I_t) is the current under illuminated conditions, and (I_{ph}) is the photocurrent ($I_{ph}=I_t-I_d$). Under the dark conditions, the current–voltage (I-V) characteristics are an important parameter to identify the importance of the various components under reverse and forwarding bias as well as other important parameters. The I-V curves of CuO:Cu_2O solar cell are explained in Figure (4.31). The I-V characteristic for Si/CuO:Cu_2O HJ at forward bias voltage for different CuO ratios within the range (-6 to 3.5)Volt.

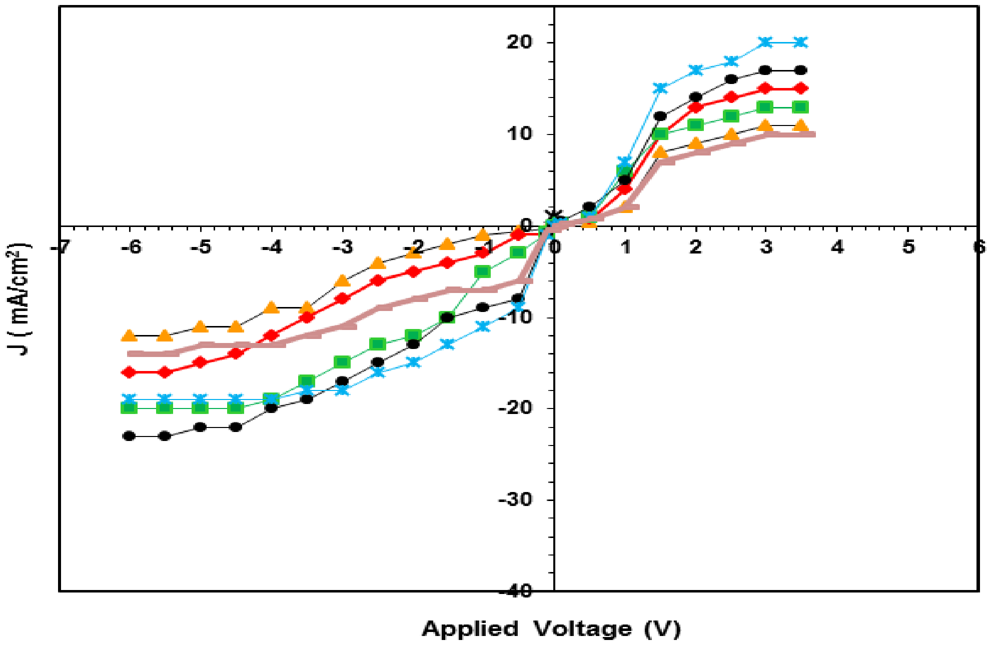

Figure(4.31): I-V Characteristic in Dark for Film of CuO:Cu_2O Solar Cell Under P=100 Mw/cm^2 .

These curves exhibit the behavior of the current with the reverse bias voltage. The current-voltage characteristic under dark is one of the optoelectronic typical for film. The measurements are passed out under incident power densities equal to (100 mW/cm^2).

That increased sensitivity of the samples after lighting changes when the silicon sample is a p-type that used with the n-type of CuO:Cu_2O films. These heterojunction structures produced by thermal evaporation have good rectifying properties. The current does not pass through the heterojunction in the dark state.

From Figures ((4-32)─(4.39)), with annealing temperatures for one and two hours for (200) °C it is obvious that the photocurrent is increased with increasing the annealing temperature for two hours as the bias voltage increases. The efficiency increased from (1.178571) to (3.642857) can also be obtained with an increase in Cu_2O doping from pure CuO to 0.006%.wt in the CuO films respectively.

This can be attributed to the fact that the width of the depletion region increased with the increasing of the applied reverse bias voltage that leads to the separation of the electron–hole pairs. Then, the increasing of the applied reverse bias voltage after doping may have been caused by the shift of the fermi level of the CuO to the center of the optical band gap due to increasing carrier concentration, which in accordance with [107].

The efficiency increased with increasing of Cu_2O doping can be obtained with an increase in CuO ratio thin film from 0.002%.wt to 0.006%.wt Cu_2O doping, the highest efficiency at doping 0.006% Cu_2O is 3.642857% with V_{oc} of 1.95 V, I_{sc} of 0.0180 $mA.cm^{-2}$, and F.F of 0.7264, also the highest efficiency at doping 4% Cu_2O is 3.471429% with V_{oc} of 2.20V, I_{sc} of 0.0170 $mA.cm^{-2}$ and F.F of 0.6497. The improved device performance is caused by the high I_{sc} and V_{oc} of this device. The results are listed in Table (4-7). That good agreement with [108-109].

The Cu_2O -doping increases the energy conversion efficiency by retarding the electron-hole recombination. These results exhibit that the extrinsic influences, such as specific surface area, are very important to improve the performance of CuO:Cu_2O solar cells.

Due to the presence of impurities that occurs during the deposition process, back aluminium contact resistance and electron-hole recombination. The value of short circuit current is usually low which causes the solar cell to experience somewhat higher resistance to the flow of charges. The measurement of the quality of a solar cell eventually obtained by the squareness of the current-voltage curve is the fill factor (FF) theoretical power (TP) that would be the result at short circuit current and open-circuit voltage altogether.

The fill factor and conversion efficiency of the assembled solar cell were achieved using equations (2.27) and (2.28) respectively. Fill factor estimate was seen to be 0.7264. Using equations (2.29) and incident power of 100W.cm^2 from the solar simulator’s illuminated on the fabricated solar cell, the conversion efficiency (η) which is the ratio of P_{out}, the electrical power output compared to P_{in}. By using equations (2.30). This corresponds [110,111] .

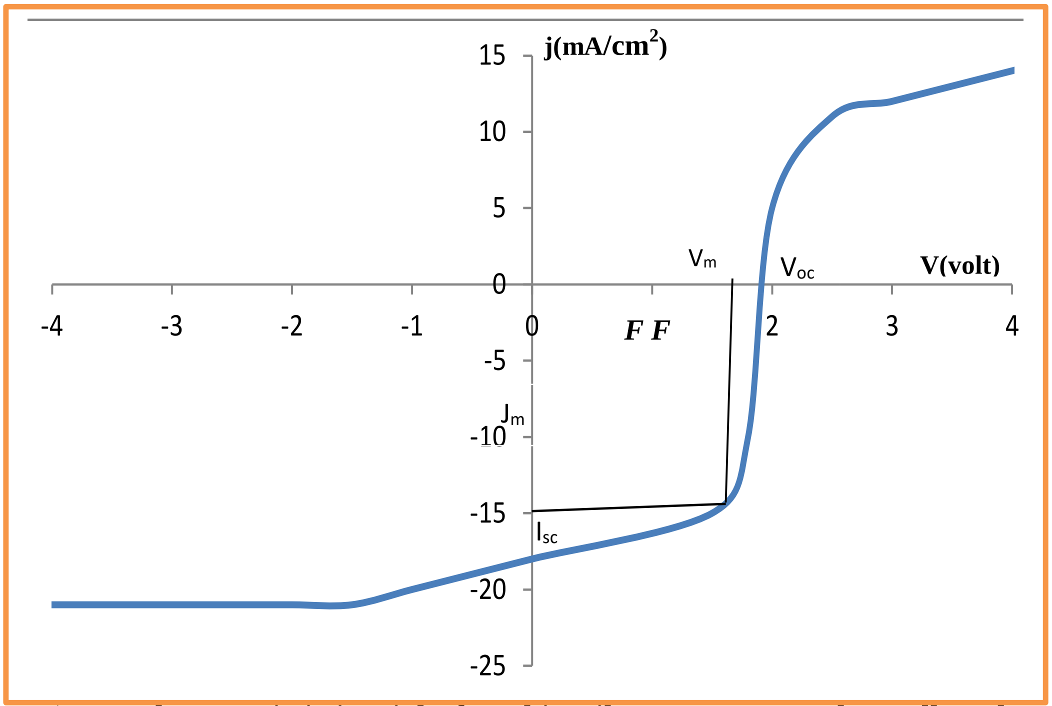

Figure(4.32):I-V Characteristic in Light for Thin Film Pure CuO Solar Cell Under P=100 Mw/cm^2 for One Hour.

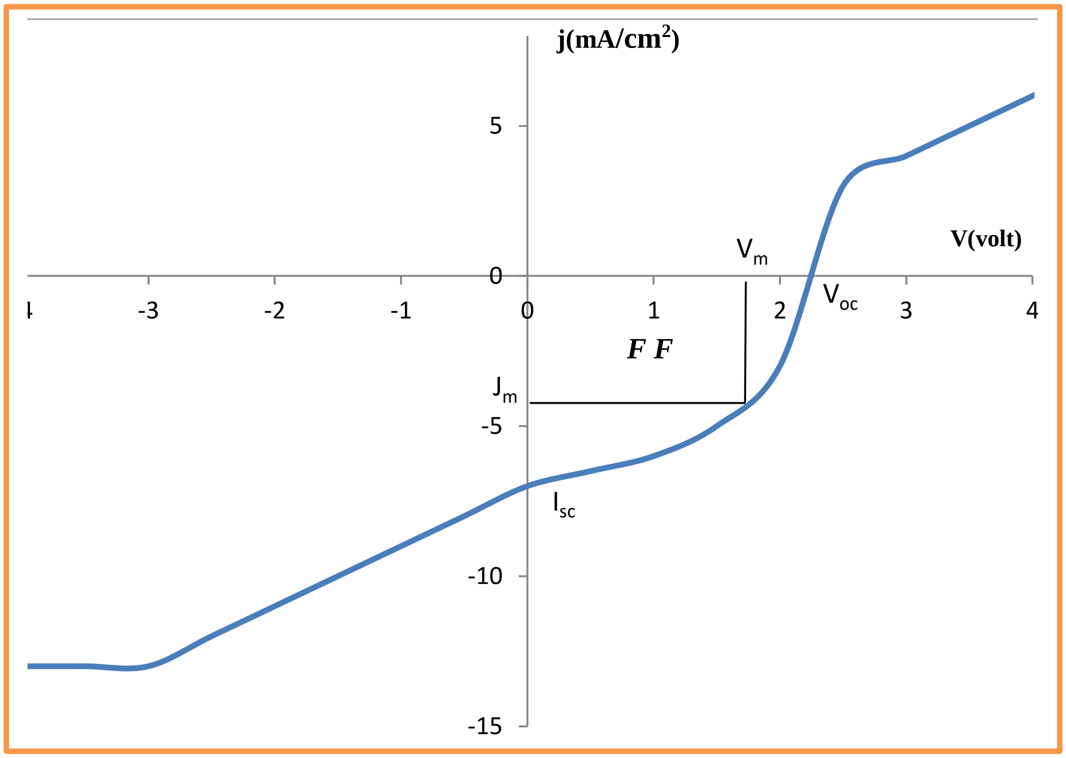

Figure(4.33): I-V Characteristic in Light forThin Film Pure CuO Solar Cell Under P=100 Mw/cm^2 for Two Hours.

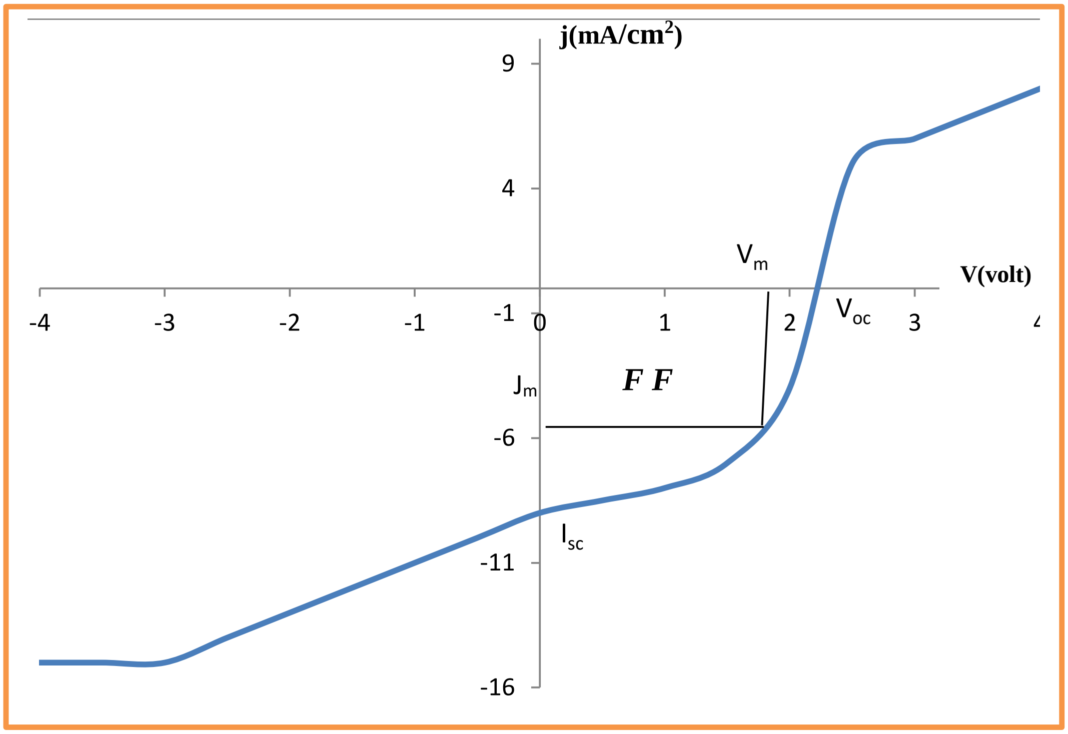

Figure(4.34):I-V Characteristic in Light for Thin Film CuO:0.002wt %Cu_2O Solar Cell Under P=100 Mw/cm^{2}for One Hour.

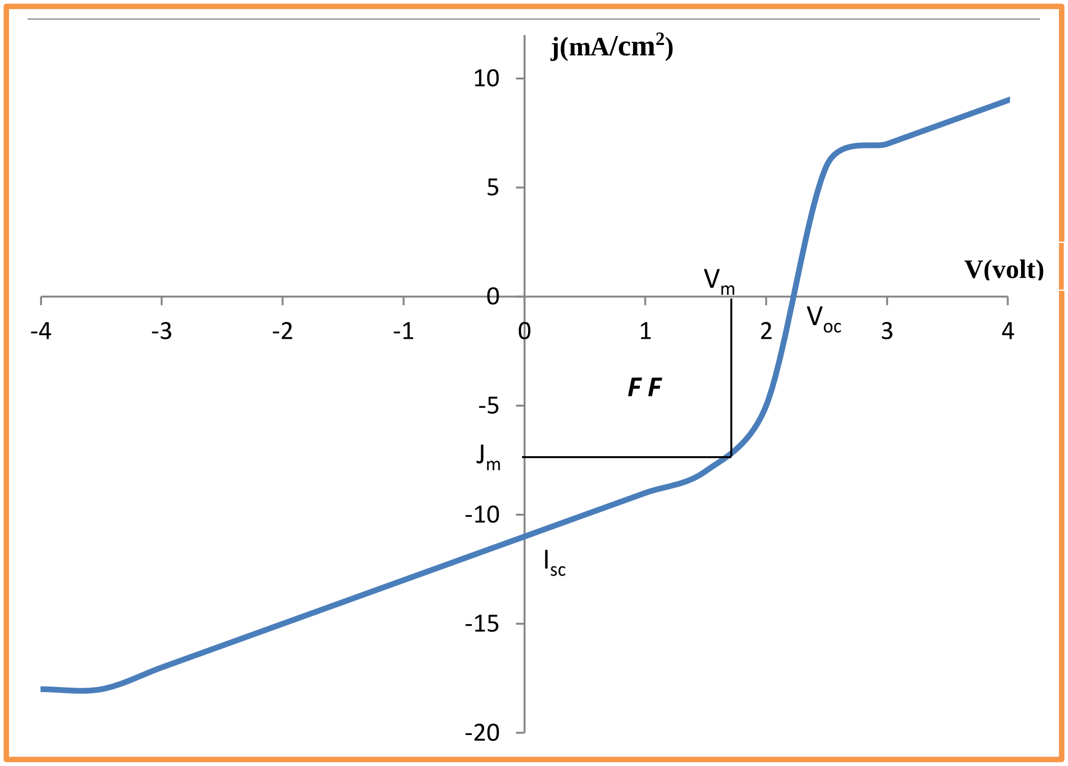

Figure(4.35):I-V Characteristic in Light for Thin Film CuO:0.002wt %Cu_2O Solar Cell Under P=100 Mw/cm^2 for Two Hours.

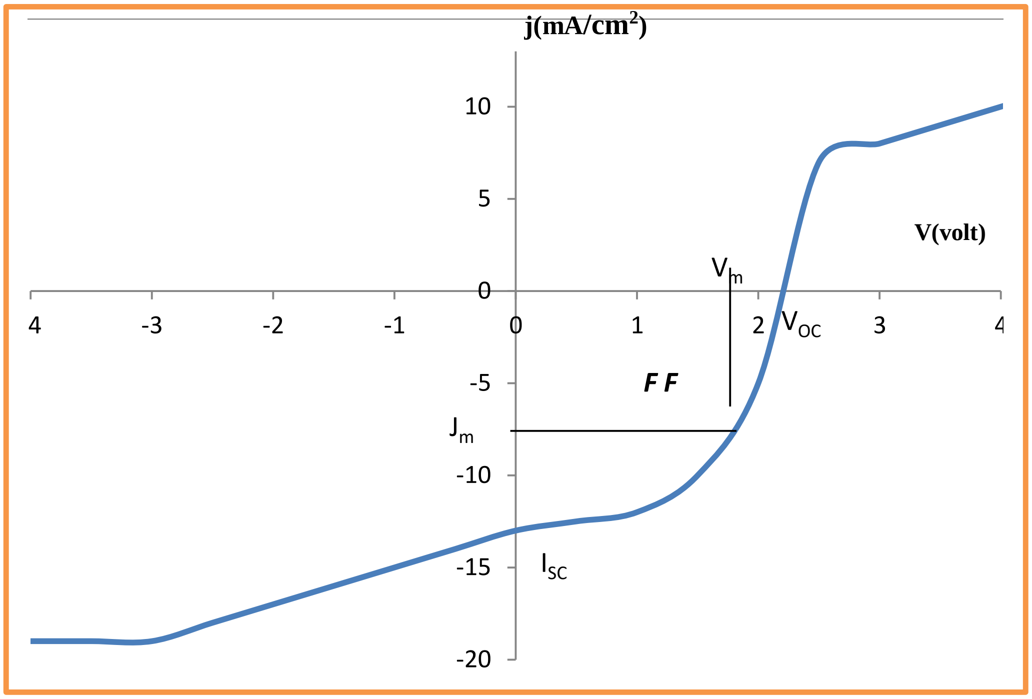

Figure(4.36):I-V Characteristic in Light for Film CuO:0.004wt%Cu_2O Solar Cell Under P=100 Mw/cm^2 for One Hour.

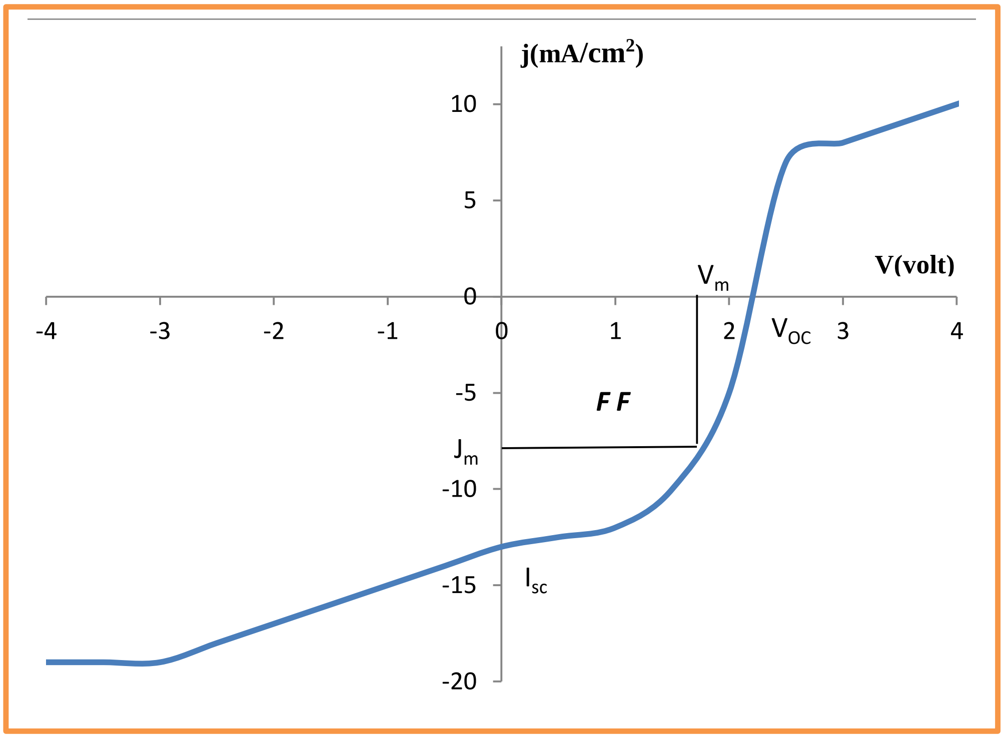

Figure(4.37):I-V Characteristic in Light for Film CuO:0.004wt%Cu_2O Solar Cell Under P=100 Mw/cm^2 For Two Hours.

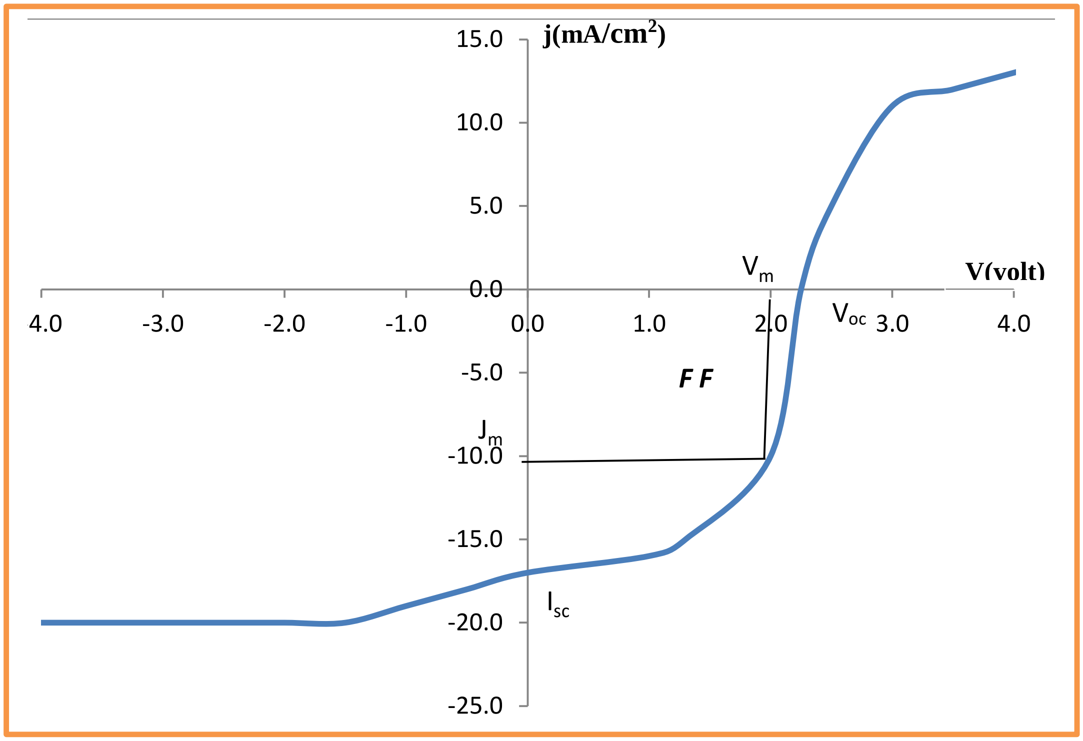

Figure(4.38):I-V Characteristic in Light forThin Film CuO:0.006wt%Cu_2O Solar Cell Under P=100 Mw/cm² For One Hour.

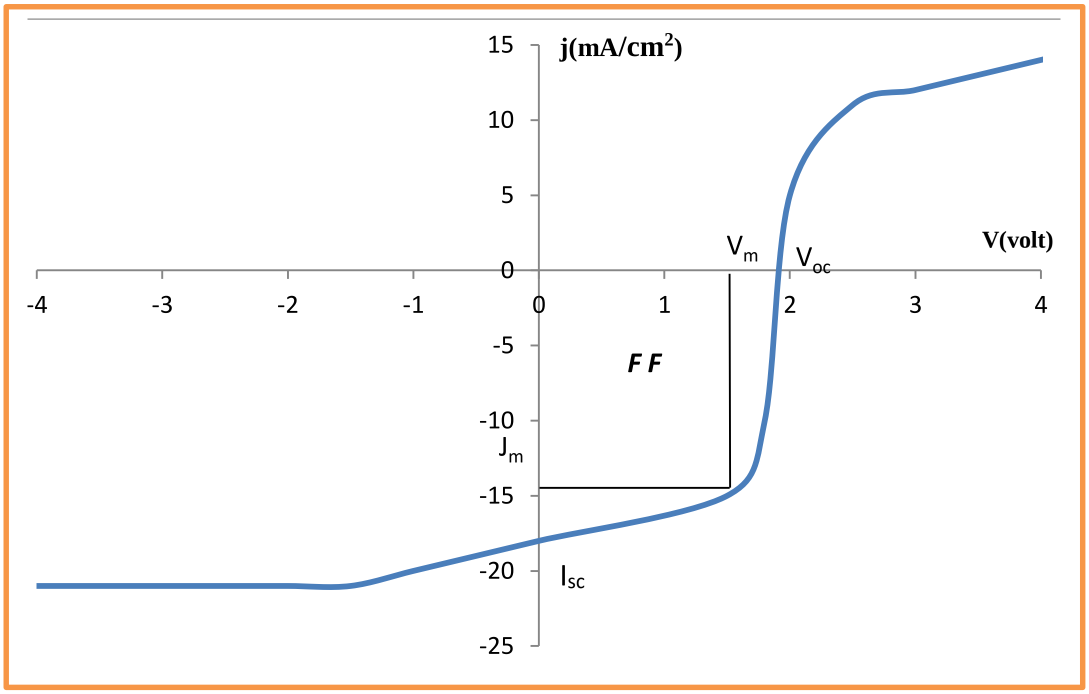

Figure(4.39):I-V Characteristic in Light for Film CuO:0.006wt %Cu_2O Solar Cell Under P=100 Mw/cm² for Two Hours.

Table(4.7): The results of the I-V for Cu_2O -doped CuO thin film at various Weight ratios of Cu_2O.

Sample Name	V_{oc} (mV)	I_{sc} (mA)	Vmax (mV)	Imax (mA)	F.F	Eff.
Pure CuO annealed for 1h	2.20	0.0050	1.9	0.0038	0.6563	1.031429
Pure CuO annealed for 2h	2.20	0.0065	1.5	0.0055	0.5769	1.178571
$CuO:0.002Cu_2O$ annealed for 1h	2.20	0.0090	1.6	0.0070	0.5656	1.6
$CuO:0.002Cu_2O$ annealed for 2h	2.25	0.0110	1.5	0.0080	0.4848	1.714286
$CuO:0.004Cu_2O$ annealed for 1h	2.20	0.0130	1.5	0.0110	0.5769	2.357143
$CuO:0.004Cu_2O$ annealed for 2h	2.20	0.0150	1.6	0.01250	0.6060	2.857143
$CuO:0.006Cu_2O$ annealed for 1h	2.20	0.0170	1.8	0.01350	0.6497	3.471429
$CuO:0.006Cu_2O$ annealed for 2h	1.95	0.0180	1.7	0.0150	0.7264	3.642857

4.2.7 Capacitance-Voltage Characteristics

The current-voltage characteristics of the best pure Cuo and $CuO:Cu_2O$ solar cells have been recorded in darkness and under 100 mW/cm^2 illumination, point by point. The reciprocal of square capacitance versus reverse bais voltage,as shown in Figures from (4.40-4.47), depicts an abrupt junction for Cu_2O-doping CuO.

The increasing with various concentrations of Cu_2O result in increasing the built-in potential which annealing for two hours, this is attributed to the improving in junction characteristics and indicates an improvement in photovoltaic characteristics. It is noted that the open circuit voltage V_{oc} decreased from (2.20-1.95), and the short circuit current density I_{sc} decrease from ((0.0050)-(0.0130)) with increasing of annealing temperature and doping with Cu_2O. As represented in table (4.8), V_{oc} drops because of increasing reverse current saturation with temperature because minority carriers increase with increasing in temperature. I_{sc} decrease because of increase the recombination of the charges which is agree with [112].

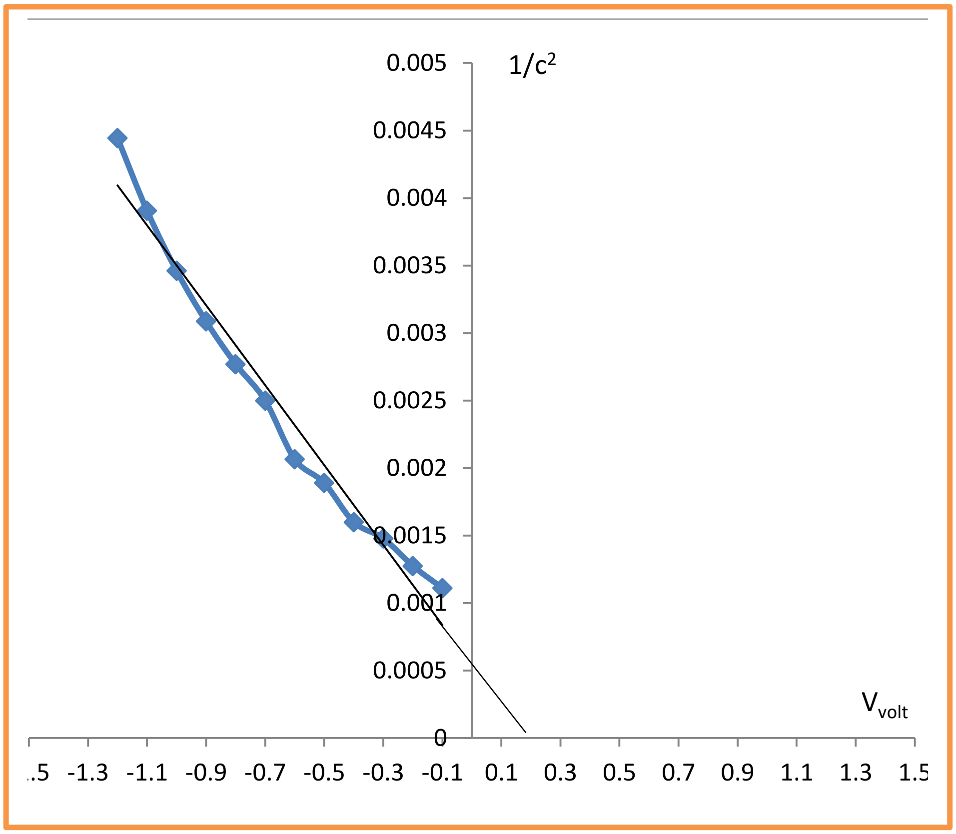

Figure(4.40): $1/c^2$Vs Applied Voltage of Pure CuO Thin Films at Annealing Temperature (200)°C for One Hour.

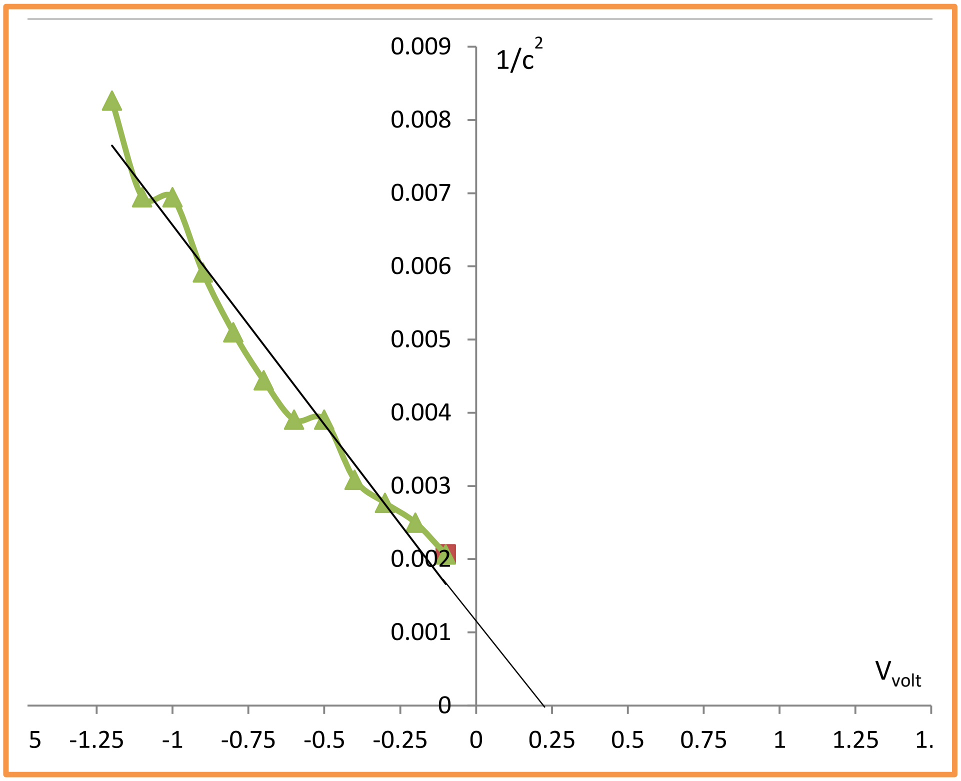

Figure(4.41) :1/c² Vs Applied Voltage of pure CuO Thin Film at Annealing Temperature(200)°C for Two Hours.

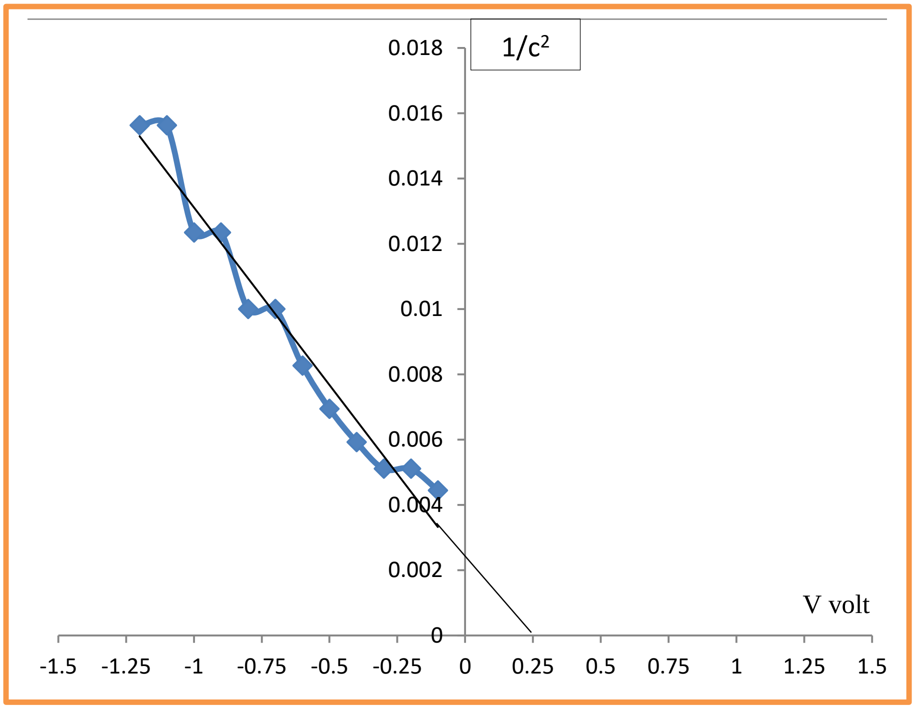

Figure(4.42) :1/c² Vs Applied Voltage of CuO: 0.002 wt% Cu_2O Thin Film at Annealing Temperature (200)°C for One Hour.

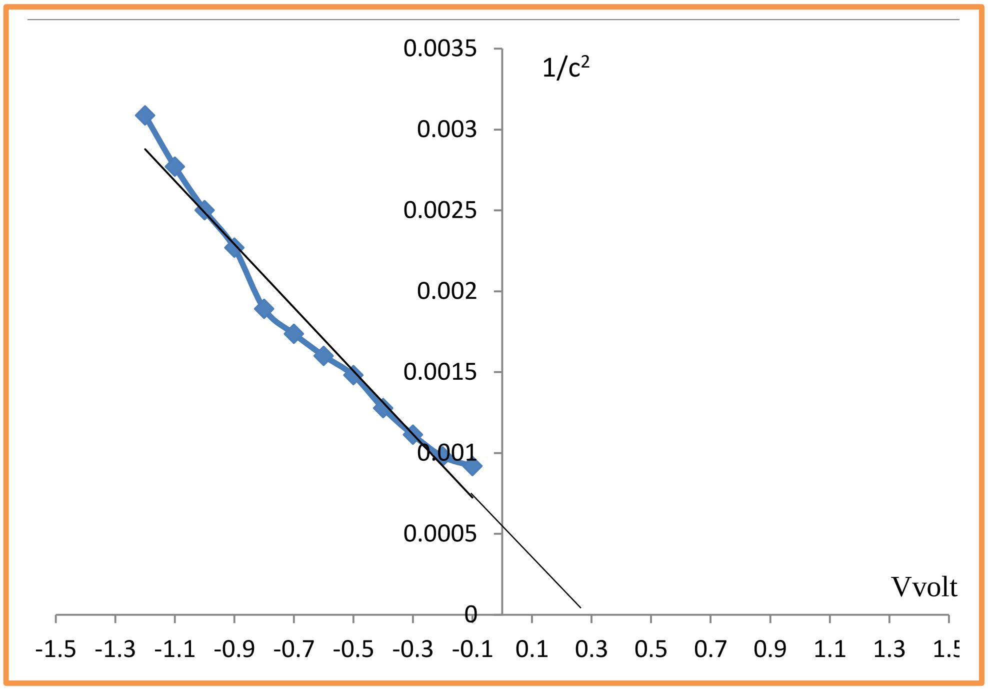

Figure(4.43): $1/c^2$ Vs Applied Voltage of CuO: 0.002 wt Cu_2O Thin Film at Annealing Temperature (200)°C for Two Hours.

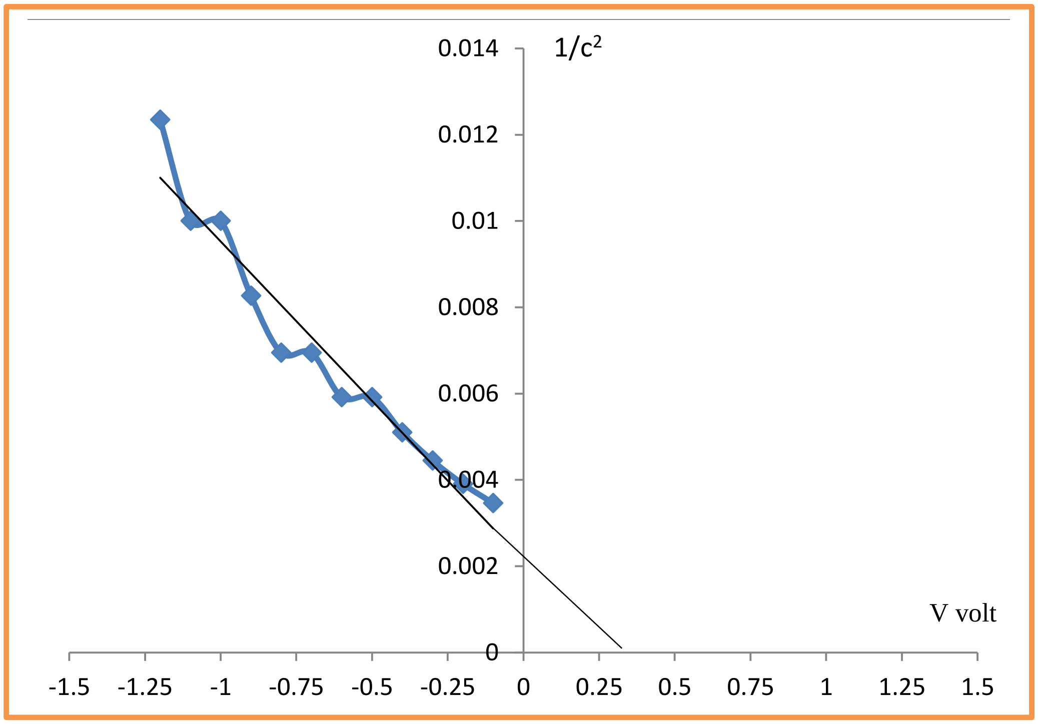

Figure(4.44): $1/c^2$ Vs Applied Voltage of of CuO: 0.004 wt% Cu_2O Thin Film at Annealing Temperature (200)°C for One Hour.

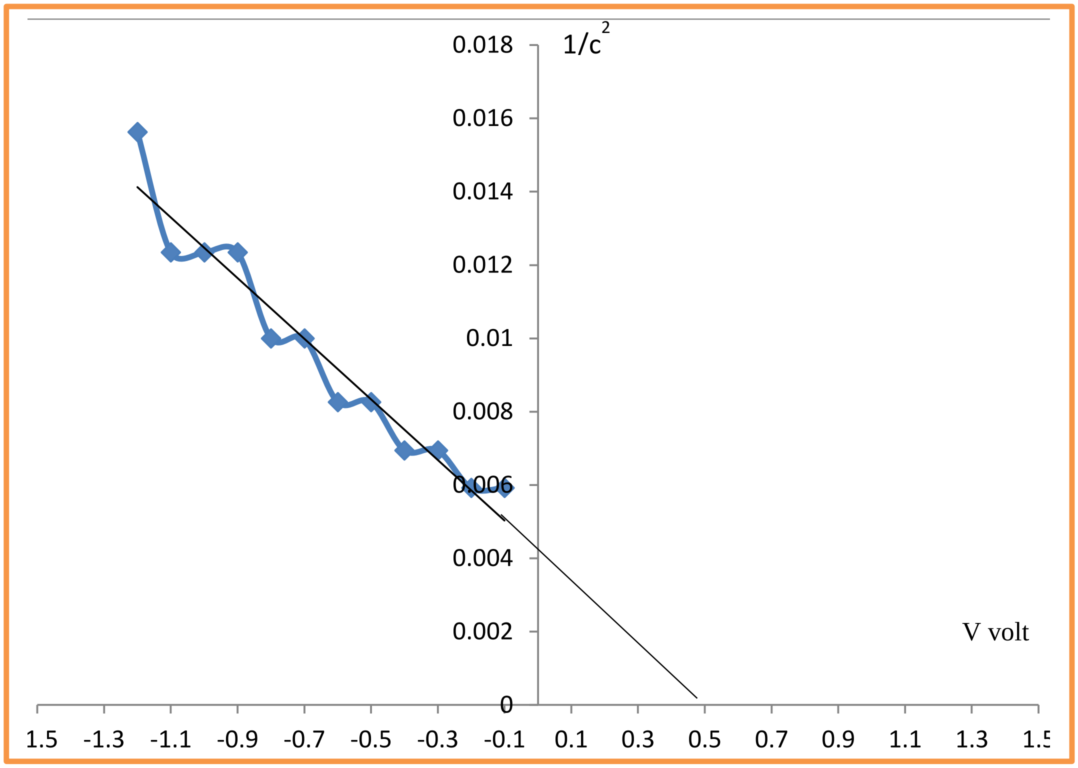

Figure(4.45): 1/c^2 Vs Applied Voltage of of CuO: 0.004Cu$_2$O Thin Film at Annealing Temperature (200)°C for Two Hours.

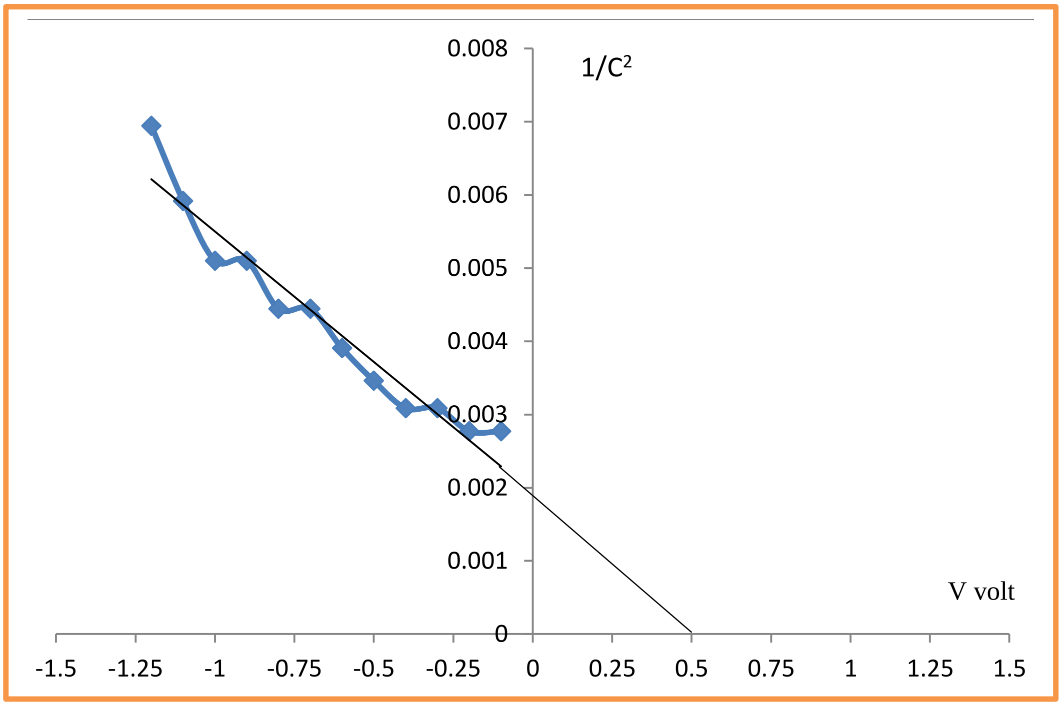

Figure(4.46): 1/c^2 Vs Applied Voltage of of CuO: 0.006wt% Cu$_2$O Thin Film at Annealing Temperature (200)°C for One Hour.

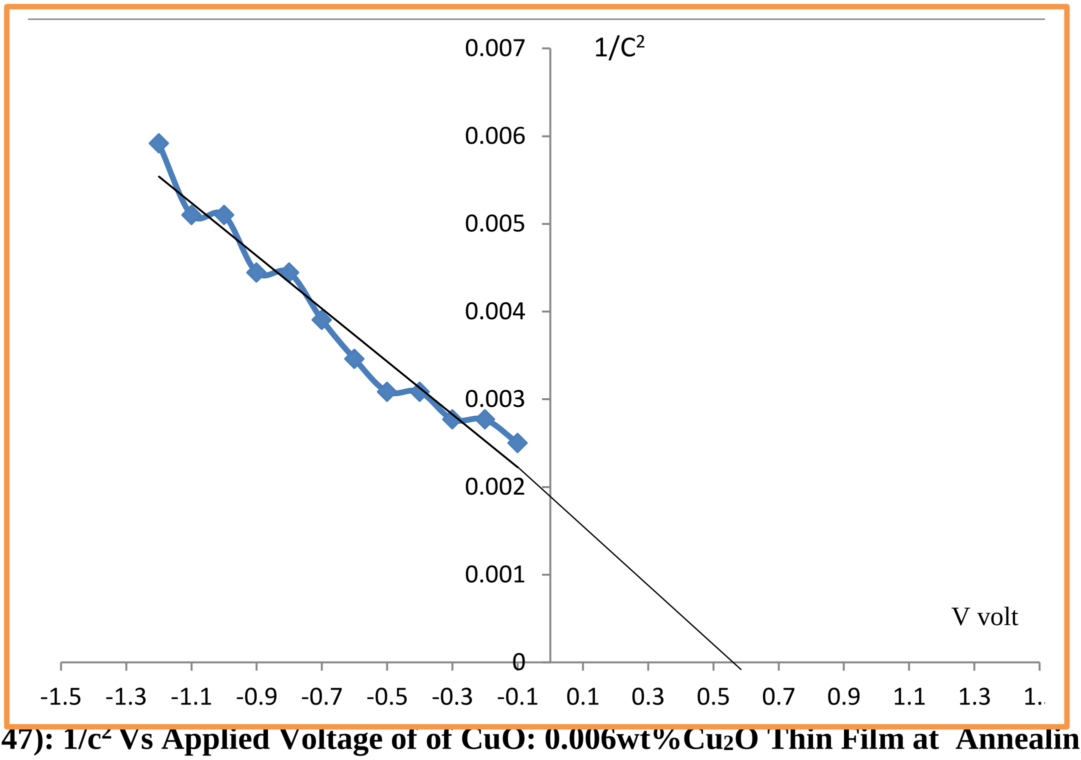

Figure(4.47): 1/c² Vs Applied Voltage of of CuO: 0.006wt%Cu_2O Thin Film at Annealing Temperature (200)°C for Two Hours.

Table (4.8): The results of capacity voltage with various weight ratios of CuO:Cu_2O at various annealing times.

Sample Name	**Built-in Potential**	**V_{oc} (mV)**	**I_{sc} (mI)**
Pure CuO at 1h.	0.19	2.20	0.0050
Pure CuO at 2h.	0.23	2.20	0.0065
CuO:0.002%Cu_2O at 1h.	0.25	2.20	0.0090
CuO:0.002%Cu_2O at 2h.	0.3	2.25	0.0110
CuO:0.004%Cu_2O at 1h.	0.35	2.20	0.0130
CuO:0.004%Cu_2O at 2h.	0.48	2.20	0.0150
CuO:0.006%Cu_2O at 1h.	0.5	2.20	0.0170
CuO:0.006%Cu_2O at 2h.	0.6	1.95	0.0180

4.4 Conclusions

1. Through the images of the atomic force microscopy (AFM), it can see that the film morphology and surface roughness were affected by Cu_2O doping. The roughness average and the root mean square (RMS) increased with the increase of Cu_2O doping.
2. The XRD analysis of the prepared $CuO:Cu_2O$ thin films indicates that the films have high-quality polycrystalline and exhibited (101) orientation, as the doping different weight ratios decreases the particle size and converts the films to amorphous. Small crystallite size, calculated from XRD, makes the surface of the films more interactions with the incident photons, leading to more efficiency in solar cells and gas sensors applications.
3. From the scanning electron microscopy (SEM), the images are shown the spherical shape of nanoparticles is observed by pure CuO and by Cu_2O doping with various weight ratios. It can notice that the particle size decrease with the increase of Cu_2O. The particle sizes that were measured from the SEM were comparable with that calculated from XRD data.
4. The transmittance of the $CuO:Cu_2O$ films decreased with increase of annealing temperatures, while the absorbance increased. The absorbance is also increased with the increase of Cu_2O doping as the transmittance decreases. Makes the films more suitable for solar cell fabrication.
5. The energy band gap (E_g) has increased with annealing temperature while it decreases with increasing Cu_2O doping.
6. The refractive index, extinction coefficient, and real and imaginary parts of dielectric constants were slightly increased with increasing annealing temperature for the prepared films. Also, they increase with the increase of Cu_2O doping.

7. Hall measurements indicated the pure and CuO:Cu_2O are n-type semiconductors with high number of carrier at different weight ratios, make the films suitable in solar cell application.
8. The high values of open circuit voltage and short circuit current give high conversion efficiency (η) that increased with the increase of Cu_2O doping.
9. The built-in potential at capacitance-voltage calculations increased with the increasing of Cu_2O doping, make the films suitable in solar cell application.
10. The high number of particles (despite the nano-thickness) on the films surface (small particle size) resulted from XRD and SEM measurements with low roughness resulting from AFM, made the good conversion efficiency compared with the thickness.

4.5 Future projects

In this context, a further investigation can be suggested as future works:

1. Using other types of deposition substrate such as quartz, silicon, or porous silicon to deposited CuO thin films.
2. Using other deposition methods (chemical or physical) with the same parameters of preparation and deposition of CuO films approved in this study.
3. Using other parameters for deposition of CuO thin films, such as changing the thickness of the layers or weight.

References

[1] D. Taesoo and U.A. Ebong,. A Review of Thin Film Solar Cell Technologies and Challenges**,** Renewable and Sustainable Energy Reviews, 70, 1286-1297, (2017).

[2] S. Iniyan and R. Goic,. A Review of Solar Photovoltaic Technologies, Renewable and Sustainable Energy Reviews 15.3, 1625-1636, (2011).

[3] R. Roesch, T. Faber, V. Hauff, E. Brown, T. M., M. Lira-Cantu and H. Hoppe,. Procedures and Practices for Evaluating Thin-Film Solar Cell Stability, Advanced Energy Materials, 5(20), 1501407, (2015).

[4] M. Hadi, S. A. AlSaati and F. Z. Razooqi,. Preparation of High Transmittance TiO_2 Thin Films by Sol-Gel Technique As Antireflection Coating, Journal of Physics: Conference Series, 1032. No. 1. IOP Publishing, (2018).

[5] W. Knoll and R. C. Advincula, (Eds.),. Functional Polymer Films, 2 Volume Set, John Wiley and Sons, (2013).

[6] M. Cernea,. Methods for Preparation of $BaTiO_3$ Thin Films, Journal of Optoelectronics and Advanced Materials 6.4 , 1349-1356, (2004).

[7] W. Grylls and R. E. Day,. V. The Action of Light on Selenium, Proceedings of the Royal Society of London 25.171-178 , 113-117, (1877).

[8] L. Panwar, R., N., F.Yettou and A.Gama,. A Comprehensive Review of Different Types of Solar Photovoltaic Cells and Their Applications, International Journal of Ambient Energy, 1-18, (2019).

[9] J. Furer,. Growth of Single-Wall Carbon Nanotubes by Chemical Vapor Deposition for Electrical Devices, Diss. University of Basel, (2006).

[10] D. Liu, W. Wu, Y. Qiu, S.Yang, S. Xiao, Q. Q. Wang and J. Wang,. Surface Functionalization of ZnO Nanotetrapods with Photoactive and Electro-Active Organic Monolayers, J. of Langmuir, 24, 5052-5059, (2008).

[11] J. Miron,. Capacitance-Voltage Profiling Techniques for Characterization of Semi-conductor Materials and Devices, ArXiv Preprint ArXiv, 3463 ,(2010).

[12] P. Maria and M. S. Chavali,. Metal Oxide Nanoparticles As Biomedical Materials, Biomimetic 5.2: 27, (2020).

[13] X. Cigang and K. L. Choy,. Chemical Vapour Deposition of Ultrafine Particles, Chemical Vapour Deposition (CVD) Advances, Technology, and Applications. CRC Press, 105-151, (2019).

[14] B. Malhotra and M. A. Ali,**.** Nanomaterials for Biosensors, Fundamentals and Applications, Nanomaterials for Biosensors,1,(2018).

[15] C. Coussens and L. Goldman, eds,. Implications of Nanotechnology for Environmental Health Research, National Academies Press, (2005).

[16] L.Kazmevski,. Polycrystalline and Amorphous Thin Films and Devices, Academic Press ,Elsevier, (2012).

[17] G. Asad, Z. T. Khodair and M. H. Saeed,. Influence of Substrate Temperature on Optical Properties of CdO Thin Films, Journal of the College of Basic Education 18.73, (2012).

[18] H. Peng, L. Jiang, J. Huang and G. Li,. Synthesis of Morphologically Controlled Tin Sulfide Nanostructures, Journal of Nanoparticle Research,9, 1163, (2007).

[19] H. Lu, C. Chu, C. Y. Lai and Y. H. Wang,. Property Variations of Direct-Current Reactive Magnetron Sputtered Copper Oxide Thin Films Deposited at Different Oxygen Partial Pressures, Thin solid films, 517(15), 4408-4412, (2009).

[20] Y. S. Lee, M. T. Winkler, S. C. Siah, R. Brandt and T. Buonassisi,. Hall Mobility of Cuprous Oxide Thin Films Deposited by Reactive Direct-Current Magnetron Sputtering, Applied Physics Letters 98.19, 192115, (2011).

[21] R. Sahay, J. Sundaramurthy, P. S. Kumar, V. Thavasi, , S. G. Mhaisalkar and S. Ramakrishna,. Synthesis and Characterization of CuO Nanofibers, and Investigation for its Suitability as Blocking Layer in ZnO NPs Based Dye Sensitized Solar Cell and as Photocatalyst in Organic Dye Degradation, Journal of Solid State Chemistry, 186, 261-267, (2012).

[22] V. V.Tyagi, N. A. Rahim, A.Jeyraj and L.Selvaraj,. Progress in Solar PV Technology: Research and Achievement, Renewable and Sustainable Energy Reviews, 20, 443-461, (2013).

[23] T. Dimopoulos, A. Peić, S. Abermann, M. Postl, E.J.W. List-Kratochvil and R. Resel,. Effect of Thermal Annealing in Vacuum on the Photovoltaic Properties of Electrodeposited Cu_2O-Absorber Solar Cell, EPJ Photovoltaics , 5, 50301, 1-6, (2014).

[24] M. Gul, Y. Kotak and T. Muneer,. Review on Recent Trend of Solar Photovoltaic Technology, Energy Exploration and Exploitation 34.4, 485-526, (2016).

[25] V. Kanna and D. Pinky,. Solar Research–A Review and Recommendations for the Most Important Supplier of Energy for The Earth with Solar Systems, International Journal of Ambient Energy 41.8, 962-968, (2018).

[26] D. Naveena, T. Logu, R. Dhanabal, K. Sethuraman and A.C. Bose,. Comparative Study of Effective Photoabsorber CuO Thin Films Prepared Via Different Precursors Using Chemical Spray Pyrolysis for Solar Cell Application, Journal of Materials Science: Materials in Electronics, 30(1), 561-572, (2019).

[27] A. N. Tuama, K. H. Abassb and M. A. Agama,. Fabrication and Characterization of Cu_2O:Ag/Si Solar Cell Via Thermal Technique, International Journal of Nanoelectronics and Materials ,13.3, (2020).

[28] S. Kawanishi, I. Suzuki, S. R.Bauers, A. Zakutayev, H. Shibata, H. Yanagi and T. Omata,. SnS Homojunction Solar Cell with n-Type Single Crystal and p-Type Thin Film, Solar RRL, *5*(4), 2000708, (2021).

[29] M. E. H. Attia, E. Elaloui, M. Abdelgaied and A. Abdullah,. Experimental Study on Improving the Yield of Hemispherical Distillers Using CuO Nanoparticles and Cooling the Glass Cover, Solar Energy Materials and Solar Cells, 235, 111482, (2022).

[30] N. Tigau, V. Ciupina, G. Prodan, G. I. Rusu, C. Gheorghies and E. Vasile,. The Influence of Heat Treatment on the Electrical Conductivity of Antimony Trioxide Thin Films, Journal of Optoelectronics and Advanced Materials, *5*(4), 907-912, (2003).

[31] M. Biver and W. Shotyk,. Stibiconite (Sb_3O_6OH), Senarmontite (Sb_2O_3) and Valentinite (Sb_2O_3): Dissolution Rates at pH 2–11 and Isoelectric Points, Geochimica et Cosmochimica Acta, 109, 268-279, (2013).

[32] S. W. Wijnhoven, W. J. Peijnenburg, C. A. Herberts, W. I. Hagens, A. G. Omen, E. H. Heugens and R. E. Geertsma,. Nano-Silver-A Review of Available Data and Knowledge Gaps in Human and Environmental Risk Assessment, Nanotoxicology, 3, 109, (2009).

[33] M. Scheringer, M. Macleod, T. Behra, L. Sigg and K. Hungerbühler,. Environmental Risks Associated with Nanoparticulate Silver Used as Biocide, Household Pers. Care Today,1, 34, (2010).

[34] B. Nowack,. Nanosilver Revisited Downstream, Science, 330, 1054, (2010).

[35] T. M. Benn and P. Westerhoff,. Nanoparticle Silver Released into Water From Commercially Available Sock Fabrics, Environmental Science and Technology, 42, 4133, (2008).

[36]L. Geranio, M. Heuberger and B. Nowack,. Behavior of Silver Nanotextiles During Washing, Environmental Science and Technology,43, 8113, (2009).

[37] E. Navarro, F. Piccapietra, B. Wagner, F. Marconi, R. Kaegi, N. Odzak and R. Behra,. Toxicity of Silver Nanoparticles to Chlamydomonas Reinhardtii, Environmental Science and Technology,42, 8959, (2008).

[38] W. Jin-Feng, C. Hong-Cun, Z. Xing-Hua, Z .De-Jun and Z. Wei-Lie,. Nonlinear Electrical Behavior of the $TiO_2.Sb_2O_3$ System, Chinese Physics Letters, 17,7, 530, (2000).

[39] N. Tigau, V. Ciupina and G. Prodan,. The Effect of Substrate Temperature on the Optical Properties of Polycrystalline Sb_2O_3 Thin Films, Journal of crystal growth, 277, 1-4, 529-535, (2005).

[40] D. M. Faulkner, Garcia-Prieto and R. J. Alcock,. The Influence of Specimen Misalignment on Wear in Conforming Pin on Disk Tests, Wear 257,1-2, 157-166, (2004).

[41] D. I. Bower,. An Introduction to Polymer Physics, Cambridge University Press, (2002).

[42] M. Rahman, A.J. Ahammad, J. H. Jin, S. J. Ahn and J. J. Lee,. A Comprehensive Review of Glucose Biosensors Based on Nanostructured Metal-Oxides, Sensors, 10, 4855, (2010).

[43] B. E. Warren,. X-Ray Diffraction. Courier Corporation, (1990).

[44] Z. H. Ibupoto, S. M. U. Ali, K. Khun, C. O. Chey, O. Nur and M. Willander,. ZnO Nanorods Based Enzymatic Biosensor for Selective Determination of Penicillin, Biosensors,1, 153, (2011).

[45] J. Solgom,. Fundamentals of the Physics of Solids: Structure and Dynamics, Springer Berlin Heidelberg, New York, (2007).

[46] L. Gumus, O. M. Ozkendir, H. Kavak and L. Ufuktepe,. Structural and Optical Properties of Zinc Oxide Thin Films Prepared by Spray Pyrolysis Method, J. Optoelectronics and advanced materials, 8, 299-303, (2006).

[47] D. M. Mattox and V. H. Mattox,. Foundations of Vacuum Coating Technology, William Andrew publishing/Noyes, (2003).

[48] R. Parsons, J. L. Vossen and W. Kern,. Thin Film Processes II, Boston academic press, (1991).

[49] S. M. Sze,. Semiconductor Devices: Physics and Technology, John Wiley and Sons,(2008).

[50] M. Azad and A. Abdullah,. Scanning Electron Microscopy (SEM): A Review, Proceedings of the 2018 International Conference on Hydraulics and Pneumatics—HERVEX, Băile Govora, Romania, (2018).

[51] R. Wiesendanger,. Scanning Probe Microscopy and Spectroscopy, Cambridge University Press, (1994).

[52] E. Meyer,. Aomic Force Microscopy, Progress in Surface Sci,41, 3-49, (1992).

[53] F. J. Giessibl,. Advances in Atomic Force Microscopy, Reviews of Modern Physics, 75, 3, 949, (2003).

[54] L. R. Johnson,. Characterization of Piezoelectric ZnO Thin Films and the Fabrication of Piezoelectric Micro-Cantilevers, Iowa State University,(2005).

[55] B. A. Hasan and I. H. Shallal,. Structural and Optical Properties of SnS Thin Films, Journal of nanotechnology and advanced materials, 2, 43, (2014).

[56] G. T. Chen, S. H. Su, C. C. Hou and M. Yokoyama,. Effects of Thermal Annealing on Performance of Organic Light-Emitting Diodes**,** Journal of The Electrochemical Society, 154, 5, 159-162, (2007).

[57] S. M. Ho,. Atomic Force Microscopy Studies on the Surface Morphologies of Chemical Bath Deposited Cus Thin Films**,** INTI International University, Putra Nilai, 71800, Negeri Sembilan, MALAYSIA. 32, 3, 1515-1519, (2016).

[58] M. Dehimi, T. Touam, A. Chelouche, F. Boudjouan, D. Djouadi, J. Solard and A. Doghmane,. Effects of Low Ag Doping on Physical and Optical Waveguide Properties of Highly Oriented Sol-Gel ZnO Thin Films, Adv.Condensed Matter Phys. 2015, 10, (2015).

[59] A. Tanusevskia and D. Poelmanb,. Optical and Photoconductive Properties of SnS Thin Films Prepared by Electron Beam Evaporation, Solar Energy Materials and Solar Cells, 80, 297, (2003).

[60] J. Jeong, S. P. Choi, K. J. Hong, J. S. Park and H. J. Song,. Structural and Optical Properties of SnO_2 Thin Films Deposited by Using CVD Techniques, Journal of the Korean Physical Society, 48,5, 960-963, (2006).

[61] D. Oman, K. Dugan, G. Killian, V. Ceekala, C. Ferekides and D. Morel,. CdTe Contacts for CdTe/CdS Solar Cells, Effect of Cu Thickness, Surface Preparation and Recontacting on Device Performance and Stability, Solar energy materials and solar cells, (1999).

[62] B. G. Yacobi,. Semiconductor Materials, Kluwer Academic Publishers ,New York, (2004).

[63] F. Bassani and G. P. Parravicini,. Electronic States and Optical Transitions in Solids, Pergamon Press, NY (1975).

[64] K. L. Chopra, I. Kaur,. Thin Film Device Applications, Plenum Press, New York, (1983).

[65] M. A. Omer,. Elementary Soild State Physics, Addiso-Wesly publishing, (1975).

[66] I. A. Z. Taha,. Preparation and Characterization of Delafossite $CuFeO_2$ TCO Thin Films by Using SPD Technique, M. Sc. thesis , Physics Science, University of Kufa , (2014).

[67] O. Stenzel,. The Physics of Thin Film Optical Spectra, Springer- Verlag Berlin Heidelberg , Germany, (2005).

[68] Y. Sirotin, Y. M. Shaskolskaya,. Fundamentals of Crystal Physics, Mir Publishers, Moscow, (1982).

[69] J. Tauc,. Amorphous and Liquid Semiconductors, Plenum press, London, N.Y, (1974).

[70] C. Kittle,. Introduction to Solid State Physics, John Wiley and Sons Inc, 8th edition, (2005).

[71] R. S. Popovic,. Hall Effect Devices, Institute of Physics Publishing, Bristol and Philadelphia, (2004).

[72] D .A. Neamen,. Semiconductor Physics and Devices Basic Principles, McGraw-Hill Companies, Inc.,New York, (2003).

[73] B. R. Nag,. Electron Transport in Compound Semiconductors, Spring-Verlag Berlin Heiderg New York, (1980).

[74] V. b. Georgieva, A. Tanusevski, and M. Georgieva,. Low Cost Solar Cells Based on Cuprous Oxide, Intech Open,(2011).

[75] V. Viswanathan,. Study of Cu Free Back Contacts to Thin Film CdTe Solar Cell, Ph.D. thesis, University of South Florida, (1985).

[76] N. Amin and T. Isaka,. Effect of Substrate Temperatures on CdSe:Sn Thin Films, Journal Application Physics, 38, 1698, (2000).

[77] D. M. Chapin, C. S. Fuller and G. L. Pearson,. Study of Depletion Region Collection in Solar Cells , 25, 676, (1974).

[78] J. Lindmayer,. Theoretical and Practical Fill Factors in Solar Cells, COMSAT Technical. Rev 2 , 105(1972).

[79] N. H. Kim, J. S. Park and W. S. Lee,. Effective Ag Doping by He-Ne Laser Exposure to Improve the Electrical and the Optical Properties of CdTe Thin Films for Heterostructured Thin Film Solar Cells, Journal of the Korean Physical Society 59.3, 2286-2290,(2011).

[80] R. H. Bube,. Photovoltaic Materials Imperial College Press, (1998).

[81] JCPDS,. Joint Committee for Powder Diffraction Standards, Power Diffraction File for Inorganic Materials, 79-2205,(1979).

[82] T. A. Lastovina, A. P. Budnyk, G. A. Khaishbashev, E. A. Kudryavtsev and A. V. Soldatov,. Copper-Based Nanoparticles Prepared From Copper (II) Acetate Bipyridine Complex, Journal of the Serbian Chemical Society.; 81(7), 751-762,(2016).

[83] K. Abdali, F. Lamis, A. Abdmuslem, O. Abdulazeez and A. Abdulazeez,. Enhancing Some Physical Properties of Cosmetic Face Powders, (2009).

[84] R. Vinodkumar, I. Navas, S. R. Chalana, K. G. Gop-Chandran, V. Ganesan, R. Philip, S. K. Sudheer and V. P. Mahadevan Pillai,. Highly Conductive and Transparent Laser Ablated Nanostructured Al:ZnO Thin Films, Appl. Surface Sci., 257, 3, 708- 716, (2010).

[85] C. A. Tseng, J. C. Lin, Y. F. Chang,. Microstructure and Characterization of Al-doped ZnO Films Prepared by RF Power Sputtering on Al and ZnO Targets, Appl. Surface Sci., 258, 16, 5996-6002, (2012).

[86] H. Y. Cheng, Y. C. Chen, C. L. Li, P. J. Li, M. P. Houng and C. F. Yang,. Developments of the Physical and Electrical Properties of NiCr and NiCrSi Single-Layer and Bi-Layer Nano-Scale Thin-Film Resistors, Nanomaterials 6.3 , 39, (2016).

[87] E. M. Mkawi, K. Ibrahim, M. K. M. Ali, M. A. Farrukh, A. S. Mohamed,. Influence of Triangle Wave Pulse on the properties of Cu_2ZnSnS_4 Thin Films Prepared by Single Step Electrode Position, Solar Energy Materials and Solar Cells130,91–98 (2014).

[88] G. A. Kumar, M.V. Ramana and K. N. Reddy., Structural and Optical Properties of ZnO Thin Films Grown on Various Substrates by RF Magnetron Sputtering, International Conference on Materials Science and Technology, 73, (2015).

[89] S. I. Salih,. Effect of Sb_2O3 and/or CdO Nanoparticle Substitution on the Properties of High-TC Superconducting Bi1. 6-x SbxPb0. $4Sr_2Ca_2$-$yCdyCu_3OZ$ Material, Iraqi Journal of Physics 16.36 , 73-84, (2018).

[90] A. R. D. A. Rajapaksha, C. A. N. Fernando, R. G. Balakrishna, V. Kumar and P. See,. An Insight in Photocurrent Generation Mechanism on Cu_2O Quantum Dot Sensitized Cu/p-CuI Photo-Electrochemical Cell and Efficient H_2 Generation at Cu/p-CuI/Cu_2O Electrolyte Interface. Materials Science and Engineering*:* B, 270, 115205, (2021).

[91] A. A. Hssi, L. Atourki, K. Abouabassi, A. Elfanaoui, K. Bouabid, A. Ihlal and MC.Ouafi,. Growth and Characterization of Cu_2O for Solar Cells Applications. In AIP Conference Proceedings (Vol.2056, No.1, p.020006). AIP Publishing LLC. (2018).

[92] P. Domens, M. Cadene,. Phys . Stat . Sol (a),59 , 20 , (1982).

[93] B. E. Warren,. X-ray Diffraction, Courier Corporation , (1990).

[94] I. S. Yahia, Y. S. Rammah and K. F. Khaled,. Fabrication of An Electrochemical Cell Based on Rhodamine B Dye for Low Power Applications, Journal of Materials and Environmental Science, 4, 3, 442-447, (2013).

[95] V. R. M. Reddy, S. Gedi, C. Park, R. W. Miles and R. Reddy,. Development of Sulphurized SnS Thin Film Solar Cells, Current applied physics,15, 588 (2015).

[96] B. A. Abdullah,. Optical Properties of Rhodamine B Dye Mixed with Polyvinyl-Pyrrolidone (PVP) as a Matrix, Journal of Kufa – Physics,9, 2, (2017).

[97] N. Tigau, V. Ciupina and G. Prodan,. Structural, Optical and Electrical Properties of Sb_2O_3 Thin Films with Different Thickness, Phys. Stat. S o1. (b) 54 ,701, (2006).

[98] A. O.Mousa and H. Hasan,. Investigation of Structure and Optical Properties of Barium Oxide (BaO) Thin Films Deposited by (CSP), relation 21: 5,(2016).

[99] M. Habibi, N. Talebian and J. Choi,. The Effect of Annealing on Photocatalytic Properties of Nanostructured Titanium Dioxide Thin Films , Dyes and Pigments, 73,103-110, (2007).

[100] M. Hassan, A. Haseeb, R. Saidur and H. Masjuki,. Effects of Annealing Treatment on Optical Properties of Anatase TiO^2 Thin Films , World Academy of Science, Engineering and Technology,40, 221-225, (2008).

[101] H. Karaagac and Peksu,. A Third Generation Solar Cell Based on Wet Chemically Etched Si Nanowires and Sol-Gel Derived Cu_2ZnSnS_4 Thin Films, Journal of Alloys and Compounds 774 , 1117-1122, (2019).

[102] A. H. Abed,. Study the Effect of Thickness on Optical Properties of Sb_2O_3 Thin Films, Al-Mustansiriyah Journal of Science, 22,1,129-138, (2011).

[103] S. Karvinen,. The Effect of Trace Element Doping of TiO_2 on the Crystal Growth and on the Anatase to Rutile Phase Transformation of TiO_2 , Solid State Sci.,5, 811-819, (2003).

[104] A. A. Alnajjar,. ZnO:Al Grown by Sputtering from Two Different Target Sources. A Comparison Study, Advances in condensed matter phys. Article, (2012).

[105] K. Hosein, E. K. Reza, J. S. Farid and Y. Ramin,. Effect of Al Doping on the Structural and Optical Properties of Electrodeposited SnS Thin Films, 213, 1302, (2016).

[106] P. Lu, H. Jia and S. Cheng,. Optical and Electrical Properties of SnS:Ag Films as Solar Cell Absorbers. Advanced materials research,11, 60-61, (2009).

[107]S. Habashyani, A. Özmen, S. Aydogan,. An Examination of Correlation Between Characteristic and Device Performance of ZnO Films as a Function of La Content, Vacuum 157 , 497-507, (2018).

[108] A. Tombak, M. Benhaliliba, Y. S. Ocak, T. Kiliçoglu,. The Novel Transparent Sputtered P-Type CuO Thin Films and Ag/p-CuO/n-Si Schottky Diode Applications, Results Phys 5 , 314-321, (2015).

[109] A. B. Uluşan, A. Tataroğlu, Y. Azizian-Kalandaragh,. On the Conduction Mechanisms of Schottky Barrier Diodes (SBDs) Using Current–Voltage–Temperature (I–V–T) Characteristics, J. Mater. Sci. Mater. Electron. (2018).

[110] K. Lab and N. Nianxin,. Preparation and Characterization of Cu_2ZnSnS_4 Thin Films and Solar Cells Fabricated from Quaternary Cu-Zn-Sn-S Target ,Journal of Photo energy, Vol 2013,Article ID929454,P.9,(2013).

[111] Z. Wang, J. Tao, W. Xiao,. Zhimin Ma Influence of Deposition Potential on Cu_2ZnSnS_4 Thin Film Solar Cells Co Electrodeposited on Fluorine Doped Tin Oxide Substrates, Journal 701 , 465-473,(2017).

[112] V. Georgieva, A. Tanusevski,. Low Cost Solar Cells Based on Cuprous Oxide , Solar Cells-Thin-Film Technologies , 55-56, (2011).